

## ABSTRACT

Title of Document:                   EXPERIMENTAL AND NUMERICAL  
                                                  STUDIES OF DRILL-STRING DYNAMICS

Chien-Min Liao, Ph.D., 2011

Directed By:                         Professor Balakumar Balachandran  
                                                  Department of Mechanical Engineering

A drill string is the transmission component of rotary drill-rig system used for mining petroleum and natural gas resources. The drill-string system is essentially a long slender structure whose length can be in kilometers. Additionally, the drill-string is subject to discontinuous forces from interactions with the wellbore, which can cause erratic torsion oscillations and stick-slip motions. Here, a unique scaled experimental apparatus has been constructed to understand the dynamics of one section of the drill-string subjected to stick-slip interactions with an outer shell. In both the experimental and modeling efforts, the drill-string system is studied as a slender rod with large discs on either end, with the bottom disc being enclosed within a shell, which is representative of a borehole. The experimental setup allows for studies of stick-slip interactions between a drill-string like system and an outer shell, unlike the prior studies. A series of careful experiments are conducted with special attention to parameters such as the drive speed, the mass imbalance, and the nature of contact between the bottom disc and the outer shell. The experimental results indicate that the rotor motions can be divided into different phases, with each phase being characterized by its own unique features that include bumping, sticking, slipping, and rolling characteristics. In order to gain insights into the drill-string

dynamics, reduced-order models have been developed inclusive of a novel drill-string wellbore force-interaction model that can account for stick-slip behavior. Both the experimental observations and model predictions are found to be in agreement, in terms of the system dynamics. Furthermore, parametric studies have been conducted and the findings are presented in the form of experimental and numerical simulation results, and the qualitative changes observed in the dynamics are discussed. These findings suggest that the drill-string curvature and contact friction plays an important role in determining the presence of erratic motions. This dissertation effort provides clues to how the drive speed can be used as a control parameter to move the system out of regions of undesired dynamics and how the drill-string motions can be influenced to keep them close to the borehole center.

EXPERIMENTAL AND NUMERICAL STUDIES OF  
DRILL-STRING DYNAMICS

By

Chien-Min Liao

Dissertation submitted to the Faculty of the Graduate School of the  
University of Maryland, College Park, in partial fulfillment  
of the requirements for the degree of  
Doctor of Philosophy  
2011

Advisory Committee:

Professor Balakumar Balachandran, Advisor and Chair

Professor Mansour Karkoub, Texas A&M, Qatar

Professor Amr Baz

Professor Abhijit Dasgupta

Assistant Professor Miao Yu

Professor Inderjit Chopra, Dean's Representative

© Copyright by  
Chien-Min Liao  
2011

## ACKNOWLEDGEMENTS

I would like to thank the people who helped me on this research and dissertation during my time as a researcher at the University of Maryland. Most importantly, I appreciate the great support received from my advisor Professor Balachandran. He offered tremendous support, and I am thankful to him for his guidance and the efforts he put forth while directing my research. All of his efforts have been like a lighthouse in the dark that has guided my success. I would also like to show my kind appreciation to my family members; their support and encouragement gave me motivation and energy throughout my research. Additionally, interactions and discussions with the members of my research group and dissertation committee members, Professor Baz, Professor Chopra, Professor Dasgupta, Professor Karkoub and Professor Yu, were also beneficial and greatly appreciated. I would also like to thank Dr. Karki of the Petroleum Institute at Abu Dhabi, UAE for helpful information and Mr. Nicholas Vlajic for helping me with the experiments. Last but not the least, the support received from the Energy and Education Research Collaboration between the Petroleum Institute and University of Maryland, over the last five years is gratefully acknowledged.

## TABLE OF CONTENTS

<b>LIST OF FIGURES</b> .....	<b>V</b>
<b>LIST OF TABLES</b> .....	<b>X</b>
<b>1. Introduction and Background</b> .....	<b>1</b>
1.1. Drill-String Vibration Studies .....	<b>6</b>
1.2. Stick-Slip Behavior .....	<b>10</b>
1.3. Nonlinear Oscillations and Interactions .....	<b>11</b>
1.4. Objectives and Scope of Work .....	<b>12</b>
1.5. Organization of Dissertation .....	<b>13</b>
<b>2. Experimental Studies</b> .....	<b>15</b>
2.1. Design and Arrangement .....	<b>16</b>
2.2. Experimental Data Collection and Results .....	<b>21</b>
2.2.1. Results at first glance .....	<b>21</b>
2.2.2. Image processing .....	<b>23</b>
2.3. Rotor Response Observations .....	<b>24</b>
2.3.1. Rotor motions at different rotation speeds .....	<b>24</b>
2.3.2. Rotor response about center and forward whirling phase .....	<b>28</b>
2.3.3. Rotor response in bumping and backward whirling phases .....	<b>31</b>
2.3.4. Characteristics of rotor dynamics .....	<b>36</b>
<b>3. Modeling, Simulations, and Comparisons</b> .....	<b>40</b>
3.1. Reduced-Order Models .....	<b>41</b>
3.1.1. Model parameters .....	<b>41</b>
3.1.2. Four degree-of-freedom model .....	<b>43</b>
3.1.3. Different presentation for four degree-of-freedom model .....	<b>53</b>
3.1.4. Five degree-of-freedom model .....	<b>55</b>
3.2. Analytical Investigations .....	<b>61</b>
3.2.1. Equilibrium solutions .....	<b>61</b>
3.2.2. System performance around equilibrium .....	<b>63</b>
3.3. Numerical Investigations .....	<b>67</b>
3.3.1. Numerical results for system with four degree-of-freedom .....	<b>68</b>
3.3.2. Numerical results for system with five degree-of-freedom .....	<b>71</b>

3.3.3. Discussion .....	74
3.4. Comparisons of Model Predictions with Experimental Results .....	75
3.4.1. Qualitative comparisons .....	75
3.4.2. Comparisons with results from literature .....	77
<b>4. Parametric Studies .....</b>	<b>84</b>
4.1. Experimental Parametric Studies .....	85
4.1.1. Qualitative changes .....	85
4.1.2. Effect of mass imbalance .....	90
4.1.3. Influence of friction .....	93
4.2. Numerical Parametric Studies .....	96
4.2.1. Model description .....	96
4.2.2. Influence of initial position and driving speed .....	98
4.2.3. Results .....	99
<b>5. Summary and Recommendations for Future Work .....</b>	<b>106</b>
5.1. Summary .....	106
5.2. Future Work .....	108
5.2.1. Distributed-parameter models with experiments .....	108
5.2.2. Five degree-of-freedom model with experiments .....	109
5.2.3. Nonlinear phenomena .....	109
5.2.4. Control schemes .....	109
<b>Appendix A .....</b>	<b>110</b>
<b>Appendix B .....</b>	<b>121</b>
<b>Appendix C .....</b>	<b>128</b>
<b>Bibliography.....</b>	<b>134</b>

## LIST OF FIGURES

1.1	Schematic of a rotary drill rig .....	3
1.2	Drill-string failure types .....	5
2.1	Schematic of drill string experimental setup .....	19
2.2	Experimental setup: (a) side view and (b) top view .....	19
2.3	Components of experimental setup: (a) overall setting, (b) system components, (c) camera, (d) DC motor, (e) encoder, and (f) test bed (unbalanced mass, bottom disc and outer shell) .....	20
2.4	Rotor in bumping motion .....	22
2.5	Rotor in rolling motion .....	22
2.6	Representative images from drill-string experiments .....	23
2.7	Motor driving voltage to rotation speed relationship .....	25
2.8	Rotor trajectories for different rotation speeds with rubber-aluminum contact: (a) 37.5 rpm (revolutions per minute), (b) 55.4 rpm, (c) 73.8 rpm, (d) 81.6 rpm, (e) 92.5 rpm, and (f) 148.2 rpm. ....	27
2.9	Rotor response for rotating speed of 37.5 rpm with aluminum-aluminum contact: (a) rotor trajectory, (b) radial displacement history, (c) time histories of normal and tangential speeds, and (d) normal and tangential displacement histories (top) and corresponding frequency spectra (bottom) .....	29
2.10	Rotor response for rotating speed of 83.1 rpm with aluminum-aluminum contact: (a) rotor trajectory, (b) radial displacement history, (c) time histories of normal and tangential speeds, (d) normal and tangential displacement histories (top) and corresponding frequency spectra (bottom) .....	30
2.11	Rotor response for rotating speed of 55.6 rpm with rubber-rubber contact-I: (a) rotor trajectory, (b) radial displacement history, (c) time histories of normal and tangential speeds, and (d) normal and tangential displacement histories (top) and corresponding frequency spectra (bottom) .....	32
2.12	Rotor response for rotating speed of 55.6 rpm with rubber-rubber contact-II: (a) rotor trajectory, (b) radial displacement history, (c) time histories of normal and tangential speeds, and (d) normal and tangential displacement histories (top) and corresponding frequency spectra (bottom) .....	33
2.13	Rotor response for rotating speed of 55.6 rpm with rubber-rubber contact-III: (a) rotor trajectory, (b) radial displacement history, (c) time histories of normal and tangential speeds, and (d) normal and tangential displacement histories (top) and corresponding frequency spectra (bottom) .....	35

2.14	Rotor response for rotating speed of 55.6 rpm with rubber-rubber contact-Complete: (a) rotor trajectory, (b) radial displacement history, (c) time histories of normal and tangential speeds, (d) normal and tangential displacement histories (top) and corresponding frequency spectra (bottom) (e) time histories of normal and tangential speeds, and (f) frequency spectra of normal and tangential displacement responses on log scale . . . . .	<b>38</b>
3.1 (a)	Illustration of two section model . . . . .	<b>45</b>
3.1 (b)	Drill string modeled as a system with two sections . . . . .	<b>45</b>
3.2 (a)	Illustration for unbalanced mass in rotor (Section II) . . . . .	<b>46</b>
3.2 (b)	Schematic of model with four degrees of freedom . . . . .	<b>46</b>
3.3	Illustrations of two contact scenarios between drill string and outer shell . . . .	<b>52</b>
3.4 (a)	Illustration for unbalanced mass in model with five degrees of freedom . . . .	<b>59</b>
3.4 (b)	Schematic of model with five degrees of freedom . . . . .	<b>59</b>
3.5	Phase portrait projections for motions around equilibrium point of four degree-of-freedom model: (a) lateral direction: initial position close to the origin, (b) lateral direction: initial position close to the outer shell (boundary), (c) lateral direction: initial position on the boundary, (d) tangential direction: initial position close to the origin, (e) tangential direction: initial position close to the boundary, and (f) tangential direction: initial position on the boundary . . . . .	<b>65</b>
3.6	Phase portrait projections for motions around equilibrium point of five degree-of-freedom model: (a) lateral direction: initial position close to the origin, (b) tangential direction: initial position close to the origin, (c) lateral direction: initial position close to the outer shell (boundary), and (d) tangential direction: initial position close to the boundary . . . . .	<b>66</b>
3.7	Four degree-of-freedom system responses for $\mu=0.9$ : (a) radial displacement of rotor versus radial speed, (b) rotation angle of stator versus rate of change of rotation angle, (c) bending angle of rotor versus rate of change of bending angle, (d) rotation angle of rotor versus rate of change of rotation angle (e) trajectory of the center of rotor in horizontal plane, in polar coordinates ( $\rho$ , $\theta$ ) . . . . .	<b>69</b>
3.8	Four degree-of-freedom system responses for $\mu=0.1$ : (a) radial displacement of rotor versus radial speed, (b) rotation angle of stator versus rate of change of rotation angle, (c) bending angle of rotor versus rate of change of bending angle, (d) rotation angle of rotor versus rate of change of rotation angle, and (e) trajectory of the center of rotor in horizontal plane, in polar coordinates	

	( $\rho, \theta$ ) .....	<b>70</b>
3.9	Five degree-of-freedom system responses for $\mu=0.9$ : (a) radial displacement of rotor versus radial speed, (b) rotation angle of stator versus rate of change of rotation angle, (c) bending angle of rotor versus rate of change of bending angle, and (d) rotation angle of rotor versus rate of change of rotation angle, (e) tilt angle of the rotor versus rate of change of tilt angle, and (f) trajectory of the center of rotor in horizontal plane, in polar coordinates ( $\rho, \theta$ ) .....	<b>71</b>
3.10	Five degree-of-freedom system responses for $\mu=0.1$ : (a) radial displacement of rotor versus radial speed, (b) rotation angle of stator versus rate of change of rotation angle, (c) bending angle of rotor versus rate of change of bending angle, and (d) rotation angle of rotor versus rate of change of rotation angle, (e) tilt angle of the rotor versus rate of change of tilt angle, and (f) trajectory of the center of rotor in horizontal plane, in polar coordinates ( $\rho, \theta$ ) .....	<b>72</b>
3.11	Numerical simulation of rotor motions corresponding to experiments: showing segments of rolling contact in (b) and bouncing contact in (c) .....	<b>76</b>
3.12	Comparison of simulation results of rotor trajectories in plane with polar coordinates ( $\rho, \theta$ ); trajectory of the center of rotor: (a) initial position close to the outer shell, friction coefficient $\mu =0.1$ ; (b) initial position close to the outer shell, friction coefficient $\mu =0.3$ ; and (c) initial position close to the outer shell, friction coefficient $\mu =0.9$ . The results obtained by using the modified four degree-of-freedom system are shown on the left column, and those obtained by using the model of Melakhessou <i>et al.</i> (2003) are shown on the right .....	<b>79</b>
3.13	Phase portraits and time histories: (a) and (d) results for friction coefficient $\mu =0.1$ , (b) and (e): results for friction coefficient $\mu =0.3$ , and (c) and (f) results for friction coefficient $\mu =0.9$ . The dashed vertical line in the phase plots corresponds to the outer shell .....	<b>81</b>
3.14	Time history of tangential motion component: (a) complete record and (b) a portion showing slipping and sticking .....	<b>82</b>
4.1	Rotor response with 61.7 grams unbalanced mass and aluminum-aluminum contact: (a) diagram of qualitative changes, (b) 28.3 rpm, (c) 74 rpm, (d) 92.5 rpm, and (e) 130 rpm .....	<b>87</b>
4.2	Rotor response by 61.7 grams unbalanced mass and aluminum - aluminum contact: (a) extreme values of radial displacement and (b) response characteristics diagram .....	<b>89</b>
4.3	Characteristic diagram of rotor response with rubber-aluminum contact: (a)	

	unbalanced mass of 28 grams and (b) unbalanced mass of 61.7 grams . . . . .	<b>92</b>
4.4	Characteristic diagram of rotor response for 28 grams unbalanced mass: (a) aluminum-aluminum contact and (b) rubber-rubber contact . . . . .	<b>95</b>
4.5	Rotor trajectory variation with respect to drive speed: (a) initial position midway between radial center and outer shell edge, and drive speed of 50 rpm; (b) initial position midway between radial center and outer shell edge, and drive speed of 200 rpm; (c) initial position close to outer shell and drive speed of 50 rpm; and (d) initial position close to outer shell with drive speed of 200 rpm . . . . .	<b>99</b>
4.6	Characteristic diagram for lateral displacement response; the circles have been included to relate to the discussion made in the text: (a) $m_b = 0.01\text{kg}$ and $\mu = 0.1$ , (b) $m_b = 0.01\text{kg}$ and $\mu = 0.3$ , and (c) $m_b = 0.01\text{kg}$ and $\mu = 0.7$ . . . . .	<b>101</b>
4.7	Characteristic diagram for lateral displacement response: (a) $m_b = 0.03\text{kg}$ and $\mu = 0.1$ , (b) $m_b = 0.03\text{kg}$ and $\mu = 0.3$ , and (c) $m_b = 0.03\text{kg}$ and $\mu = 0.7$ . . . . .	<b>103</b>
4.8	Characteristic diagram for lateral displacement response: (a) $m_b = 0.08\text{kg}$ and $\mu = 0.1$ , (b) $m_b = 0.08\text{kg}$ and $\mu = 0.3$ , and (c) $m_b = 0.08\text{kg}$ and $\mu = 0.7$ . . . . .	<b>104</b>
A.1	Experimental arrangement to study bending-torsion vibrations (on the left) with details at the bottom (on the right) . . . . .	<b>110</b>
A.2	Driving and transmission parts of the experiment . . . . .	<b>112</b>
A.3	Experimental setup on the left and main frame model on the right . . . . .	<b>113</b>
A.4	Middle shelf held by linear bearings (to allow free sliding along the vertical direction) . . . . .	<b>113</b>
A.5	Drive motor: motor mounted on top where the drive shift is inserted through the hole made on the top panel . . . . .	<b>114</b>
A.6	Metal shaft with a disc on top to be bolted onto the upper disc. A metal string (drill string) is to be screwed onto the metal shaft . . . . .	<b>114</b>
A.7	Encoder to be placed at the lower end of the metal string. The metal string is to be screwed onto the lower disc . . . . .	<b>114</b>
A.8	Rotor with brake disc. The metal string coming out of the lower disc is to be connected to a universal joint which in turn is screwed onto the brake disc . .	<b>115</b>
A.9	Cylindrical housing that encloses the lower disc and the brake disc. The encoder (white) is to be attached to the housing by using a joint . . . . .	<b>115</b>
A.10	Floating (middle) panel that supports the housing. Two laser triangulation sensors are to be placed on this panel. The panel is attached to the frame through linear bearings . . . . .	<b>116</b>
A.11	Middle and lower panels. The housing rests on the middle panel. Four	

springs and one actuator are attached to both the middle and lower panels.

The actuator is to be bolted whereas the springs are to be attached by using a

	horseshoe clamp .....	<b>116</b>
A.12	DC motor scale diagram (Ref. Anaheim Automation) .....	<b>117</b>
A.13	Brake disc (Ref. Encoder Product Inc.) .....	<b>117</b>
A.14	Absolute encoder: model 960 (Ref. Encoder Product Inc.) .....	<b>117</b>
A.15	Electro-magnetic actuator (Ref. ETREMA Inc.) .....	<b>117</b>
A.16	Laser displacement sensor (Ref. Acuity Laser Measurement) .....	<b>118</b>
A.17	Optical Sensor (Ref. Philtec Inc.) .....	<b>118</b>
A.18	Side view of arrangement .....	<b>119</b>
A.19	An isometric view of arrangement .....	<b>119</b>
A.20	Driving motor with circuit .....	<b>119</b>
A.21	Housing and bottom disc .....	<b>119</b>
A.22	Top disc with encoder .....	<b>120</b>
A.23	Wheels under the housing .....	<b>120</b>
A.24	Encoder supporting frame .....	<b>120</b>
A.25	Bottom disc with housing .....	<b>120</b>

## **LIST OF TABLES**

3.1	Symbols used for different quantities and their description .....	<b>42</b>
3.2	System parameter values used in earlier studies (Melakhessou <i>et al.</i> , 2003) ..	<b>64</b>
3.3	System parameter values used to generate numerical results for comparison with experimental results .....	<b>77</b>
A.1	Experimental components in design phase .....	<b>111</b>

# Chapter 1

## Introduction and Background

In recent years, there has been an increasing demand for petroleum across the globe. In the United States of America alone, motor gasoline consumption has reached over 378 million gallons per day<sup>1</sup>. With the ever surging demand and limited reserves, it is important that appropriate techniques be developed to improve the efficiency of present oil rigs. The 2010 year Deepwater Horizon oil spill event has brought global awareness to the importance of drilling safety. Making the drilling process safer, less susceptible to failures, and more efficient in general is one step towards this general goal.

In Figure 1.1, a typical rotary drilling apparatus is shown. The apparatus essentially consists of the torque-generating unit, a cutting tool, and an arrangement for transferring torque between the two. The torque generating unit, also called the *rotary unit*, is

---

<sup>1</sup> [www.eia.doe.gov/neic/quickfacts/quickoil.html](http://www.eia.doe.gov/neic/quickfacts/quickoil.html)

generally located above the ground. The actual drilling process usually takes place several hundred meters below ground level. The mechanism used to transfer the torque between the torque generating unit and the cutting tool is typically a series of connected, hollow steel drill pipes called the *drill string*. Each pipe can be 9 meters long, and a threaded connection connects two drill pipes. The drill string is a long, slender structure that is attached to a short heavier segment containing a cutting tool at the free end. This cutting tool is called a *drill bit* and this heavy segment along with the tool is called the *bottom hole assembly* (BHA). Although details are not shown in Figure 1.1, the short heavy segment may contain what are called stabilizers to minimize lateral motions during a drilling operation.

The drill string is driven in a rotary fashion from the top end, usually, by means of an electric motor and a gearbox unit called the *top drive* or the *torque generating unit* or *rotary unit*, and this string is sent at a prescribed rate through a rotating mass (the rotary) near the ground level. This system is designed to construct a borehole from the earth's surface to a reservoir of oil or gas. The borehole is lined (usually with steel) and the excess in the diameter of this cavity over the diameter of the drill pipe is called the *over gauge*. This annular gap, which varies along the length of the borehole is necessary for fluid conduction.

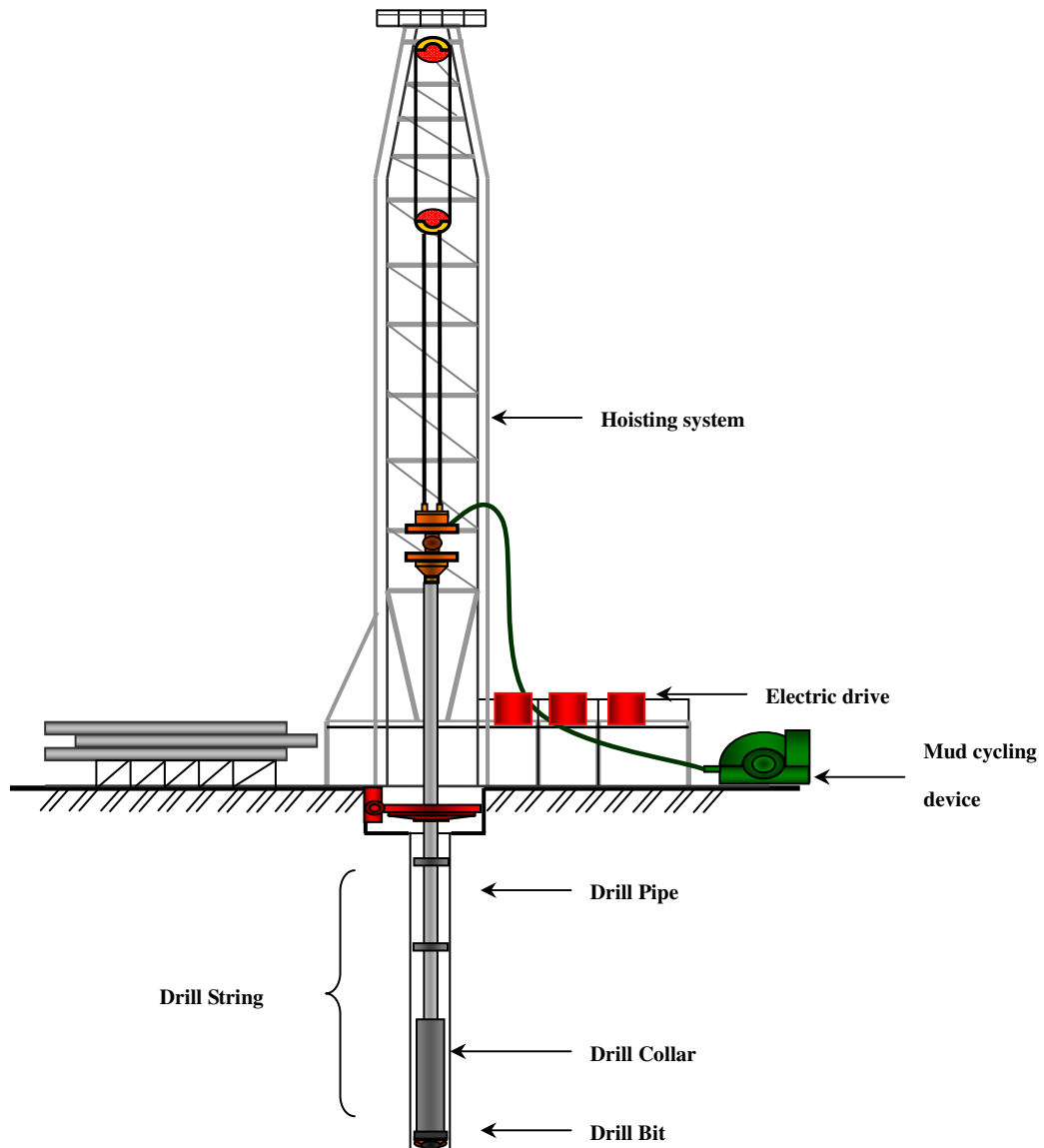


**Figure 1.1:** Schematic of a rotary drill rig. Many details such as sensors and stabilizers used in the bottom hole assembly are not shown in this figure. The height from the top to the ground is typically about 30 to 80 m, from the rotary table that houses the electric drive to the BHA is about 1000 to 8000 m, and the BHA is about 100 m to 300 m long (Leine, van Campen, and Keultjes, 2002).

This fluid is a source of external interaction along the drill string in addition to gravity and the bore liner. During a drilling operation, pressurized fluid (called *mud* or spud mud in the field<sup>2</sup>) is continuously circulated down the center of the drill string, out of holes in the drill bit and back to the surface via the space between the rotating drill string and the surface of the bore hole. This is done to cool the drill bit as well as to lubricate it and remove rock (shale) cuttings produced by the bit. These cuttings are filtered out by using what are called shale shakers, and the filtered mud is returned to the mud pits. This drilling system is naturally prone to dynamic instabilities that are not fully understood.

From information obtained in the field, it is known that drill-string washouts (cracks in drill strings) occur twice per week and drill-stem separations occur one in seven wells and that more than 40% of the drill-stem separations are related to drill-string failures. Most of the failures are reported to occur in the BHA region (Spanos, Chevallier, Politis, and Payne, 2003). It has been reported that the cost of drilling a well can be measured in tens of millions of dollars (Macdonald and Bjune, 2007). The incidence of down-hole failure of a drill string can further increase this cost. This cost associated with lost time (to recover the drill string from the well and recommence drilling) and the

---

<sup>2</sup> [http://en.wikipedia.org/wiki/Drilling\\_mud](http://en.wikipedia.org/wiki/Drilling_mud)

material cost of the damaged drill-string elements can be very high. In particular, this is true when the failure of a drill string is not detected at the washout stage and complete separation subsequently takes place down hole. In Figure 1.2, two types of failures are shown, one associated with a stem separation at a threaded connection and another associated with a crack in the drill stem. These failures can result from the stresses produced during the drill string vibrations as well as the abrasive action of the drill mud.



**Figure 1.2:** Drill-string failure types: photographs<sup>3</sup> of drill string failures with a stem separation shown on the left and a cracked drill stem (washout failure) on the right. The stem separation on the left could be due to torsion vibrations while the cracked drill stem may be due to bending vibrations.

---

<sup>3</sup> Courtesy, National Drilling Company, Abu Dhabi, UAE

In Section 1.1, models used to describe drill-string vibrations are briefly reviewed, and following that stick-slip behavior is briefly reviewed in Section 1.2, and other aspects of nonlinear oscillations such as nonlinear interactions are discussed in Section 1.3. Following that, in Section 1.4, the dissertation research objectives are presented, and finally, the organization of this dissertation is outlined in the last section of this chapter.

## **1.1 Drill-String Vibration Studies**

A drill string undergoes different types of vibration during a drilling operation. These include the following: i) axial or longitudinal vibrations, which are mostly due to the interaction between the drill bit and the rocks, ii) bending or lateral vibrations, often caused by drill-pipe eccentricity, leading to a rotational motion named as drill string whirl, iii) torsion vibrations (sometimes referred to as stick-slip vibrations in the literature because stick-slip interactions are the main source of torsion vibrations), caused by nonlinear interaction between the bit and the rock and/or the drill string with the bore hole wall, and iv) hydraulic vibrations in the circulation system, stemming from pump pressure pulsations. The hydraulic vibrations are not considered to be a main source of drill-string vibrations.

Drill-string vibrations are complicated and coupled. Over the last two decades, an extensive number of modeling, simulation, and experimental studies have been conducted to understand these vibrations (Aarrestad, Tonnesen, and Kyllingstad, 1986; Kyllingstad and Halsey, 1988; Cook, Nicholson, Sheppard, and Westlake, 1989; Jansen, 1991; Berlioz, der Hagopian, Dufour, and Draoui, 1996; Yigit and Christoforou, 1996, 1998; Christoforou and Yigit, 1997, 2003; Tucker and Wang, 1999; Leine, van Campen, and Keultjes, 2002; Melakhessou, Berlioz, and Ferraris, 2003; Spanos *et al.*, 2003; Mihajlović, van Veggel, van de Wouw, and Nijmeijer, 2004; Mihajlović, van de Wouw, Rosielle, and Nijmeijer, 2007; Ritto, Soize, and Sampaio, 2009).

Aarrestad, Tonnesen, and Kyllingstad (1986) and Cook *et al.* (1989) reported some of the first experimental results on drill-string vibrations. Kyllingstad and Halsey (1989) focused on the stick-slip phenomenon associated with torsion vibrations, which were modeled by using a single degree-of-freedom (DOF) system. Berlioz *et al.* (1996) conducted experiments to examine the coupling between transverse (lateral) and axial vibrations. Yigit and Christoforou (1996) and Christoforou and Yigit (1997) focused on modeling the coupling between transverse and axial vibrations.

Jansen (1991) modeled the bottom hole assembly as an unbalanced rotor supported by two bearings. By using this model, effects of nonlinearities due to friction and gap

between the outer shell and whirling motions of the drill string were studied. The work of Melakhessou, Berlioz, and Ferraris (2003), in which a four degree-of-freedom model is presented to study the bending and torsion motions of the drill string as well as the interactions with the outer shell, builds on the work of Jansen (1991). This model is further discussed in Chapter 3 as well as in Appendix B. Melakhessou *et al.* (2003) also reported experimental results, but their experiments as well as the comparisons between the simulation results and experimental results were not complete.

Stick-slip and whirl vibrations of a drill string and the influence of the fluid lubrication on it were studied by Leine, van Campen, and Keultjes (2002). They presented a reduced-order model with two degree-of-freedom, considered contact conditions in detail, and studied bifurcations associated with discontinuities in the system. The work of Leine *et al.* (2002) illustrated the complexities of torsion drill-string dynamics including interactions between stick-slip and whirl, and the possible instabilities that can be exhibited by such systems. In a broader context, drill string systems are discontinuous systems, instabilities in which have been addressed in the book of Leine and Nijmeijer (2004). Mihajlović *et al.* (2004, 2007) conducted a series of experiments to understand friction-induced vibrations and self-sustained lateral vibrations caused by a mass imbalance in an experimental rotor system. Mihajlović *et al.* also

carried out numerical investigations and showed that there two types of torsion vibrations and discussed coupling between torsion and lateral vibrations. They studied the effect of contact and the unbalanced mass on the system bifurcations. However, they do not consider the effect of axial vibrations in their work.

Finite element analysis studies have also been carried by using linear models (e.g., Khulief Al-Naser, 2005) to determine buckling loads and critical rotational speeds. Spanos *et al.* (2003) focused on the lateral vibrations of the drill string by using a finite element model. They did not consider drill-string rotation in their work. An illustration of the use of Cosserat mechanics to study drill-string vibrations is provided by Tucker and Wang (1999). This mechanics can be useful for studying nonlinear motions of a drill string. However, Tucker and Wang (1999) do not examine the instabilities exhibited by the system. In the recent study, Ritto, Soize and Sampaio (2009) construct a distributed-parameter or continuous model and use this model to study the axial vibrations.

Navarro-Lopez and Cortes (2007) have discussed that axial motions can lead to failures in a drill system. They focus on the drill-bit dynamics and study possible failures of the drill bit due to torsion, axial, and lateral oscillations. Self-excited stick-slip oscillation and sticking phenomena of the drill bit have also been studied in prior efforts

(e.g., Richard, Germy, and Detournay, 2004). The results of Richard *et al.* (2004) indicate that by changing the weight on the bit (WOB) and the rotation speed of the drill string, undesired nonlinear oscillatory phenomena can be avoided.

Although different models have been developed and studied to understand stick-slip vibrations, whirl vibrations, axial vibrations, and lateral vibrations, given the complexity of the dynamics, a comprehensive nonlinear treatment of this problem remains to be conducted. In addition, different possible nonlinear phenomena have not been fully explored, as most of the experiments have tended to focus on either lateral or torsion vibrations. In the prior experimental studies conducted in a laboratory setting, the drill string is fixed at the bottom to a rotating disc, which is not representative of the conditions in the field where the end of a drill string has freedom to move around. Moreover, the interaction forces along the axial direction between the drill bit and the soil and rocks have also not received full consideration. A combined analytical, experimental, and numerical effort is needed to gain further insights into the vibrations of the BHA assembly and relate them to failures such as those shown in Figure 1.2.

## **1.2. Stick-Slip Behavior**

Apart from the context of drill-string dynamics, stick-slip vibrations have been studied in

the context of many other systems. They have been studied as oscillations induced by dry friction; for instance, the sound produced by vibrations of a bowed instrument (e.g., Popp and Stelter, 1990). A common dry friction model that is used is a discontinuous model with Coulomb friction. This model has a switch that determines when a friction force acts on the system and when it does not. Karnopp (1985) proposed a stick-slip friction model on the basis of force balance and used this model to understand how the friction force depends on the relative velocity between the contacting surfaces. Various versions of the Coulomb and Karnopp models have been used in the literature to study contact dynamics (e.g., Awrejcewicz and Olejnik, 2005; Duan and Singh, 2006). Leine, van Campen, de Kraker, and Van den Steen (1998) have presented alternate friction models. Stick-slip behavior is important in many macro-scale mechanical problems (Pfeiffer and Glocker, 1996; Crowther and Zhang, 2005) as well as micro-scale ones (e.g., Bockelmann, Essevaz-Roulet, and Heslot, 1997).

### **1.3. Nonlinear Oscillations and Interactions**

From the discussion of Sections 1.1 and 1.2, it is clear that the dynamics of a drill string is nonlinear and complex. The system has features of non-smoothness (e.g., Leine and Nijmeijer, 2004) and this system is capable of exhibiting a wide variety of nonlinear

behavior (e.g., Nayfeh and Balachandran, 1995) including qualitative changes with respect to friction and rotational speed of the drill string. The coupling amongst torsion, lateral, and axial vibrations has not received full consideration, and it is possible that nonlinear interactions exhibited by other mechanical and structural systems (e.g., Nayfeh and Balachandran, 1989) also exist in this system. This remains to be studied and understood along with the stick-slip phenomenon mentioned in Sections 1.1 and 1.2. Different nonlinear behavior exhibited by rotors and discs (e.g., Mottershead, 1998; Popprath and Ecker, 2007) may also be relevant to the drill-string problem. Furthermore, the drill-string problem does share many similarities with the milling dynamics problem (e.g., Long, 2006; Long and Balachandran, 2007). However, the interactions between loss of contact dynamics and delay dynamics have not received the same consideration. Nonlinear instabilities such as grazing instabilities in impacting systems (Long, Lin, and Balachandran, 2007) may also be important for understanding the interactions between a drill string and an outer shell or well bore.

## **1.4 Objectives and Scope of Work**

The overall goal of the work is to obtain a fundamental understanding of drill-string dynamics through a combined experimental, analytical, and numerical effort and also

apply this understanding to other systems with similar characteristics. Specific objectives include the following:

- i) understand stick-slip behavior when two flexible surfaces or one flexible surface and a rigid body are in contact
- ii) study existing reduced-order models such as those proposed by Melakhessou *et al.* (2003) and develop them further with careful attention to contact dynamics and stick-slip behavior between a drill string and the outer shell as well as between a drill bit and bottom of the well
- iii) construct an experimental arrangement to study coupling between bending and torsion motions as well as to explore interactions between a drill string and outer shell and a drill bit and well bottom, validate model predictions, and uncover new dynamics and new phenomena
- iv) propose guidelines to mitigate drill-string failures.

## **1.5 Organization of Dissertation**

In the next chapter, a lab-scale experiment arrangement is presented as well as the characteristics of rotor dynamics observed throughout experimental work. The aspects of this arrangement that make it unique are also detailed. The design and component details

are provided in Appendix A. In the third chapter, reduced-order models studied by the author are presented and simulation results obtained by using these models are discussed. These models include four degree-of-freedom and five degree-of-freedom models. Special attention is paid to contact between the drill string and the outer shell, and how it is modeled. The model predictions are compared with experimental results generated by the author as well as others in the literature. Related details on the derivation of the four degree-of-freedom model are provided in Appendix B and one example of simulation program by Matlab is shown on Appendix C. In the fourth chapter, parametric studies undertaken through experiments and numerical efforts are presented, and the results are used to suggest guidelines for practical drilling operations. In the last chapter, a summary of this dissertation work is presented and recommendations for future work are made. Three appendices relevant to this dissertation are included, and a bibliography that was useful for this dissertation work is also presented.

## **Chapter 2**

### **Experimental Studies**

Mihajlović *et al.* (2007) performed a series of experiments focusing on the interaction between friction-induced vibration and self-sustained later vibrations in an experimental rotor dynamic setup. The work mainly discusses the response of a rotor subject to a friction force applied along the torsion direction in a string with clamped ends, one mounted to a motor and another mounted on to a friction disc. In a similar effort, Khulief *et al.* (2009) presented a lab-scale experiment focused on the influence of stick-slip, the well-borehole contact, drill-fluid interaction, and weight on bit. Expanding on the idea of a string fixed at both ends, here, a string fixed to a motor on one end but free on the other has been put together in this dissertation effort. This is a principal feature of the present experimental work. This feature allows for a simultaneous study of both rotor and contact dynamics. The drill-system has been studied in various settings to examine the rotor

response, when the system is subjected to different frictional forces and driving speeds.

In this chapter, the experimental approach used for studying the dynamics of the drill-string system is described. The experimental setup along with a detailed description is provided in Section 2.1. The sensors used, their arrangement, and the image processing scheme used to determine the position of the rotor are reported in Section 2.2. This type of visualization of rotor dynamics has not been carried out before. Experimental results, which are descriptive of the rotor movements and trajectories, are presented and explained in Section 2.3.

## **2.1 Design and Arrangement**

In this section, the experimental arrangement construction is described. The drill-string has been simplified as a thin rod with two discs on either end. This arrangement is used to validate the models presented in modeling section later as well as to uncover drill-string dynamics and explore control strategies. A detailed design has been carried out as shown in Figure 2.1, Figure 2.2, and Figure 2.3. The main testing apparatus is built on a rectangular frame with two feet by two feet in length and width, as shown in Figure 2.1. The cross-section size of each column and beam is two inches by two inches and these components are made from aluminum material. The height of the main structure is six

feet. The two plates mounted on the top and in the middle of the frame are for mounting the driving motor and test bed, respectively.

The experimental system, which is approximately a 25:1 scaled down version of an actual drill-string system in terms of the drill-string diameter, is shown in Figure 2.2 and Figure 2.3 (a) and (b) (Liao *et al.* 2009, 2011). This test arrangement represents one section of the drill string with stabilizers at both ends. A slender aluminum rod with quarter inch diameter is driven by a DC motor from the top of the rigid frame, which represents the drill string under the ground. A tunable speed motor is used to drive the system at the top, as shown in Figure 2.3 (d). In order to maintain a constant rotating speed, the motor is connected to a rigid disc eight inches in diameter, and a custom connector secures the rod to the disc. The disc on the top represents the stabilizer of the drill-string system in Figure 2.3 (e). In Figure 2.3 (c), two eleven bit absolute encoders are used, with one at the top and another at the bottom of the drill string that are used to measure the rotations of the top and bottom discs, respectively. The bottom disc can be representative of either another stabilizer in a drill-string pipe or the drill bit of the bottom hole assembly.

In Figure 2.3 (f), an unbalanced mass attached to the bottom disc is used to mimic the curvature of the drill string during a drilling process. The unbalanced mass creates

lateral forcing into the system where subjected to rotation. An outer shell is used to simulate the borehole, and to study stick-slip interactions between the drill string and the outer shell. The outer shell has an outer diameter of eight inches and a wall thickness of 0.2 inches. A camera mounted near the top disc captures the movement of the bottom disc (Figure 2.3(c)). The rotor is expected to collide with the outer shell when it experiences large lateral displacements; stick-slip vibrations are also likely to occur during contact with the outer shell.

For studying the effects of friction and its influence on the system, different combinations of rotor peripheral material and outer shell surface material have been considered. The different contact surface combinations considered are aluminum-aluminum (Al-Al) combination, rubber-aluminum (R-Al) combination, and rubber-rubber (R-R) combination. These combinations correspond to low to moderate and high levels of friction, respectively.

With this experimental arrangement, the studies have allowed the author to investigate the influence of contact between the drill string and the outer shell as well as nonlinear effects. Additional details are provided in Appendix A.

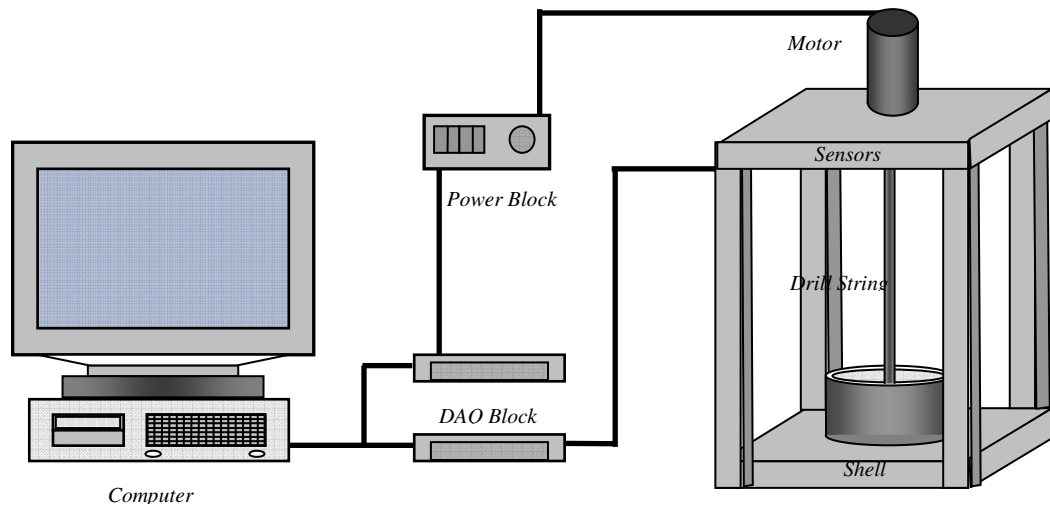


**Figure 2.1:** Schematic of drill string experimental setup.

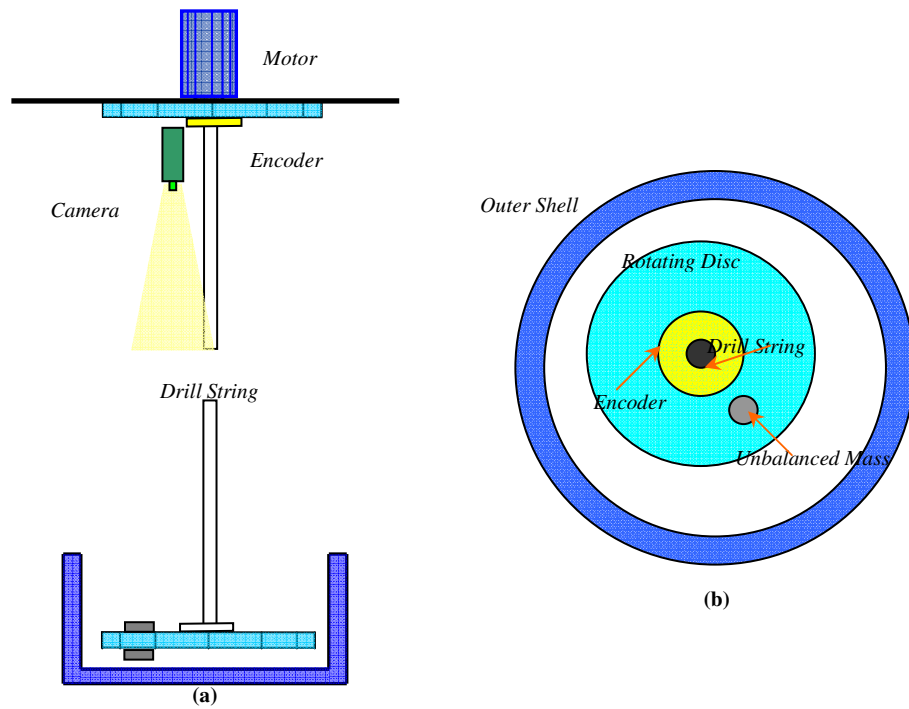


**Figure 2.2:** Experimental setup: (a) side view and (b) top view.

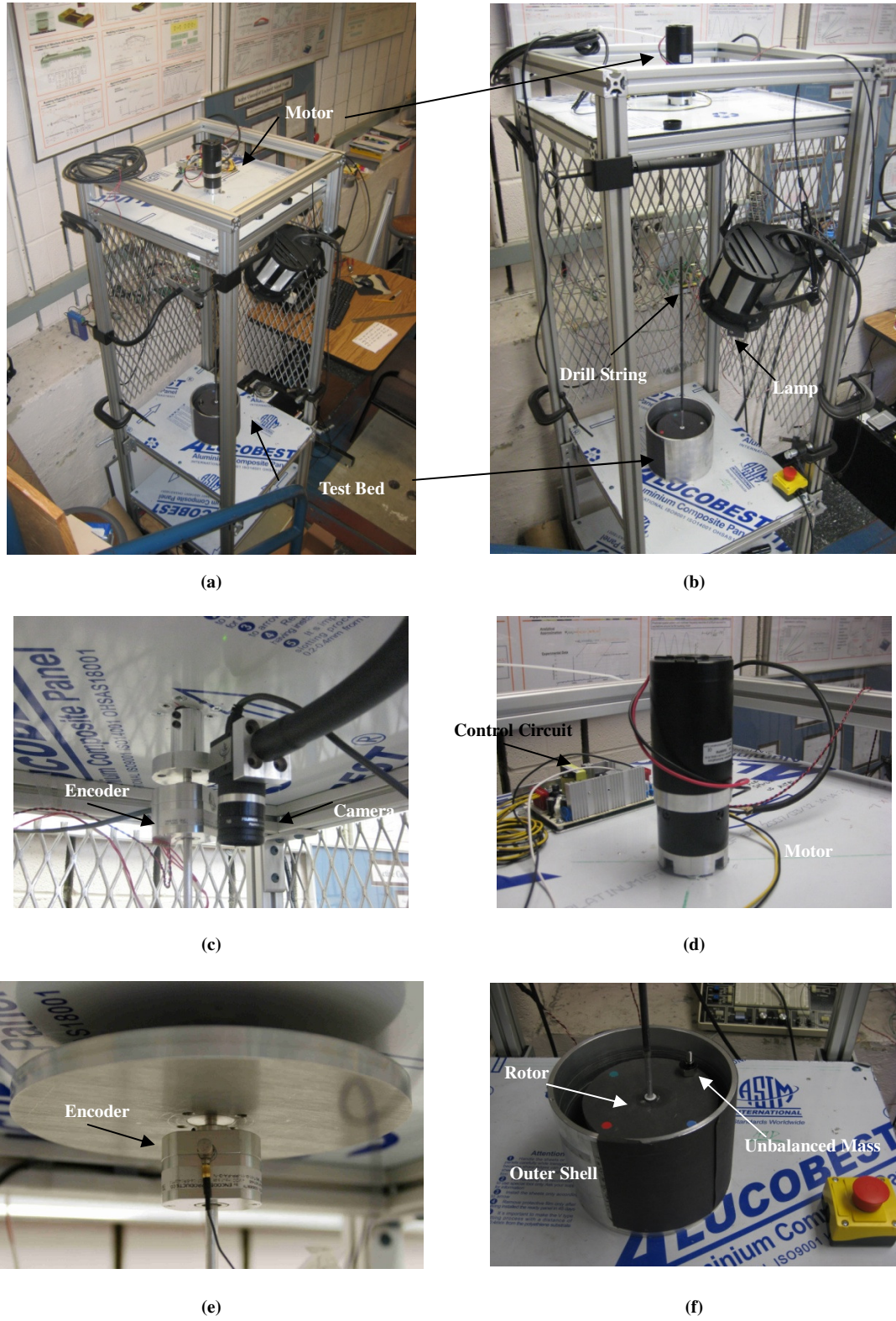


**Figure 2.3:** Components of experimental setup: (a) overall setting, (b) system

components, (c) camera, (d) DC motor, (e) encoder, and (f) test bed (unbalanced mass, bottom disc and outer shell).

## **2.2 Experimental Data Collection and Results**

Results of the rotor dynamics are presented in this section. Characteristic rotor motions include rolling and bumping motions. Studying the sources of these behaviors as well as how they influence the system is an important aspect of the experiments. The rotor movements are captured using a video camera, and the trajectories are determined using an imaging processing technique.

### **2.2.1 Results at first glance**

Experimental observations of rolling motions and bumping motions are shown in Figure 2.4 and Figure 2.5, respectively. The first case corresponds to the low rotation speed, while the second one corresponds to a high rotation speed. With a heavier unbalanced mass, rolling motions are observed. Some of these characteristics have also been reported in previous work [Leine *et al.* 2002, Melakhessou *et al.* 2003, Mihajlović *et al.* 2004].

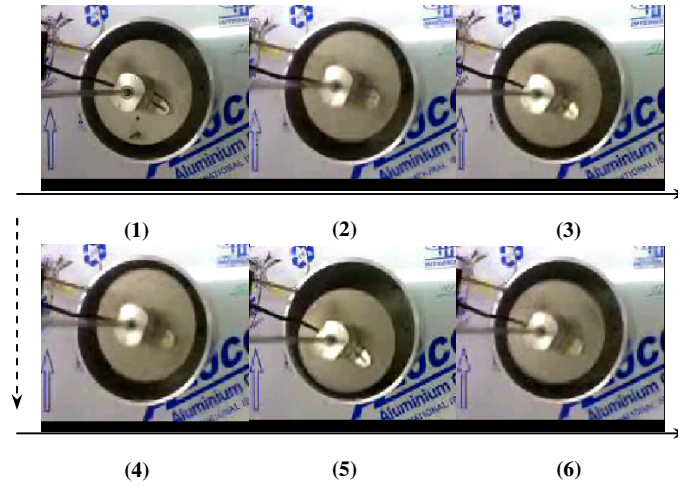


**Figure 2.4:** Rotor in bumping motion.

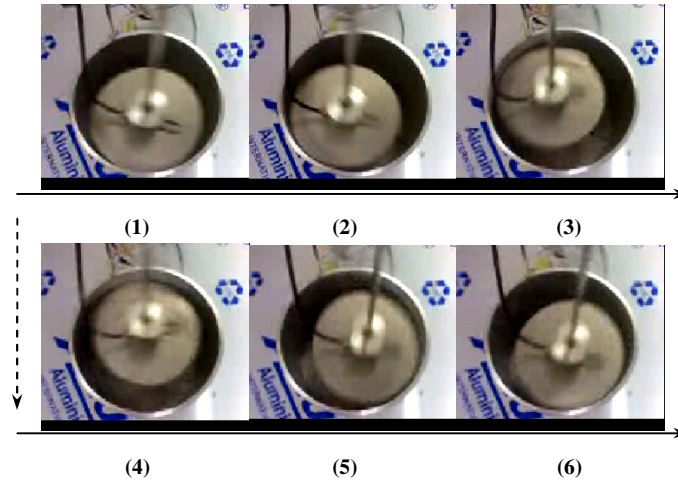


**Figure 2.5:** Rotor in rolling motion.

The rotor motions as observed at a low-motor speed and a high-motor speed are reported here. The driving speed from the motor plays a determining role in the type of rotor response observed. The experiments have been conducted to collect quantitative data for analysis and model validation as well as to gain an understanding of the rotor dynamics.

## **2.2.2 Image processing**

Image processing is a means to translate an image to a set of numerical data (Russ, 2006).

The method has been applied in several research fields including medical imaging of retina (Staal, Abramoff, Niemeijer, Viergever, and van Ginneken, 2004) and gait based human identification (Wang, Tan, Ning, and Hu, 2003). Although image processing is a complicated procedure, in the present context, it can serve as a powerful tool to understand the rotor motions in the plane by processing the video data clips.

In Figure 2.6, a set of representative image examples used to locate the rotor on a plane is shown. The image shown in Figure 2.6 (a) is the original image of the rotor position, as obtained from the camera. By dropping the color information, the image is translated to the black and white image shown in Figures 2.6 (b) and (c). A black and white image is easier for distinguishing one feature from another since it has high

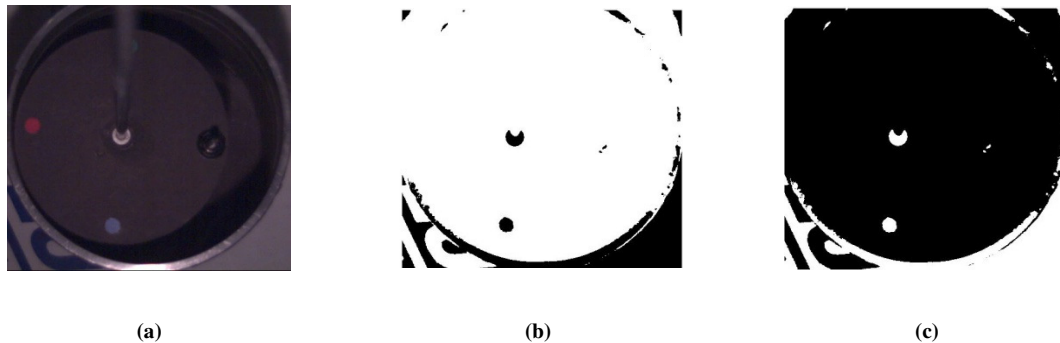


**Figure 2.6:** Representative images from drill-string experiments.

contrast. By targeting the center of string which is the black dot at the center of Figure 2.6 (b) or the white dot in the center of Figure 2.6 (c), the position of the rotor can be located.

## **2.3 Rotor Response Observations**

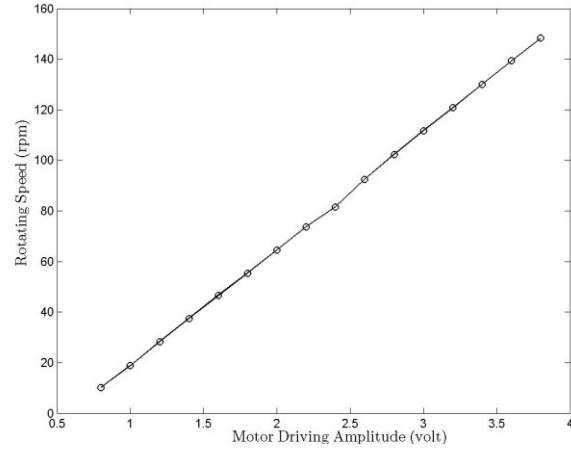
In the previous section, the rotor motions were categorized as rolling and bumping motions. The driving speed of the system plays an important role in determining the type of motion observed. In this section, details of the different observed rotor motions for different rotations speeds are discussed.

### **2.3.1 Rotor motions at different rotation speeds**

Experimental results obtained at different rotating speeds are detailed in this section. Different levels of rotation speed are provided by using a DC (direct current) motor, which responds in a linear fashion to the voltage input. The corresponding relationship is shown in Figure 2.7. This relationship is curve fit to obtain the equation  $DS = 46.005 \cdot (V_{volt} - 0.8) + 10.2$ , where  $DS$  represents the motor drive speed output in and  $V_{volt}$  is the input voltage from the control circuit.

The experiments conducted initially cover sixteen values of the driving speed from 10 rpm (revolutions per minute) to 150 rpm in 9.33 rpm increments. However, the actual rotation speed varies from case to case due to hardware and experimental complications.

$V_{volt}$ (volt)	$DS$ (rpm)	$V_{volt}$ (volt)	$DS$ (rpm)
0.8	10.2	2.4	81.63
1.0	18.82	2.6	92.55
1.2	28.27	2.8	102.33
1.4	37.5	3.0	111.71
1.6	46.57	3.2	120.73
1.8	55.35	3.4	130.02
2.0	64.82	3.6	139.27
2.2	73.75	3.8	148.22



$$DS = 46.005 \cdot (V_{volt} - 0.8) + 10.2$$

**Figure 2.7:** Motor driving voltage to rotation speed relationship.

In the experiments, the string is rotated from 10.2 rpm to 148.22 rpm in 9.201 rpm increments. Additionally, a 28 gram unbalanced mass has been attached onto the rotor to generate lateral forcing.

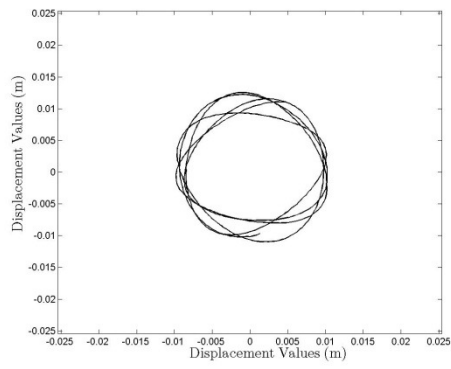
Rotor trajectories obtained for various levels of rotation speed are shown in Figure 2.8. The trajectories represent the location of drill string, or similarly, the rotor center. Here, six cases are used to describe the rotor motions in different stages.

In Figure 2.8 (a), the rotor is rotating around the center of the shell, where the shell boundary is a circle with radius of 0.195 m. With an increase in the rotation speed, the rotor moves closer to the edge of outer shell and starts bumping and rotating around the outer shell as seen in Figure 2.8 (b). This portion of the trajectory with corners and sharp angles represents bumping and the smooth curve represents rotation around the shell.

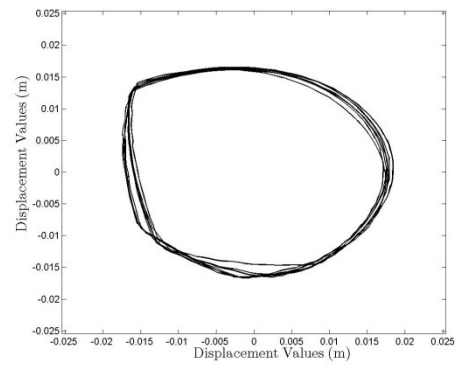
With a further increase in the rotation speed, the rotor moves closer to the edge of shell.

The trajectory shown in Figure 2.8 (c) is illustrative of mostly rotations around the edge rather than bumping. This behavior is called forward whirl, which means the disc is orbiting the center of the shell in the direction that the motor is turning (Swanson, Powell, and Weissman, 2005).

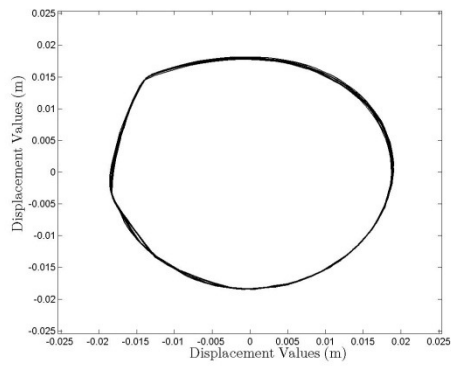
In Figure 2.8 (d), the rotor motions show bumping characteristics followed by backward whirling motions. In contrast with forward whirling, when backward whirling occurs, the rotor orbits the center in the opposite direction to the disc rotation (Swanson *et al.*, 2005). After bumping followed by backward whirling phase, with an increase in the rotation speed, the rotor goes back to rotation around the center of shell as illustrated in Figures 2.8 (e) and (f). In short, as the drive speed is quasi-statically increased, the rotor starts rotating around the center, then transitions to a bumping-forward whirl phase followed by a bumping-backward whirl phase and finally a return to a rotation around the center.



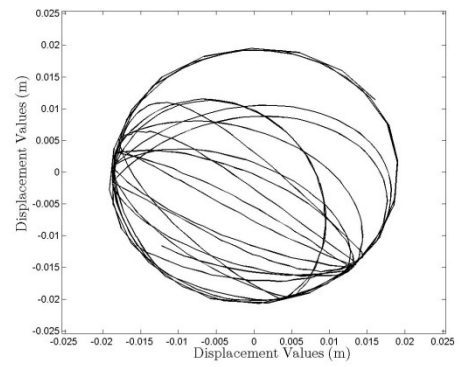
(a)



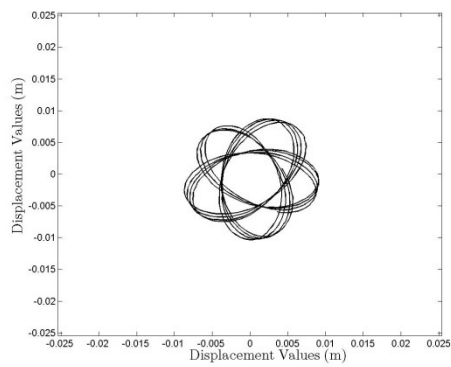
(b)



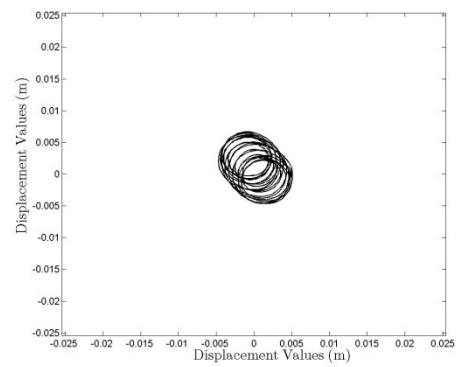
(c)



(d)



(e)



(f)

**Figure 2.8:** Rotor trajectories for different rotation speeds with rubber-aluminum contact:

(a) 37.5 rpm (revolutions per minute), (b) 55.4 rpm, (c) 73.8 rpm, (d) 81.6 rpm, (e) 92.5 rpm, and (f) 148.2 rpm.

### **2.3.2 Rotor response about center and forward whirling phase**

In the last section, the rotor behavior was divided into several phases corresponding to its driving speed and the characteristics associated with each phase were discussed.

In Figure 2.9(a), the rotor response is shown when the rotor is driven at 37.5 rpm, the system has 28 grams of unbalanced mass and there is aluminum-aluminum contact between the rotor and outer shell. The sole difference between this case and the case of the previous section is in the contact surface material. The friction coefficient is expected to be lower in the present aluminum-aluminum (Al-Al) case than in the previous rubber-aluminum (R-Al) case. However, the actual friction coefficient of each contact surface combination is difficult to measure in the experiment. When the rotor does not make contact with the outer shell, the type of contact surface has no effect on the system. In such no-contact cases, there is no bumping between the rotor and the outer shell, and the rotor trajectory in Al-Al case shows a similar pattern as observed for the R-Al case. From the time history of the radial displacement illustrated in Figure 2.9 (b), it is clear that there is no sign of contact with the shell, since the displacement is approximately 0.01 m and the shell is located around 0.02 m. The amplitude of the radial speed history

depicted in Figure 2.9(c) is small, since the driving speed is slow. The displacement components of the rotor along the normal and tangential directions of the rotor is sinusoidal in nature with a phase difference; the corresponding frequency spectra shown in Figure 2.9(d) feature a prominent peak at the motor driving frequency.

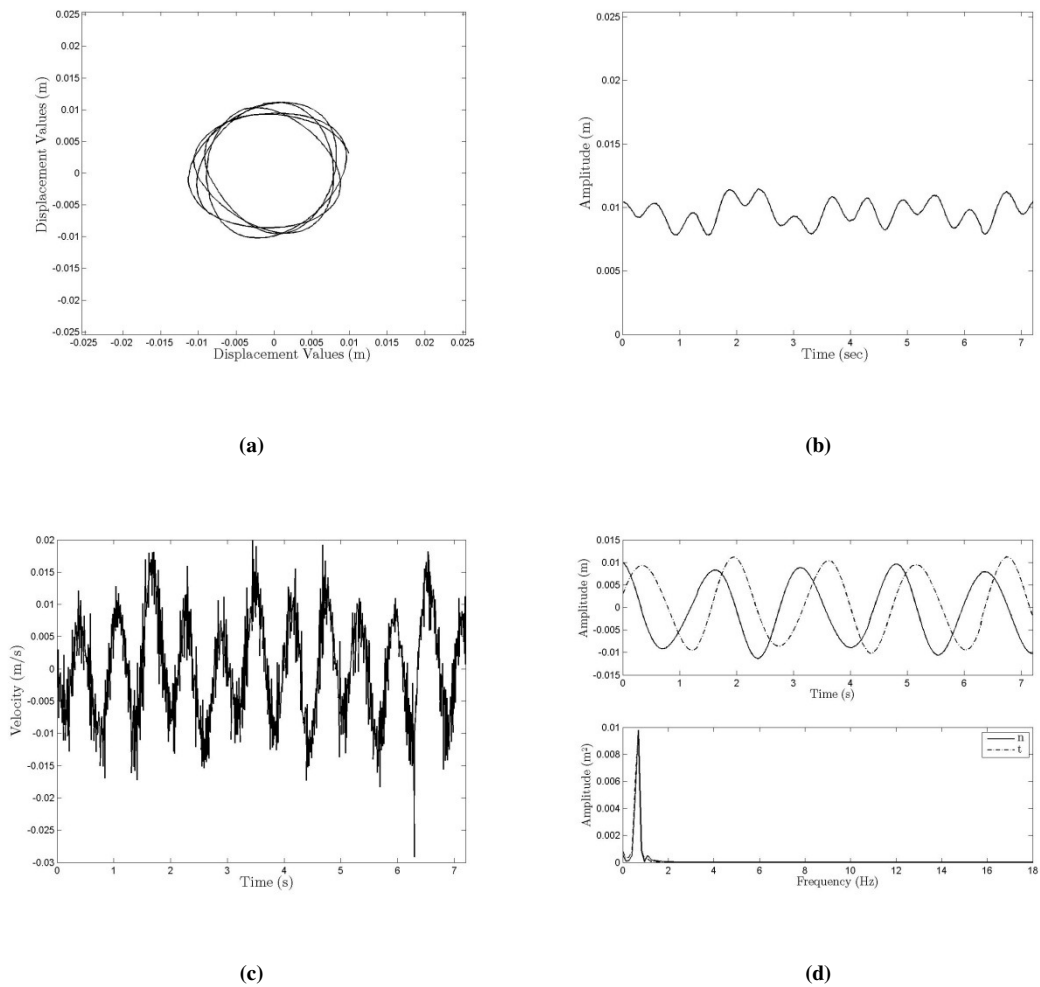


**Figure 2.9:** Rotor response for rotating speed of 37.5 rpm with aluminum-aluminum contact: (a) rotor trajectory, (b) radial displacement history, (c) time histories of normal and tangential speeds, and (d) normal and tangential displacement histories (top) and

corresponding frequency spectra (bottom).

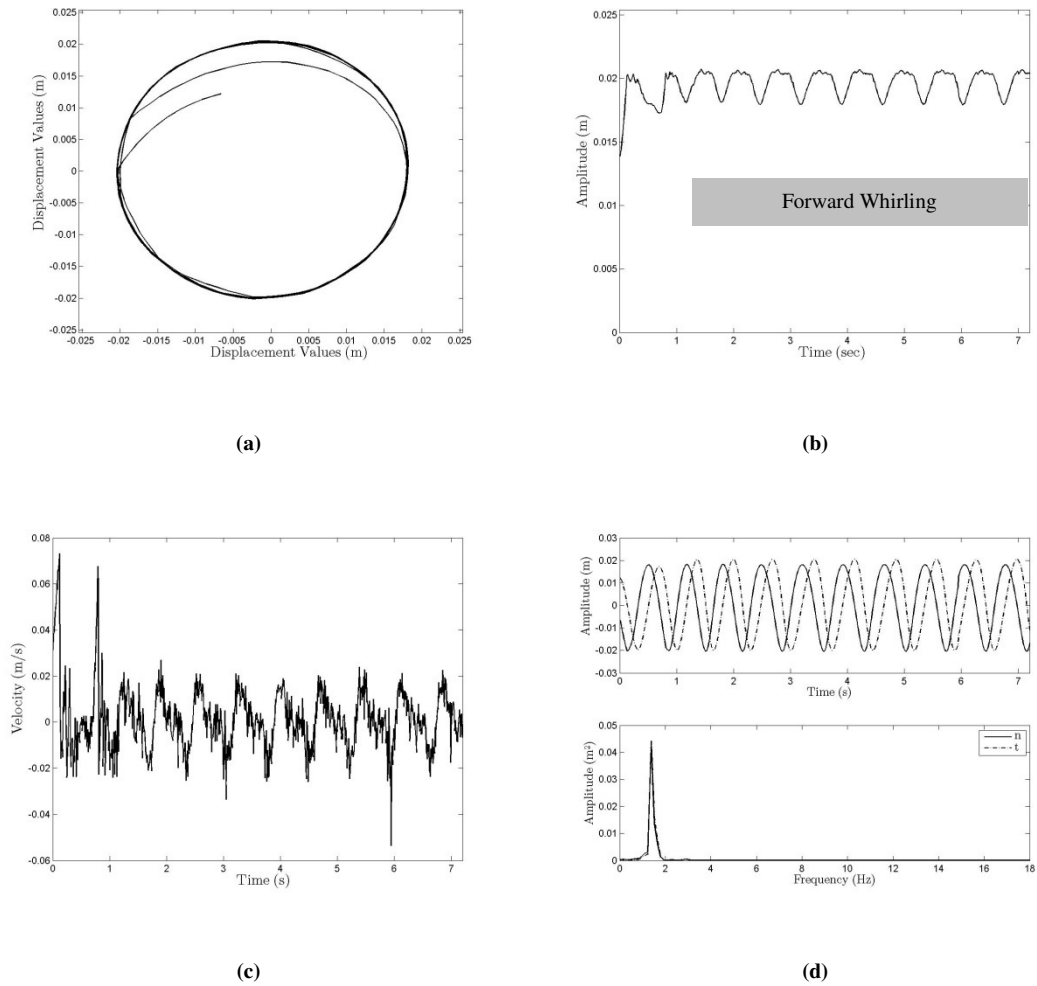


**Figure 2.10:** Rotor response for rotating speed of 83.1 rpm with aluminum-aluminum contact: (a) rotor trajectory, (b) radial displacement history, (c) time histories of normal and tangential speeds, and (d) normal and tangential displacement histories (top) and corresponding frequency spectra (bottom).

With an increase in rotation speed, the rotor goes into a bumping and forward whirling phase. The rotor response shown in Figure 2.10 (a) features more than two

impacts with the outer shell before going into forward whirling. In the forward whirling phase, the radial displacement history has a small amplitude sinusoidal component and a DC offset close to the outer shell, as shown in Figure 2.10 (b).

In Figure 2.10 (c), the first two peaks observed in the radial velocity time history are associated with the bumping of the rotor into the shell. After the impacts, when the rotor goes into forward whirling, the radial velocity amplitude drops close to zero. It should be noted that the velocity amplitude of forward whirling phase is lower than observed during the bumping stage. In Figure 2.10(d), the frequency spectra of the normal and tangential response components feature a prominent peak at the drive frequency.

### **2.3.3 Rotor response in bumping and backward whirling phases**

Here, the rotor response observed after the forward whirling phase is discussed. To understand this behavior, a rubber-rubber (R-R) contact surface is considered, as it is a high friction case compared to the Al-Al and R-Al cases. For consistency, the imbalance mass level is kept at 28 grams, as in the previous experiments.

As the rotor speed is increased, the rotor goes from a forward whirling phase to a bumping phase. Again, when bumping occurs, the rotor starts bounces on and off the shell edge; the trajectories form sharp corners which can be observed in the rotor

trajectory of Figure 2.11(a). In Figure 2.11 (b), the first response peak is associated with

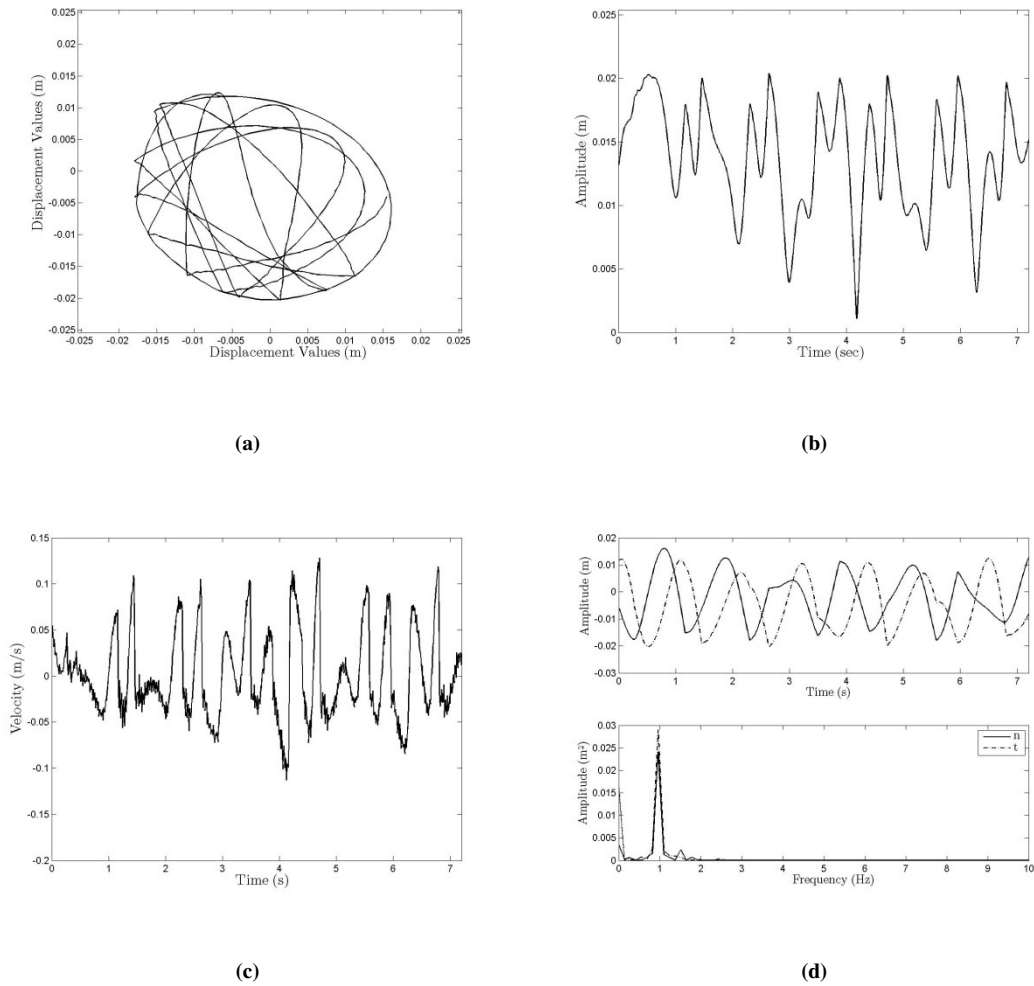


**Figure 2.11:** Rotor response for rotating speed of 55.6 rpm with rubber-rubber contact -I:

(a) rotor trajectory, (b) radial displacement history, (c) time histories of normal and tangential speeds, and (d) normal and tangential displacement histories (top) and corresponding frequency spectra (bottom).

forward whirling of the rotor followed by subsequent bumping. During the bumping phase, the radial speed component has a higher amplitude than during the forward

whirling phase, as can be discerned from Figure 2.11 (c). The normal direction

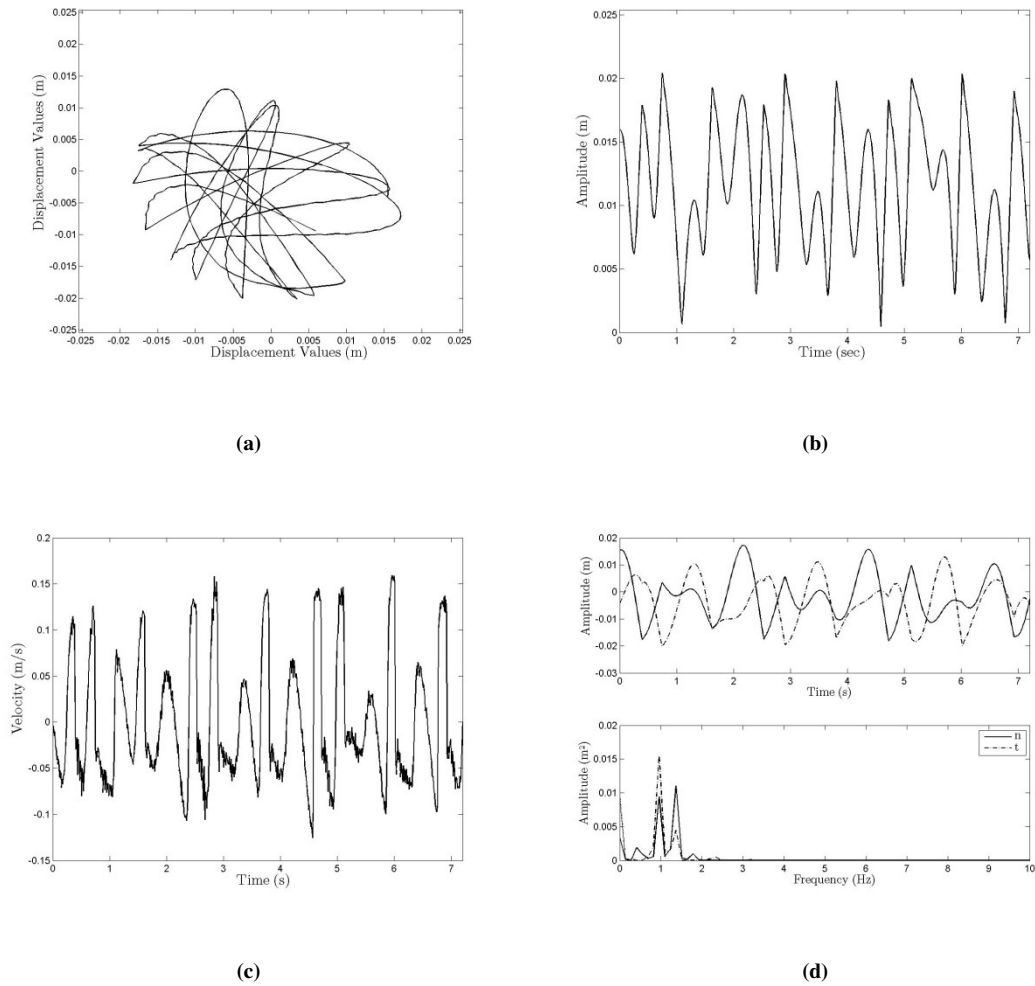


**Figure 2.12:** Rotor response for rotating speed of 55.6 rpm with rubber-rubber contact -II:

(a) rotor trajectory, (b) radial displacement history, (c) time histories of normal and tangential speeds, and (d) normal and tangential displacement histories (top) and corresponding frequency spectra (bottom).

displacement component of the rotor is not sinusoidal due to the bouncing. The frequency spectra of Figure 2.11 (d) show a prominent peak at the drive frequency. A small

amplitude peak at a frequency higher than the drive frequency can be seen in the spectral plots.

A rotor trajectory in a pure bumping phase is illustrated in Figure 2.12 (a). In this phase, the rotor bumps periodically back and forth across the whole outer shell region, as shown in Figure 2.12 (b). After an impact, the amplitude of radial velocity jumps to a higher value, as can be discerned from Figure 2.12 (c). The frequency spectra of Figure 2.12(d) show two peaks, with the first peak corresponding to the motor drive frequency.

Following the bumping phase, backward whirling can occur. The rotor trajectory of Figure 2.13 (a) shows similar characteristics to those observed during forward whirling in Figure 2.10 (a). However, the dynamics is quite different. During forward whirling, the rotor does not induce an extra torque onto the drill string, since the whole string is in free body rotation, but torsion vibrations along with a high torque is thought to exist during backward whirling. One way to distinguish between forward and backward whirling is on the basis of the radial displacement time history, such as that illustrated in Figure 2.13 (b). The rotor response during a backward whirling phase exhibits a saw tooth like wave pattern whereas during a forward whirling phase, the system response has a wave pattern with a sinusoidal character and a DC offset.

Another way to discern whether a rotor is in forward or backward whirling is on the

basis of the frequency spectra, such as those shown in Figure 2.13(d). During backward

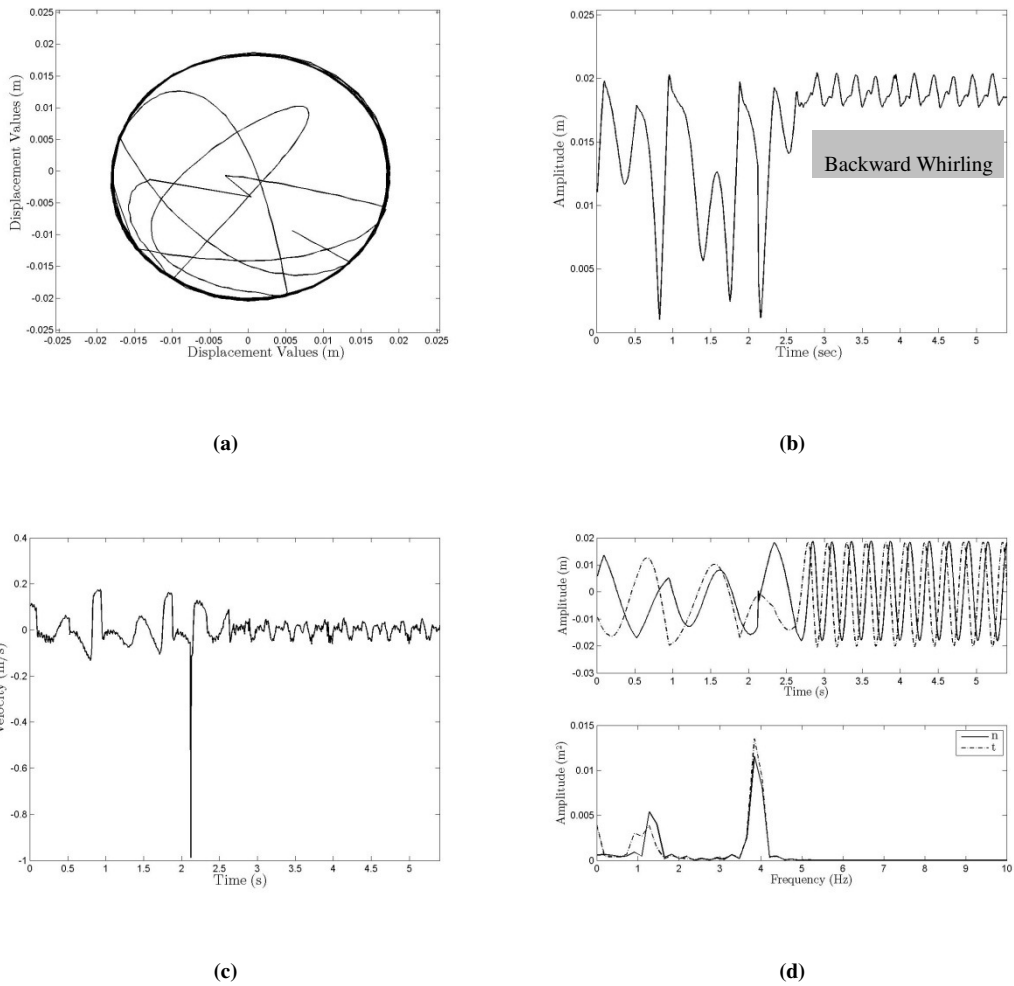


**Figure 2.13:** Rotor response for rotating speed of 55.6 rpm with rubber-rubber contact

-III: (a) rotor trajectory, (b) radial displacement history, (c) time histories of normal and

tangential speeds, and (d) normal and tangential displacement histories (top) and

corresponding frequency spectra (bottom).

whirling, there is a response frequency component that is higher than the excitation

frequency; the ratio of this frequency to the drive frequency can be determined from the

diameter of the rotor and inner diameter of the shell (Vlajic, Liao, Karki, and Balachandran, 2011). Backward whirling is important to note, as it can lead to drill-string failures. In practice, it is preferable to avoid this dynamics.

### **2.3.4 Characteristics of rotor dynamics**

In sections 2.3.2 and 2.3.3, the transition from a forward whirling phase to a bumping stage to backward whirling phase was discussed. These different phenomena can occur for the same input parameters. To illustrate this point, consider the results shown in Figure 2.14. These results have been obtained for a rotor with rubber-rubber contact, an unbalanced mass of 28 grams, and a drive speed of 55.6 rpm.

Based on observations, certain criteria have been established in order to identify the different types of behavior. During forward whirling, the radial velocity oscillates about zero, and the radial displacement is close to the border of the shell. Forward whirling characteristics can be discerned from Figures 2.14 (b) and (c). Bumping motions drive the radial velocity up to a higher level compared to that observed during forward whirling motions (see Figure 2.14(c)). During bumping, the rotor trajectory also contains sharp features (see Figure 2.14(a)).

The rotor trajectories and radial velocity histories associated with backward whirling and forward whirling share similar features. However, as mentioned before, during

backward whirling, the response has a saw tooth like wave feature, which is not so in the case of forward whirling. The frequency spectrum provides another means to distinguish between forward whirling and backward whirling. A rotor in backward whirling contains a response frequency component at a frequency higher than the excitation frequency.

Under the assumption of no slip condition, small shell deflection, and small amplitude torsion oscillations, the relationship between the excitation frequency and the frequency associated with backward whirling can be determined in terms of the geometry of rotor and outer shell (see Vlajic *et al.*, 2011). This relationship between the backward whirling frequency and the excitation frequency is given by

$$\omega_{backward} = \frac{d_{rotor}}{D_{shell\ in} - d_{rotor}} \cdot \omega_{drive} \quad (2.1)$$

where  $\omega_{backward}$  is the frequency associated with backward whirling,  $d_{rotor}$  is the diameter of the rotor,  $D_{shell\ in}$  is inner diameter of outer shell, and  $\omega_{drive}$  is the excitation frequency.

In the experiments, the observed frequency ratio is about 4.05, which is close to the value of 3.87 determined on the basis of the diameters of rotor and outer shell.

Another distinguishing criterion is on the basis of the normal and tangential velocity components of the rotor. The amplitudes of the normal and tangential velocity components are found to be higher in backward whirling compared to those observed in forward whirling.

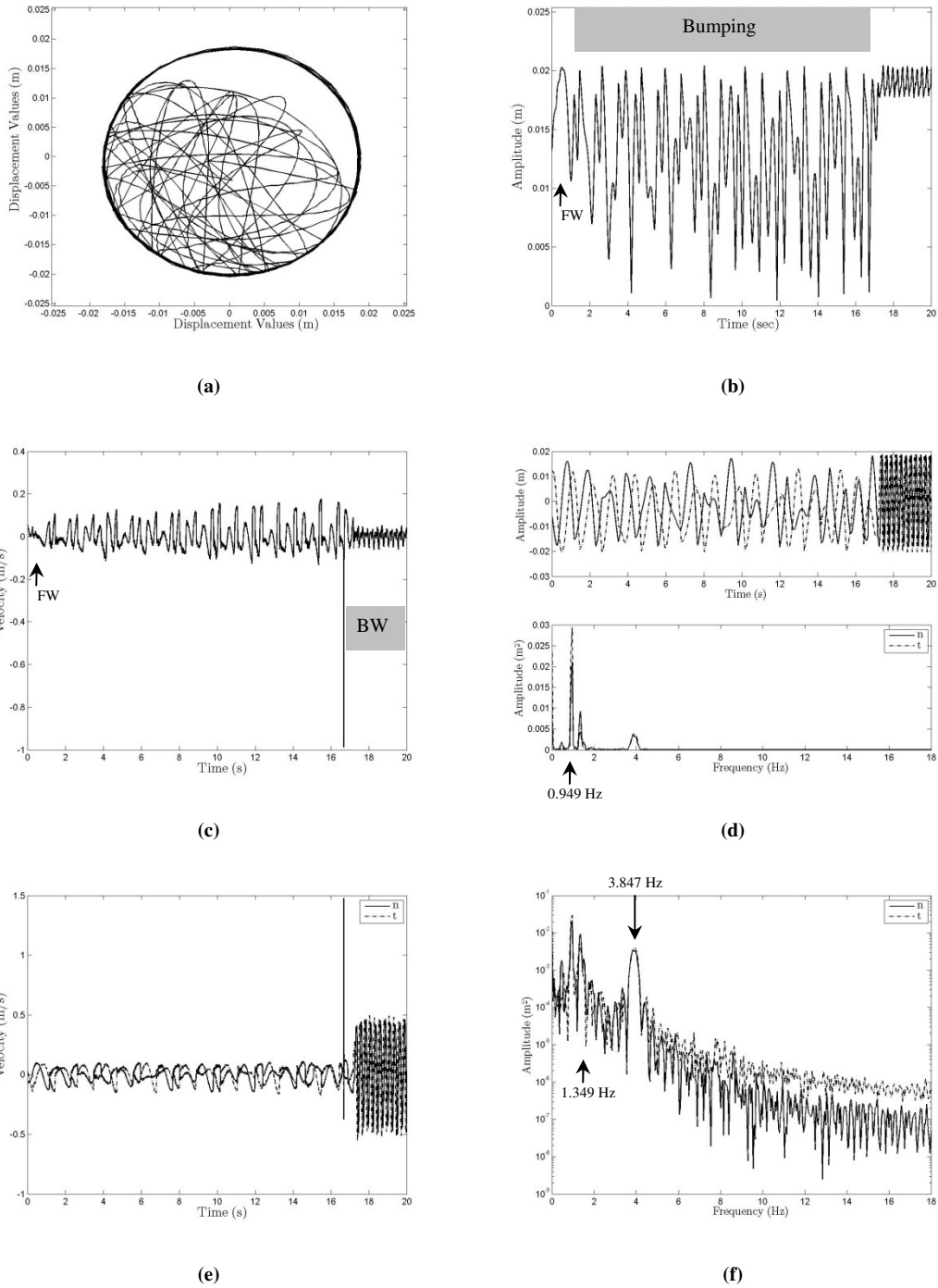


**Figure 2.14:** Rotor response for rotating speed of 55.6 rpm with rubber-rubber contact-Complete: (a) rotor trajectory, (b) radial displacement history, (c) time histories of normal and tangential speeds, (d) normal and tangential displacement histories (top) and

corresponding frequency spectra (bottom), (e) time histories of normal and tangential speeds, and (f) frequency spectra of normal and tangential displacement responses on log scale.

## **Chapter 3**

### **Modeling, Simulations, and Comparisons**

In this chapter, the work carried out on modeling and the corresponding numerical simulations undertaken to address the research objectives is discussed. Two reduced order models are derived and discussed in Section 3.1. The first model has four degree-of-freedom and the second model builds on the first and includes the tilt angle of the rotor as the fifth degree-of-freedom. As mentioned in introductory section, the four degree-of-freedom models closely follow the work of Melakhessou *et al.* (2003) and Jansen (1991), and through this dissertation work, a novel drill string and wellbore interaction model is introduced. Additionally, the five degree-of-freedom model considered in this chapter follows discussions with Professor M. Karkoub of the Texas T&M University, Doha, Qatar. In each of these models, a drill-string segment in the

BHA portion of Figure 1.1 is considered, and this segment is modeled as a rotor inside a shell. Equilibrium solutions of this system are explored in Section 3.2, and dynamics close to them are investigated through numerical simulations. In Section 3.3, the author has presented simulations carried out by using the nonlinear models to understand the drill-string dynamics, including bumping, sliding, and sticking motions. Furthermore, in Section 3.4, the results are compared with experimental findings and to the results obtained by Melakhessou *et al.* (2003).

### **3.1 Reduced-Order Models**

Reduced-order models are the low dimensional models that can be used to capture the dynamics of a continuous system. Reduced-order models can be developed for both linear and nonlinear systems (Antoulas, Sorensen, and Gugercin, 2001) and they have applications in wide range of research areas such as fluid dynamics (e.g., Bergmann, Cordier, and Brancher, 2005) and structural dynamics. One of the benefits of using reduced-order models of a nonlinear system is that one is able to obtain approximate solutions with limited computational resources.

#### **3.1.1 Model parameters**

In Table 3.1, the model variables and parameters used throughout the research are given.

The variable  $\rho$  is the radial or lateral displacement,  $\theta$  is the rotation of the first section,  $\varphi$  is the rotation due to the bending along the tangential direction, and  $\alpha$  is the rotation angle of the second section.

**Table 3.1: Symbols used for different quantities and their description**

Symbol	Meaning/Definition
$\rho$	Radial or Lateral Displacement of Rotor
$\theta$	Rotation Displacement of First Section (Stator)
$\varphi$	Rotation Displacement due to Bending
$\alpha$	Rotation Displacement of Second Section (Rotor)
$\psi$	Tilt Angle of Rotor
$I_1$	Stator Moment of Inertia
$I_2$	Rotor Moment of Inertia
$I_3$	Rotor Moment of Inertia in Tilting Direction
$m$	Mass of Second Section (Rotor)
$m_b$	Unbalanced Mass on Rotor
$K_r$	Stiffness along Radial Direction
$K_t$	Stiffness along Tangential Direction
$K_{tor}$	Torsion Stiffness
$K_p$	Stiffness of Outer Shell
$e$	Distance of Rotor Center to Unbalanced Mass
$\rho_0$	Initial Position of Rotor
$D$ & $D_{shell}$	Outer Shell Inner Diameter
$d$ & $d_{string}$	Rotor Diameter
$\tau$ & $M_{ext}$	External Torque
$\lambda$	Contact Parameter; equals to 1 when there is contact and 0 otherwise
$F_f$	Friction Force
$R$	Radius of Rotor
$l$	Length of String
$\delta$	$\delta = \rho_0 + gap$
$gap$	Radial Separation between Rotor and Outer shell at Initial Position

These four variables are used in the four degree-of-freedom model. In addition,  $m$  is the mass of second section, and  $m_b$  is the unbalanced mass located at a distance  $e$  from the axis of rotation of the second section. This distance quantity is also known as the eccentricity.

The second section is referred to as rotor, while the first section is referred to as stator in this research. The parameters  $I_1$ ,  $I_2$ , and  $I_3$  are moments of inertia of the stator, rotor, and rotor in tilting direction, respectively. Similarly,  $K_r$ ,  $K_t$ , and  $K_{tor}$  are the stiffness quantities along the radial, tangential, and torsion directions, respectively. The other stiffness quantity,  $K_p$ , is the stiffness of outer shell.

The five degree-of-freedom model includes the four variables used in the four degree-of-freedom model and the additional coordinate  $\psi$ , which represents the tilt angle of the rotor with respect to a vertical axis. These quantities are illustrated in Figures 3.1 and 3.2. Additional system quantities are shown in Table 3.1.

### **3.1.2 Four degree-of-freedom model**

Lateral vibrations occur in an operating drill string system, and are often times modeled by a rotor with an unbalanced mass (Jansen, 1991). Although the drill-string system is comprised of a combination of spatially continuous members and discrete elements, in an effort to understand the stick-slip interactions, reduced-order models have been

developed in this effort. A continuous drill string modeled as two discrete elements is illustrated in Figure 3.1(a). By monitoring the movement of each section, the dynamics of the drill string in the aforementioned section can be examined. Extending this idea, the whole dynamics of a drill string can be obtained by a series combination of such sections.

To develop these reduced-order models, building on the earlier efforts of Melakhessou *et al.* (2003), a section of the spatially continuous and rotating drill string is modeled as a system of two rotating sections with an unbalanced mass attached to one of them. These reduced-order models are meant to be a starting point for development of a full system model in the future.

As shown in Figure 3.1(b), the drill-string system is modeled as system with two rotating sections, a top stator and a bottom rotor. The bottom rotor has three degrees of freedom and the top stator has one degree of freedom to make a total of four degrees of freedom. The first section (stator) has one degree-of-freedom in rotation  $\theta$ . The second section (rotor) has three degrees of freedom, which are namely, the radial displacement  $\rho$ ,

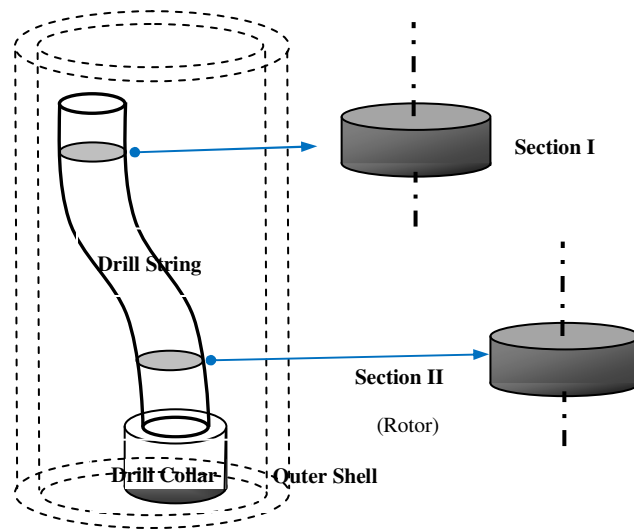


**Figure 3.1(a):** Illustration of two section model.

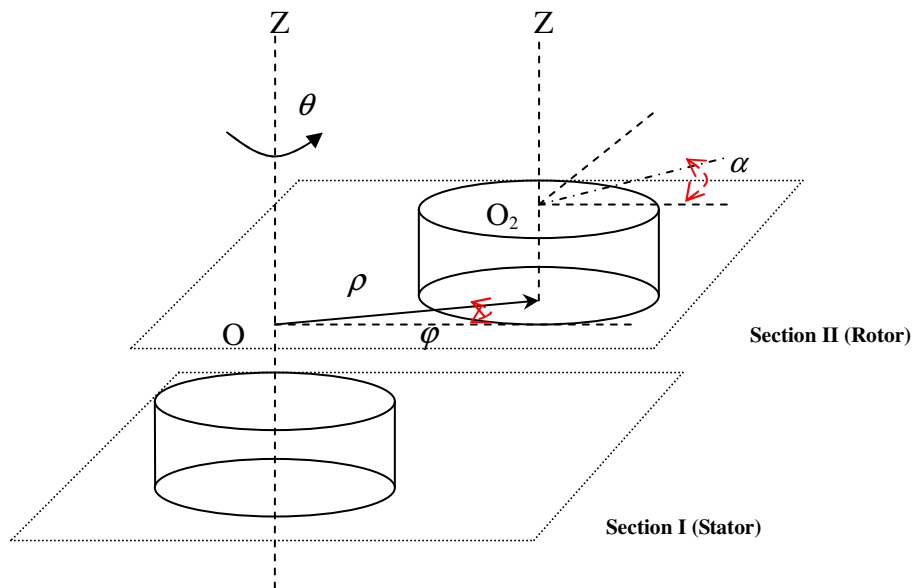


**Figure 3.1 (b):** Drill string modeled as a system with two sections.

the bending angle  $\varphi$  along the tangential direction, and the torsion angle  $\alpha$ . In addition,  $m_b$  is the unbalanced mass located at a distance  $e$  from the axis of rotation of the second section, as shown in Figure 3.2(a).



The parameters used in the development of the four degree-of-freedom model and the model illustrations are shown in Figure 3.2(b). A linear spring contact model is used to represent the interactions between the drill string and the outer shell or borehole.

### I. Energy and Virtual Work Expressions

For the continuous drill-string system shown in Figure 3.1(a), by accounting for the continuous and the discrete elements, the Lagrangian can be formed as [Liao *et al.*, 2009]

$$\begin{aligned}
 L_{system} &= L_{continuous\ element} + L_{discrete\ element\ I} + L_{discrete\ element\ II} \\
 &= \int_0^l \left( T_{continuous\ element} - V_{continuous\ element} \right) dz + T_{discrete\ element\ I} + T_{discrete\ element\ II} \\
 &\quad - V_{discrete\ element\ I} - V_{discrete\ element\ II}
 \end{aligned} \tag{3.1}$$

where  $L_{system}$  represents the system Lagrangian,  $T$  and  $V$  are the kinetic and potential energy components, respectively, and  $z$  is a parameter along the axial direction of the drill string of length  $l$ . Neglecting the inertia properties of the continuous element and taking into account only the stiffness properties of the continuous element and the unbalanced mass, the energy expressions for the reduced-order system are formed as given next.

Different than the equations shown in Appendix B for the model used by Melakhessou *et al.* (2003), the kinetic energy of reduced-order system can be constructed as shown in equations (3.2) and (3.3).

$$T_{total} \approx T_{discrete\ element\ I} + T_{discrete\ element\ II} \tag{3.2}$$

$$T_{total} = T = \frac{1}{2} I_1 \dot{\theta}^2 + \frac{1}{2} (m + m_b) (\dot{\rho}^2 + \rho^2 (\dot{\theta} + \dot{\varphi})^2) + \frac{1}{2} I_2 \dot{\alpha}^2 + \frac{1}{2} m_b e^2 \dot{\alpha}^2 + m_b e \dot{\alpha} [\rho (\dot{\theta} + \dot{\varphi}) \cos(\alpha - \theta - \varphi) - \dot{\rho} \sin(\alpha - \theta - \varphi)] \quad (3.3)$$

where the different inertia parameters are defined as in Table 3.1. The system potential energy can be constructed as

$$V_{total} = V_{continuous\ element} + V_{discrete\ element\ I} + V_{discrete\ element\ II} \approx U_{total} \quad (3.4)$$

$$U_{total} = \frac{1}{2} K_r (\rho - \rho_0)^2 + \frac{1}{2} K_t (\rho \varphi)^2 + \frac{1}{2} K_{tor} (\alpha - \theta)^2 + \frac{1}{2} \lambda K_p \left[ \rho - \frac{1}{2} (D - d) \right]^2 \quad (3.5)$$

where the different stiffness constants are as defined in Appendix B and  $\lambda$  is a contact parameter to be used to capture the contact between the rotor and outer shell. It is zero when there is no contact and one when there is contact. The virtual work associated with the external forces and moments is given by

$$\delta W_{ext} = -\lambda F_t [R(\delta\alpha) + \rho(\delta\theta + \delta\varphi)] + M_{ext} \delta\alpha \quad (3.6)$$

It is mentioned that the work done by the external moment differs from that provided in the work of Melakhessou *et al.* (2003).

## II. Four Degree-of-freedom Model of Melakhessou *et al.* (2003)

Melakhessou *et al.* (2003) obtained the following equations after assuming the level of unbalanced mass is much less than rotor mass  $m + m_b \approx m$ , neglecting the rotary inertia associated with the unbalanced mass  $m_b e^2$  and using  $M_{ext} \delta\theta$  for the external work

done by the moment instead of the  $M_{ext} \delta\alpha$  term shown in equation (3.6). These equations can be derived by using the extended Hamilton's principle (e.g., Meirovitch, 2001). Details of the derivation are shown in Appendix B.

$$m \ddot{\rho} - m \rho (\dot{\theta} + \dot{\varphi})^2 + K_r (\rho - \rho_0) + \lambda K_p (\rho - \delta) + K_t \rho \dot{\varphi}^2 = em_b (\dot{\alpha}^2 \cos(\beta) + \ddot{\alpha} \sin(\beta)) \quad (3.7)$$

$$I_1 \ddot{\theta} + m \rho^2 (\ddot{\theta} + \ddot{\varphi}) + 2m \rho \dot{\rho} (\dot{\theta} + \dot{\varphi}) = -em_b \ddot{\alpha} \rho \cos(\beta) + em_b \rho \dot{\alpha}^2 \sin(\beta) + \lambda F_t \rho + M_{ext} \quad (3.8)$$

$$m \rho (\ddot{\theta} + \ddot{\varphi}) + 2m \dot{\rho} (\dot{\theta} + \dot{\varphi}) + K_t \rho \dot{\varphi} = -em_b \ddot{\alpha} \cos(\beta) + em_b \dot{\alpha}^2 \sin(\beta) + \lambda F_t \quad (3.9)$$

$$I_2 \ddot{\alpha} + K_{tor} (\alpha - \theta) = -em_b ([2 \dot{\rho} (\dot{\theta} + \dot{\varphi}) + \rho (\ddot{\theta} + \ddot{\varphi})] \cos(\beta) + [\rho (\dot{\theta} + \dot{\varphi})^2 - \ddot{\rho}] \sin(\beta)) + \lambda F_t R \quad (3.10)$$

where

$$\beta = \alpha - (\theta + \varphi) \quad (3.11)$$

### III. Modified Four Degree-of-freedom Model of Dissertation Work

Starting from Lagrangian, Equations (3.3), (3.5) and (3.6) and using the extended

Hamilton's principle, the following governing equations of motion are obtained:

$$(m + m_b) \ddot{\rho} - (m + m_b) \rho (\dot{\theta} + \dot{\varphi})^2 + K_r (\rho - \rho_0) + \lambda K_p (\rho - \delta) + K_t \rho \dot{\varphi}^2 - em_b (\ddot{\alpha} \sin(\beta) + \dot{\alpha}^2 \cos(\beta)) = 0 \quad (3.12)$$

$$I_1 \ddot{\theta} + (m + m_b) \rho^2 (\ddot{\theta} + \ddot{\varphi}) + 2(m + m_b) \rho \dot{\rho} (\dot{\theta} + \dot{\varphi}) - K_{tor} (\alpha - \theta) - em_b \rho (\dot{\alpha}^2 \sin(\beta) - \ddot{\alpha} \cos(\beta)) = -\lambda F_t \rho \quad (3.13)$$

$$(m + m_b) \rho (\ddot{\theta} + \ddot{\varphi}) + 2(m + m_b) \dot{\rho} (\dot{\theta} + \dot{\varphi}) + K_t \rho \dot{\varphi} - em_b (\dot{\alpha}^2 \sin(\beta) - \ddot{\alpha} \cos(\beta)) = -\lambda F_t \quad (3.14)$$

$$(I_2 + m_b e^2) \ddot{\alpha} + K_{tor} (\alpha - \theta) + em_b [-\ddot{\rho} \sin(\beta) + \rho(\ddot{\theta} + \ddot{\varphi}) \cos(\beta) + \rho(\dot{\theta} + \dot{\varphi})^2 \sin(\beta) + 2\dot{\rho}(\dot{\theta} + \dot{\varphi}) \cos(\beta)] = M_{ext} - \lambda F_t R \quad (3.15)$$

Equations (3.12)-(3.15) can be assembled in the matrix form

$$[M]\{\ddot{X}\} + [C]\{\dot{X}\} + [K]\{X\} = \{F\} \quad (3.16)$$

where the  $[M]$ ,  $[C]$  and  $[K]$  matrices are discussed below, along with the displacement vector  $\{X\}$ .

$$\{X\} = \begin{Bmatrix} \rho \\ \theta \\ \varphi \\ \alpha \end{Bmatrix} \quad (3.17)$$

$$[M] = \begin{bmatrix} m + m_b & 0 & 0 & -em_b \sin(\beta) \\ 0 & I_1 + (m + m_b) \rho^2 & (m + m_b) \rho^2 & em_b \rho \cos(\beta) \\ 0 & (m + m_b) \rho & (m + m_b) \rho & em_b \cos(\beta) \\ -em_b \sin(\beta) & em_b \rho \cos(\beta) & em_b \rho \cos(\beta) & I_2 + m_b e^2 \end{bmatrix} \quad (3.18)$$

$$[C] = \begin{bmatrix} 0 & -(m + m_b) \rho(\dot{\theta} + \dot{\varphi}) & -(m + m_b) \rho(\dot{\theta} + \dot{\varphi}) & -em_b \dot{\alpha} \cos(\beta) \\ 0 & 2(m + m_b) \rho \dot{\rho} & 2(m + m_b) \rho \dot{\rho} & -em_b \rho \dot{\alpha} \sin(\beta) \\ 0 & 2(m + m_b) \dot{\rho} & 2(m + m_b) \dot{\rho} & -em_b \dot{\alpha} \sin(\beta) \\ 2em_b (\dot{\theta} + \dot{\varphi}) \cos(\beta) & em_b \rho(\dot{\theta} + \dot{\varphi}) \sin(\beta) & em_b \rho(\dot{\theta} + \dot{\varphi}) \sin(\beta) & 0 \end{bmatrix} \quad (3.19)$$

$$[K] = \begin{bmatrix} \lambda K_p + K_r & 0 & K_t \rho \varphi & 0 \\ \lambda F_t & K_{tor} & 0 & -K_{tor} \\ 0 & 0 & K_t \rho & 0 \\ 0 & -K_{tor} & 0 & K_{tor} \end{bmatrix} \quad (3.20)$$

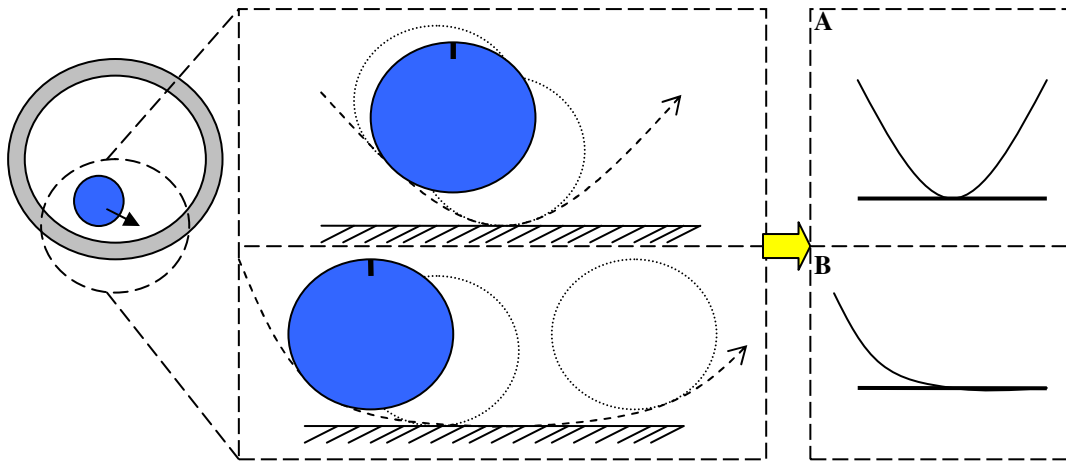
$$\text{and } [F] = \begin{bmatrix} \lambda K_p \delta + K_r \rho_0 \\ 0 \\ -\lambda F_t \\ M_{ext} - \lambda F_t R \end{bmatrix} \quad (3.21)$$

Equations (3.17) to (3.21) are recast in the state-space form to generate the numerical solutions of the nonlinear four degree-of-freedom system. It is noted that the equations of motion are nonlinearly coupled.

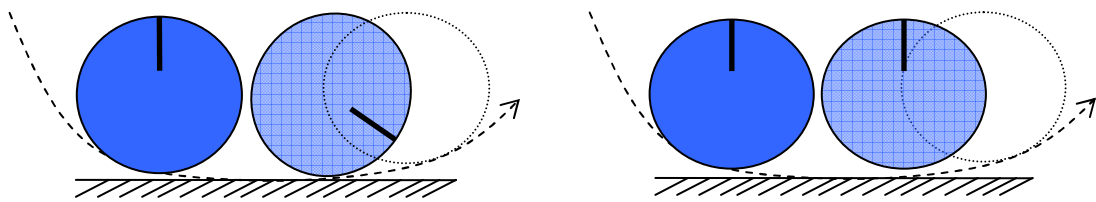
#### IV. Stick-Slip Interaction Model

The stick-slip interactions between the drill string and the outer shell are modeled along the lines of the work of Leine *et al.* (2002) and Leine and Nijmeijer (2004). The different cases considered here are as follows: i) no contact between the outer edge of the string and the shell (i.e.,  $\lambda = 0$  in this case) and the normal contact force  $F_{normal}$  is zero in this case, ii) there is contact and there is only rotation and no sliding as shown in Figure 3.3(b), and iii) there is contact and there is pure sliding and no rotation as shown in Figure 3.3(c). In the present work, the possibility for combined rolling and slipping is not included.

Equations (3.22) to (3.27) are used to determine and describe the contact between the drill string and the outer shell. The tangential force used in equations (3.12)-(3.15) or



(a)



(b)

(c)

**Figure 3.3:** Illustrations of two contact scenarios between drill string and outer shell.

equations (3.17)-(3.21) is determined from equation (3.25). The parameter  $\delta$  is the radial

separation between the outer shell and the drill string, and this parameter is used to judge

whether there is contact or not. The relative speed  $V_{relative}$  between the two contacting

surfaces is used to determine whether there is sliding or not. Equation (3.27) is

determined on the basis of a pure rolling mode. The maximum tangential force is

calculated as  $F_t|_{max}$ .

$$\delta = 0.5 \cdot (D - d) \tag{3.22}$$

$$\lambda = \begin{cases} 0; \rho \leq \delta \\ 1; \rho > \delta \end{cases} \quad (3.23)$$

$$F_{normal} = \begin{cases} 0 & \rho \leq \delta \\ K_p \cdot (\rho - \delta) & \rho > \delta \end{cases} \quad (3.24)$$

$$F_t = \begin{cases} F_t|_{equ}; & V_{relative} = 0 \text{ \& } |F_t|_{max} \geq |F_t|_{equ} \\ F_t|_{max}; & else \end{cases} \quad (3.25)$$

$$F_t|_{max} = -sign(V_{relative}) \cdot \mu \cdot F_{normal} \quad (3.26)$$

$$F_t|_{equ} = -\frac{M_{ext}}{\frac{2I_2}{m \cdot d} + 0.5 \cdot d} \quad (3.27)$$

### 3.1.3 Different form of four degree-of-freedom model

Making use of the extended Hamilton principle and starting from the system Lagrangian

again, the governing equations of the system in terms of Hamiltonian quantities are

obtained as shown below:

$$\begin{aligned} \dot{\rho} = & -\left[ e^2 m_b^2 \Pi_\varphi \sin(2\beta) \right] + \left\{ 2(m + m_b) \left[ e^2 m_b m + I_2 (m + m_b) \right] \right\}^{-1} \\ & \cdot \left\{ \left[ 2I_2 (m + m_b) + e^2 m_b (2m + m_b) \right] \Pi_\rho - e^2 m_b^2 \Pi_\rho \cos(2\beta) + 2em_b (m + m_b) \Pi_\alpha \sin(\beta) \right\} \end{aligned} \quad (3.28)$$

$$\begin{aligned} \dot{\Pi}_\rho = & \left\{ 2(m + m_b) \rho^3 \left[ e^2 m_b m + I_2 (m + m_b) \right] \right\}^{-1} \cdot \\ & \left\{ \begin{aligned} & \Pi_\varphi^2 \left[ 2I_2 (m + m_b) + e^2 m_b (2m + m_b) + e^2 m_b^2 \cos(2\beta) \right] \\ & - 2\rho em_b \Pi_\varphi \cos(\beta) \cdot \left[ (m + m_b) \Pi_\alpha + em_b \Pi_\rho \sin(\beta) \right] \\ & + 2(m + m_b) \cdot \rho^2 \left[ e^2 m_b m + I_2 (m + m_b) \right] \cdot \left[ \lambda K_p \delta + K_r \rho_0 - \rho (K_r + \lambda K_p + K_t \varphi^2) \right] \end{aligned} \right\} \end{aligned} \quad (3.29)$$

In equation (3.28),  $\dot{\rho}$  represents the first derivative of the lateral displacement and in

equation (3.29) and  $\dot{\Pi}_\rho$  represents the first derivative of the momentum associated with this degree-of-freedom. The rest of the equations of motion are given by

$$\dot{\theta} = (\Pi_\theta - \Pi_\varphi) / I_1 \quad (3.30)$$

$$\lambda F_t \rho + \dot{\Pi}_\theta = \left\{ 2(m + m_b) \rho^2 \left[ e^2 m_b m + I_2 (m + m_b) \right] \right\}^{-1} \cdot \left\{ \begin{aligned} & -e^2 m_b^2 \Pi_\varphi^2 \sin(2\beta) + 2em_b \Pi_\varphi \rho (-em_b \Pi_\rho \cos(2\beta) + (m + m_b) \Pi_\alpha \sin(\beta)) \\ & + 2em_b \Pi_\rho \cos(\beta) \cdot \left[ (m + m_b) \Pi_\alpha + em_b \Pi_\rho \sin(\beta) \right] \\ & + K_{tor} (\alpha - \theta) \cdot (m + m_b) \cdot \left[ e^2 m_b m + I_2 (m + m_b) \right] \rho^2 \end{aligned} \right\} \quad (3.31)$$

$$\left\{ I_1 (m + m_b) \rho \left[ e^2 m_b m + I_2 (m + m_b) \right] \right\}^{-1} \cdot \left\{ \begin{aligned} & -I_1 \Pi_\varphi \left[ 2I_2 (m + m_b) + e^2 m_b (2m + m_b) + e^2 m_b^2 \cos(2\beta) \right] \\ & + 2\rho em_b I_1 \cos(\beta) \cdot \left[ (m + m_b) \Pi_\alpha + em_b \Pi_\rho \sin(\beta) \right] \\ & + (m + m_b) \cdot \rho \left[ e^2 m_b m + I_2 (m + m_b) \right] \cdot (\Pi_\theta - \Pi_\varphi + I_1 \dot{\varphi}) \end{aligned} \right\} = 0 \quad (3.32)$$

$$e^2 m_b^2 \Pi_\varphi^2 \sin(2\beta) + 2 \left\{ (m + m_b) \left[ e^2 m_b m + I_2 (m + m_b) \right] \right\}^{-1} \cdot \left\{ \begin{aligned} & em_b \Pi_\varphi \left[ em_b \Pi_\rho \cos(2\beta) - (m + m_b) \Pi_\alpha \sin(\beta) \right] \\ & - \rho em_b \Pi_\rho \cos(\beta) \cdot \left[ (m + m_b) \Pi_\alpha + em_b \Pi_\rho \sin(\beta) \right] \\ & + \rho (m + m_b) \cdot \left[ e^2 m_b m + I_2 (m + m_b) \right] \cdot (\lambda F_t \rho + K_t \varphi \rho^2 + \dot{\Pi}_\varphi) \end{aligned} \right\} = 0 \quad (3.33)$$

$$\dot{\alpha} = \left\{ 4I_1 (m + m_b) \rho \left[ e^2 m_b m + I_2 (m + m_b) \right] \right\}^{-1} \cdot \left\{ -4em_b I_1 (m + m_b) \Pi_\varphi \cos(\beta) + \rho \left[ 4I_1 (m + m_b)^2 \Pi_\alpha + 4em_b I_1 (m + m_b) \Pi_\rho \sin(\beta) \right] \right\} \quad (3.34)$$

$$\lambda F_t R + \dot{\Pi}_\alpha = M_{ext} + \left\{ 2(m + m_b) \rho^2 \left[ e^2 m_b m + I_2 (m + m_b) \right] \right\}^{-1} \cdot \left\{ \begin{aligned} & e^2 m_b^2 \Pi_\varphi^2 \sin(2\beta) + 2em_b \Pi_\varphi \rho \left[ em_b \Pi_\rho \cos(2\beta) - (m + m_b) \Pi_\alpha \sin(\beta) \right] \\ & - 2\rho^2 em_b \Pi_\rho \cos(\beta) \cdot \left[ (m + m_b) \Pi_\alpha + em_b \Pi_\rho \sin(\beta) \right] \\ & - 2\rho^2 K_{tor} (m + m_b) \cdot (\alpha - \theta) \cdot \left[ e^2 m_b m + I_2 (m + m_b) \right] \end{aligned} \right\} \quad (3.35)$$

Equations (3.28)-(3.35) describe the time evolutions of the different displacements

and the associated momenta for the top and bottom discs. This model obtained in terms of the Hamiltonian quantities is the other form of the four degree-of-freedom model. Both of these two forms are used to generate numerical results.

### **3.1.4 Five degree-of-freedom model**

In addition to the four coordinates that have been used in the four degree-of-freedom model, namely, the radial displacement  $\rho$ , the rotation  $\theta$  of first section or stator, the bending angle  $\varphi$  along the tangential direction, the torsion angle  $\alpha$  of the second section or rotor, an additional coordinate, the tilt angle  $\psi$  of the rotor, is introduced.

The derivation of the five degree-of-freedom model is also carried out by using the Extended Hamilton's Principle. To this end, as carried out in Appendix B for the four degree-of-freedom case, the system kinetic energy, system potential energy, and virtual work are first constructed next.

#### **I. System Kinetic Energy**

Again, the total kinetic energy is composed of the energy of each section and the kinetic energy of the unbalanced mass.

##### **1. Kinetic Energy of Stator**

The motion of stator is a rotation around axis OZ with an angular speed  $\dot{\theta}$ ; thus, the energy is

$$T_1 = \frac{1}{2} I_1 \dot{\theta}^2 \quad (3.36)$$

where  $I_1$  is the mass moment of inertia of stator. The whole system rotates with an angular speed  $\dot{\theta}$ .

## 2. Kinetic Energy of Rotor

The rotor has a mass  $m$  and mass moments of inertia  $I_2$  and  $I_3$  about the axes of interest. This rotor's center of mass has a radial motion  $\rho$  with respect to axis  $OZ$  and angular speed components  $\dot{\alpha}$  and  $\dot{\psi}$  about the respective axes of interest. Hence, the kinetic energy can be written as

$$T_2 = \frac{1}{2} m (\mathbf{V}_G \cdot \mathbf{V}_G) + \frac{1}{2} I_2 \dot{\alpha}^2 + \frac{1}{2} I_3 \dot{\psi}^2 \quad (3.37)$$

where the velocity of the center of mass  $\mathbf{V}_G$  is

$$\mathbf{V}_G = \dot{\rho} \hat{n} + \rho (\dot{\theta} + \dot{\varphi}) \hat{t} \quad (3.38)$$

## 3. Kinetic Energy of the Unbalanced Mass

The different components of the position vector from the unbalanced mass  $m_b$  to the origin  $O$  in Figure 3.4(a), and the rotation matrix  $[L]$  for the tilt angle about the  $\hat{i}$  direction can be determined as

$$\begin{cases} \mathbf{OM}_b \cdot \hat{i} \\ \mathbf{OM}_b \cdot \hat{j} \\ \mathbf{OM}_b \cdot \hat{k} \end{cases} = \begin{cases} \rho \cos(\theta + \varphi) + e \cos(\alpha) \\ \rho \sin(\theta + \varphi) + e \sin(\alpha) \\ 0 \end{cases} \quad \text{and} \quad [L] = \begin{bmatrix} 1 & 0 & 0 \\ 0 & \cos(\psi) & \sin(\psi) \\ 0 & -\sin(\psi) & \cos(\psi) \end{bmatrix} \quad (3.39a)$$

Thus, the components of the position vector to the unbalanced mass are transformed

to

$$\begin{Bmatrix} \mathbf{OM}_b \bullet \hat{\mathbf{i}}' \\ \mathbf{OM}_b \bullet \hat{\mathbf{j}}' \\ \mathbf{OM}_b \bullet \hat{\mathbf{k}}' \end{Bmatrix} = [L] \begin{Bmatrix} \mathbf{OM}_b \bullet \hat{\mathbf{i}} \\ \mathbf{OM}_b \bullet \hat{\mathbf{j}} \\ \mathbf{OM}_b \bullet \hat{\mathbf{k}} \end{Bmatrix} = \begin{bmatrix} 1 & 0 & 0 \\ 0 & \cos(\psi) & \sin(\psi) \\ 0 & -\sin(\psi) & \cos(\psi) \end{bmatrix} \begin{bmatrix} \rho \cos(\theta + \varphi) + e \cos(\alpha) \\ \rho \sin(\theta + \varphi) + e \sin(\alpha) \\ 0 \end{bmatrix} \quad (3.39b)$$

where the unit vectors with the primes are along the corresponding rotated directions.

The kinetic energy of the unbalanced mass is given by

$$\begin{aligned} T_b = \frac{1}{2} m_b \left( \frac{d(\mathbf{OM}_b)}{dt} \bullet \frac{d(\mathbf{OM}_b)}{dt} \right) &= \frac{1}{2} m_b (e^2 \dot{\alpha}^2 + \dot{\rho}^2 + \rho^2 (\dot{\theta} + \dot{\varphi})^2 \\ &+ 2e \dot{\alpha} [\rho (\dot{\theta} + \dot{\varphi}) \cos(\beta) - \dot{\rho} \sin(\beta)] \\ &+ \rho^2 \dot{\psi}^2 \sin^2(\theta + \varphi) + \rho^2 \dot{\psi}^2 \sin^2(\alpha) \\ &+ 2e \rho \dot{\psi} \sin(\theta + \varphi) \sin(\alpha)) \end{aligned} \quad (3.40)$$

#### 4. Ratio of Unbalanced Mass to Mass of Rotor

In the work of Melakhessou *et al.* (2003), the unbalanced mass  $m_b$  is assumed to be relatively small compared to that of the mass of rotor, when the total system kinetic energy is constructed. However, here, the effect of unbalanced mass is considered.

Hence, the mass term is shown as  $m + m_b = m_t$ , while calculating the system kinetic energy.

#### 5. System Kinetic Energy

$$\begin{aligned}
 T = T_1 + T_2 + T_b = & \frac{1}{2} I_1 \dot{\theta}^2 + \frac{1}{2} m_t (\dot{\rho}^2 + \rho^2 (\dot{\theta} + \dot{\varphi})^2) + \frac{1}{2} (I_2 + m_b e^2) \dot{\alpha}^2 + \frac{1}{2} I_3 \dot{\psi}^2 \\
 & + \frac{1}{2} m_b (e^2 \dot{\alpha}^2 + \dot{\rho}^2 + \rho^2 (\dot{\theta} + \dot{\varphi})^2 + 2e \dot{\alpha} [\rho (\dot{\theta} + \dot{\varphi}) \cos(\beta) - \dot{\rho} \sin(\beta)]) \\
 & + \rho^2 \dot{\psi}^2 \sin^2(\theta + \varphi) + \rho^2 \dot{\psi}^2 \sin^2(\alpha) + 2e \rho \dot{\psi} \sin(\theta + \varphi) \sin(\alpha)
 \end{aligned} \tag{3.41}$$

## II. System Potential Energy

Proceeding along the lines of Appendix B, the system potential energy can be shown to be made up of the energy due to bending along radial and tangential directions and that due to contact deformation. This leads to

$$U_{total} = \frac{1}{2} K_r (\rho - \rho_0)^2 + \frac{1}{2} K_t (\rho \varphi)^2 + \frac{1}{2} K_{tor} (\alpha - \theta)^2 + \frac{1}{2} \lambda K_p (\rho - \delta)^2 \tag{3.42}$$

## III. Virtual Work

The external work done by the friction force  $F_t$  that acts along the tangential direction and the torque  $M_{ext}$  applied to Section II is determined as

$$\delta W_{ext} = -\lambda F_t [R(\delta\alpha + \delta\psi) + \rho(\delta\theta + \delta\varphi + \delta\psi)] + M_{ext} \delta\alpha \tag{3.43}$$

where  $\delta\alpha$ ,  $\delta\theta$ ,  $\delta\varphi$ , and  $\delta\alpha$  are the needed virtual displacements.

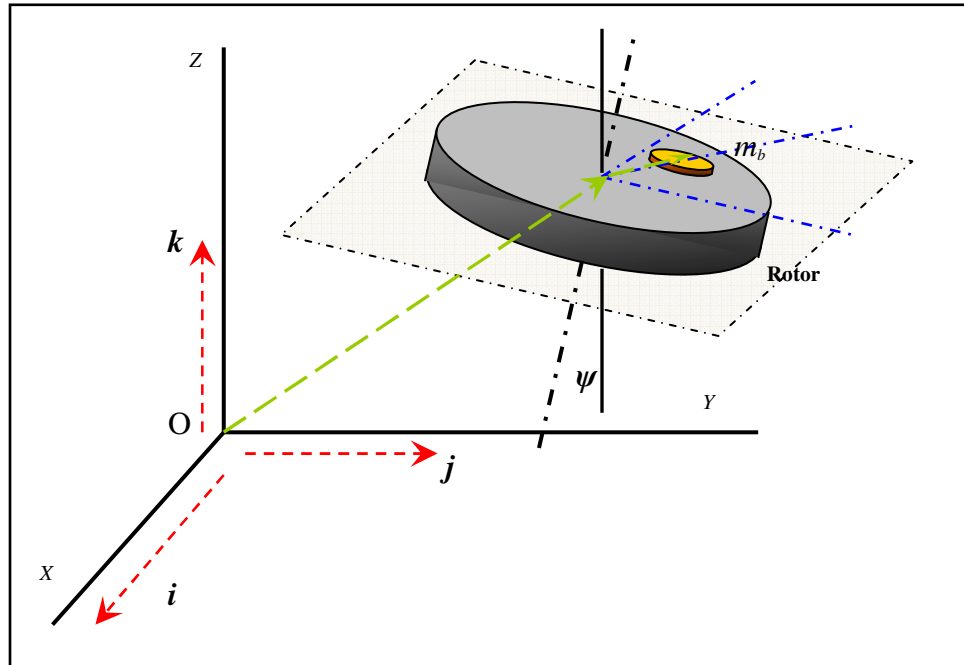


**Figure 3.4 (a):** Illustration for unbalanced mass in model with five degrees of freedom.

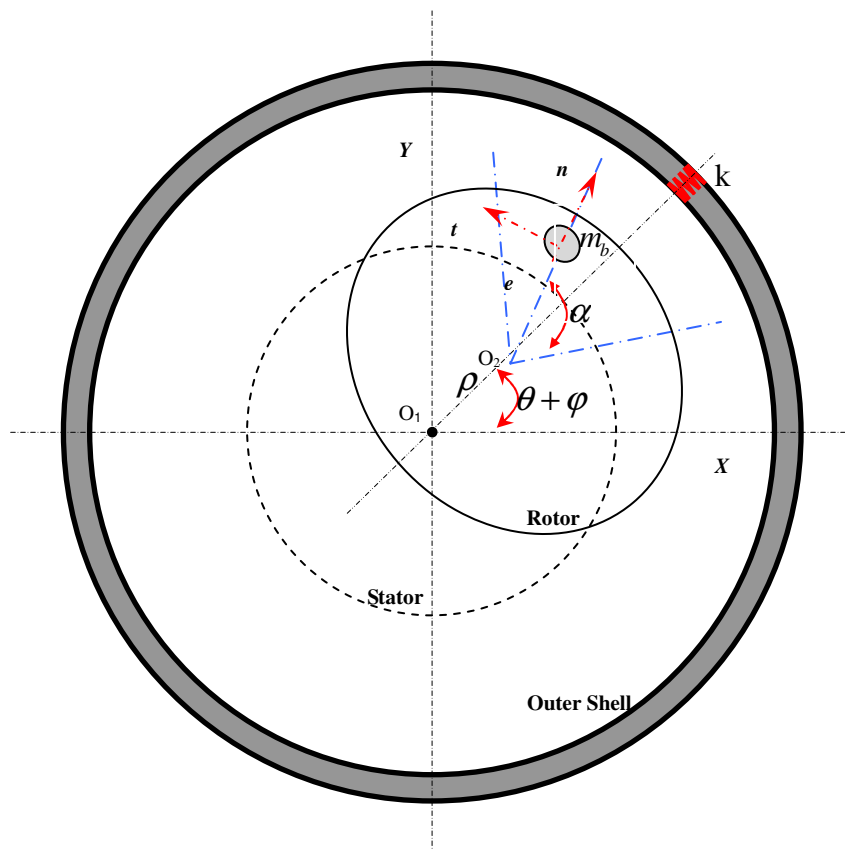


**Figure 3.4 (b):** Schematic of model with five degrees of freedom.

#### IV. Equations of Motion

In Figure 3.4 (b), a schematic of the five degree-of-freedom model is illustrated. Making use of equations (3.41)-(3.43) and the extended Hamilton's principle, the following equations of motion have been obtained:

$$(m + m_b) \ddot{\rho} - (m + m_b) \rho (\dot{\theta} + \dot{\varphi})^2 + K_r (\rho - \rho_0) + \lambda K_p (\rho - \delta) + K_t \rho \dot{\varphi}^2 \quad (3.44)$$

$$-m_b \rho \sin^2 (\theta + \varphi) \dot{\psi}^2 - m_b e \cos \beta \dot{\alpha}^2 - m_b e \sin \alpha \sin (\theta + \varphi) \dot{\psi} - m_b e \sin \beta \ddot{\alpha} = 0$$

$$I_1 \ddot{\theta} + (m + m_b) \rho^2 (\ddot{\theta} + \ddot{\varphi}) + 2(m + m_b) \rho \dot{\rho} (\dot{\theta} + \dot{\varphi}) - K_{tor} (\alpha - \theta) \quad (3.45)$$

$$-em_b \rho [\dot{\alpha}^2 \sin(\beta) - \ddot{\alpha} \cos(\beta)] - m_b \rho \dot{\psi}^2 \cos(\theta + \varphi) [e \sin \alpha + \rho \sin(\theta + \varphi)] = -\lambda F_t \rho$$

$$(m + m_b) \rho (\ddot{\theta} + \ddot{\varphi}) + 2(m + m_b) \dot{\rho} (\dot{\theta} + \dot{\varphi}) + K_t \rho \dot{\varphi} - em_b (\dot{\alpha}^2 \sin(\beta) - \ddot{\alpha} \cos(\beta)) \quad (3.46)$$

$$-m_b \dot{\psi}^2 \cos(\theta + \varphi) [e \sin \alpha + \rho \sin(\theta + \varphi)] = -\lambda F_t$$

$$(I_2 + m_b e^2) \ddot{\alpha} + K_{tor} (\alpha - \theta) + em_b [-\dot{\rho} \sin(\beta) + \rho (\ddot{\theta} + \ddot{\varphi}) \cos(\beta) + \rho (\dot{\theta} + \dot{\varphi})^2 \sin(\beta) \quad (3.47)$$

$$+ 2 \dot{\rho} (\dot{\theta} + \dot{\varphi}) \cos(\beta)] - em_b \dot{\psi}^2 \cos \alpha [e \sin \alpha + \rho \sin(\theta + \varphi)] = M_{ext} - \lambda F_t R$$

$$\{(I_3 + m_b e^2 \sin^2 \alpha) + \rho m_b \sin(\theta + \varphi) \cdot [2e \sin \alpha + \rho \sin(\theta + \varphi)]\} \ddot{\psi}$$

$$+ \{ [2m_b e \dot{\alpha} \cos \alpha + 2m_b \sin(\theta + \varphi) \dot{\rho} + 2m_b \cos(\theta + \varphi) \rho (\dot{\theta} + \dot{\varphi})] \quad (3.48)$$

$$\cdot [e \sin \alpha + \rho \sin(\theta + \varphi)] \} \dot{\psi} = -\lambda F_t (R + \rho)$$

The nonlinear equations of motion (3.44)-(3.48) are used to generate the numerical solutions for the five degree-of-freedom system discussed in later section. The contact between the drill string and the outer shell is modeled in the same manner as discussed earlier for the four degree-of-freedom case.

## 3.2 Analytical Investigations

In the last section, the drill string system has been modeled by using two models, one with four degrees of freedom and another with five degrees of freedom. Further, two different representations of the system, with one in terms of Hamiltonian quantities, were introduced. In this section, these models are studied.

### 3.2.1 Equilibrium solutions

Disregarding all the external force terms, the system is determined to have one fixed or equilibrium point. For the four degree-of-freedom model given by equations (3.7) - (3.10), the equilibrium solutions are obtained as

$$K_r(\rho - \rho_0) + \lambda K_p(\rho - \delta) + K_t \rho \varphi^2 = 0 \quad (3.49)$$

$$\lambda F_t \rho + M_{ext} = 0 \quad (3.50)$$

$$K_t \rho \varphi = \lambda F_t \quad (3.51)$$

$$K_{tor}(\alpha - \theta) = \lambda F_t R \quad (3.52)$$

Equations (3.49)-(3.52) lead to

$$\rho = \frac{K_r \rho_0 + \lambda K_p \delta}{K_r + \lambda K_p} \quad (3.53)$$

$$\theta = \alpha; \quad \varphi = 0 \quad (3.54)$$

The radial position of the equilibrium point depends on the initial radial displacement and the radial stiffness and contact stiffness. Also, this point can be

determined for either  $\lambda=0$  or  $\lambda=1$ , the particular value depending on the presence of contact between the rotor and the borehole (outer shell).

Similarly, for calculating the equilibrium points of the four degree-of-freedom model expressed in terms of the Hamiltonian quantities, equations (3.28)-(3.35) are used to generate the following equilibrium equations:

$$\dot{\theta} = 0 \quad (3.55)$$

$$\lambda F_t \rho = \left\{ 2(m + m_b) \rho^2 \left[ e^2 m_b m + I_2 (m + m_b) \right] \right\}^{-1} \cdot \left\{ K_{tor} (\alpha - \theta) \cdot (m + m_b) \cdot \left[ e^2 m_b m + I_2 (m + m_b) \right] \rho^2 \right\} \quad (3.56)$$

$$\left\{ I_1 (m + m_b) \rho \left[ e^2 m_b m + I_2 (m + m_b) \right] \right\}^{-1} \cdot \left\{ (m + m_b) \cdot \rho \left[ e^2 m_b m + I_2 (m + m_b) \right] \cdot I_1 \dot{\phi} \right\} = 0 \quad (3.57)$$

$$2 \left\{ (m + m_b) \left[ e^2 m_b m + I_2 (m + m_b) \right] \right\}^{-1} \cdot \left\{ \rho (m + m_b) \cdot \left[ e^2 m_b m + I_2 (m + m_b) \right] \cdot (\lambda F_t \rho + K_t \phi \rho^2) \right\} = 0 \quad (3.58)$$

$$\dot{\alpha} = 0 \quad (3.59)$$

$$\lambda F_t R = M_{ext} + \left\{ 2(m + m_b) \rho^2 \left[ e^2 m_b m + I_2 (m + m_b) \right] \right\}^{-1} \cdot \left\{ 2 \rho^2 K_{tor} (m + m_b) \cdot (\alpha - \theta) \cdot \left[ e^2 m_b m + I_2 (m + m_b) \right] \right\} \quad (3.60)$$

Equations (3.55-3.60) lead to

$$\rho = \frac{\lambda K_p \delta + K_r \rho_0}{K_r + \lambda K_p + K_t \phi^2} \quad (3.61)$$

$$\alpha - \theta = \frac{2 \lambda F_t \rho}{K_{tor}} \quad (3.62)$$

$$\phi = -\frac{\lambda F_t}{K_t \rho} \quad (\text{if } \rho \neq 0) \quad (3.63)$$

$$\alpha - \theta = \frac{M_{ext} - \lambda F_t R}{K_{tor}} \quad (3.64)$$

By comparing the equilibrium solutions obtained for the four degree-of-freedom models in the non-contact case (i.e.,  $\lambda=0$ ); that is equations (3.53)-(3.54) and equations (3.61)-(3.64), the condition

$$\rho = \rho_0; \quad \theta = \alpha; \quad \varphi=0 \quad (3.65)$$

can be obtained. From this, it is gathered, that in the absence of contact, the equilibrium depends on the initial position of the rotor in radial direction and external torque applied to the system. At equilibrium, the rotor's radial position is constant and the system experiences rigid body rotation if  $M_{ext}$  is a constant.

The equilibrium solution of the five degree-of-freedom model can be determined as

$$\rho = \frac{K_r \rho_0 + \lambda K_p \delta}{K_r + \lambda K_p}; \quad \theta = \alpha; \quad \varphi=0; \quad \psi=\text{constant} \quad (3.66)$$

As expected, there is no difference between the equilibrium solutions obtained for the five degree-of-freedom and four degree-of-freedom cases. The tilt angle between vertical axis and rotor  $\psi$  has no effect on the equilibrium position, if the tilt angle remains constant.

### 3.2.2 System performance around equilibrium

To study the model performance around the equilibrium position, numerical integrations were carried out for the parameter values used in earlier work. For the system

parameter values given in Table 3.2, the eigenvalues associated with the equilibrium position were determined from the corresponding Jacobian Matrix to be the following:

i.) For the non-contact case ( $\lambda=0$ ), eigenvalues are

$$\{0 \pm 114.018i, -1.24 \times 10^{-5} \pm 38.33i, -1.64 \times 10^{-5} \pm 33.35i, -8.34 \times 10^{-6}, -1.36 \times 10^{-9}\}$$

ii.) For the contact case ( $\lambda=1$ ), eigenvalues are

$$\{0 \pm 114.018i, -1.11 \times 10^{-4} \pm 38.33i, -1.51 \times 10^{-3} \pm 33.58i, 0, -7.66 \times 10^{-5}\}$$

For these parameter values, the equilibrium point of the four degree-of-freedom system is found to be unstable for both the contact and non-contact cases.

**Table 3.2: System parameter values used for studies (Melakhessou *et al.*, 2003)**

Parameters	Variable	Value	units
Mass of Rotor	$m$	$7.8 * 10^{-2}$	Kg
Unbalanced Mass on Rotor	$m_b$	$7.8 * 10^{-3}$	Kg
Stator Moment of Inertia	$I_1$	$9.34 * 10^{-4}$	$Kgm^2$
Rotor Moment of Inertia	$I_2$	$1.36 * 10^{-6}$	$Kgm^2$
Bending Stiffnesses I	$K_r$	$1.019 * 10^2$	$Nm^{-1}$
Bending Stiffnesses II	$K_t$	$1 * 10^2$	$Nm^{-1}$
Torsional Stiffnesses	$K_{TOR}$	1.371	$Nm^*rad^{-1}$
Stiffnesses of Outer Shell	$K_p$	$2 * 10^6$	$Nm^{-1}$
Outer Shell Inner Diameter	$D$	$2.4 * 10^{-2}$	m
Rotor Diameter	$d$	$2 * 10^{-2}$	m
Initial Position of Rotor	$\rho_0$	$1.9 * 10^{-3}$	m
Motor Torque	$\tau$	$4.05 * 10^{-3}$	Nm

Next, the motions of the four degree-of-freedom (DOF) and five degree-of-freedom systems around the equilibrium position are shown in Figures 3.5 and 3.6 for different initial conditions.

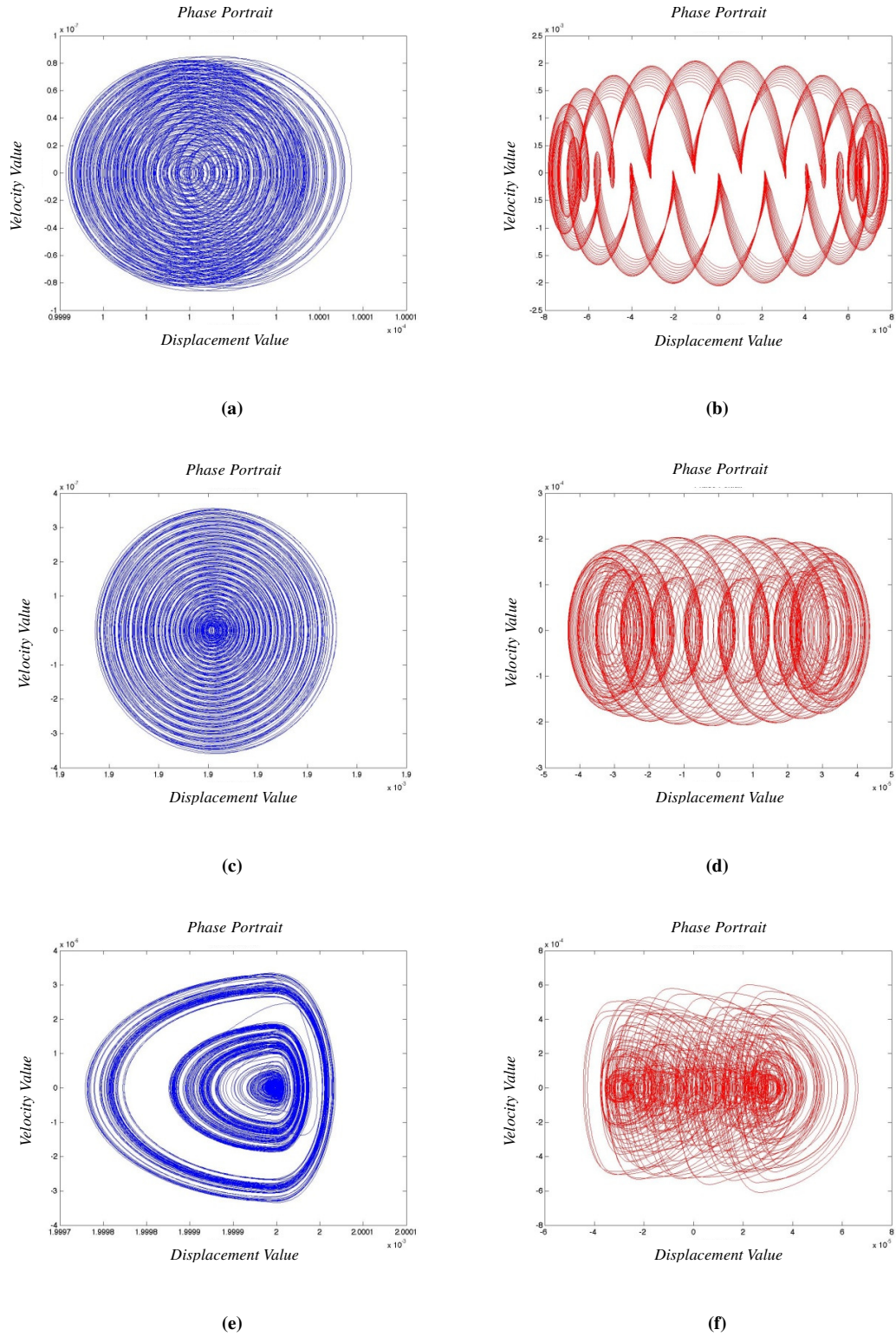
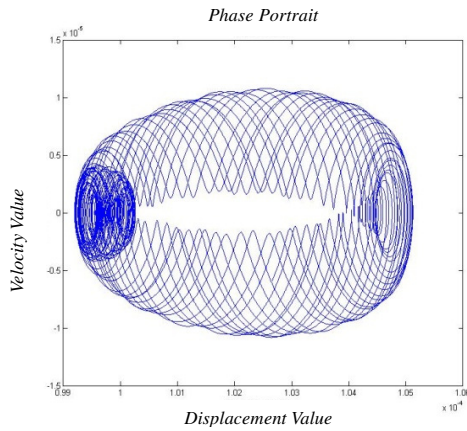
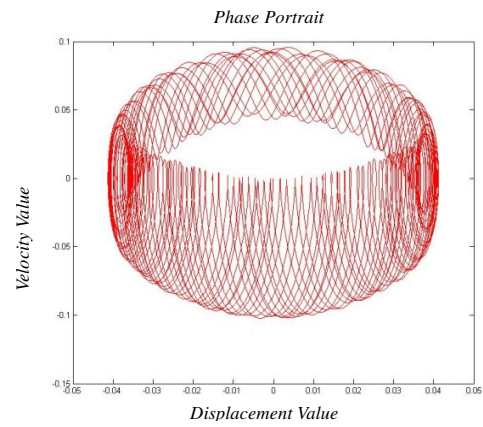


**Figure 3.5:** Phase portrait projections for motions around equilibrium point of four

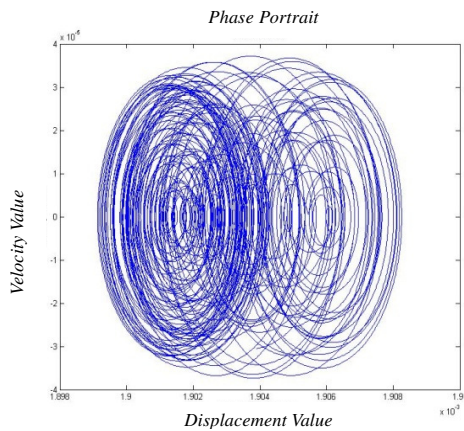
degree-of-freedom model: (a) lateral direction: initial position close to the origin, (b) lateral direction: initial position close to the outer shell (boundary), (c) lateral direction: initial position on the boundary, (d) tangential direction: initial position close to the origin, (e) tangential direction: initial position close to the boundary, and (f) tangential direction: initial position on the boundary.



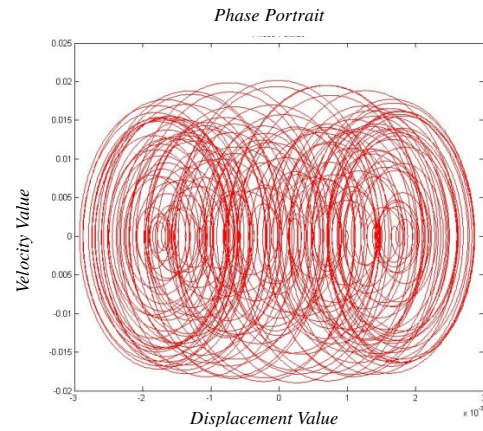
(a)



(b)



(c)



(d)

**Figure 3.6:** Phase portrait projections for motions around equilibrium point of five

degree-of-freedom model: (a) lateral direction: initial position close to the origin, (b) tangential direction: initial position close to the origin, (c) lateral direction: initial position close to the outer shell (boundary), and (d) tangential direction: initial position close to the boundary.

The results of Figure 3.5 and 3.6 illustrate that the characteristics of the motion are different when the motion is initiated close to center of the shell as opposed close to it or from the outer shell. These differences are primarily due to the contact between the outer shell and the rotor, which is discussed in the later sections. The inclusion of the tilt angle does include some oscillatory characteristics that were not previously observed.

### **3.3 Numerical Investigations**

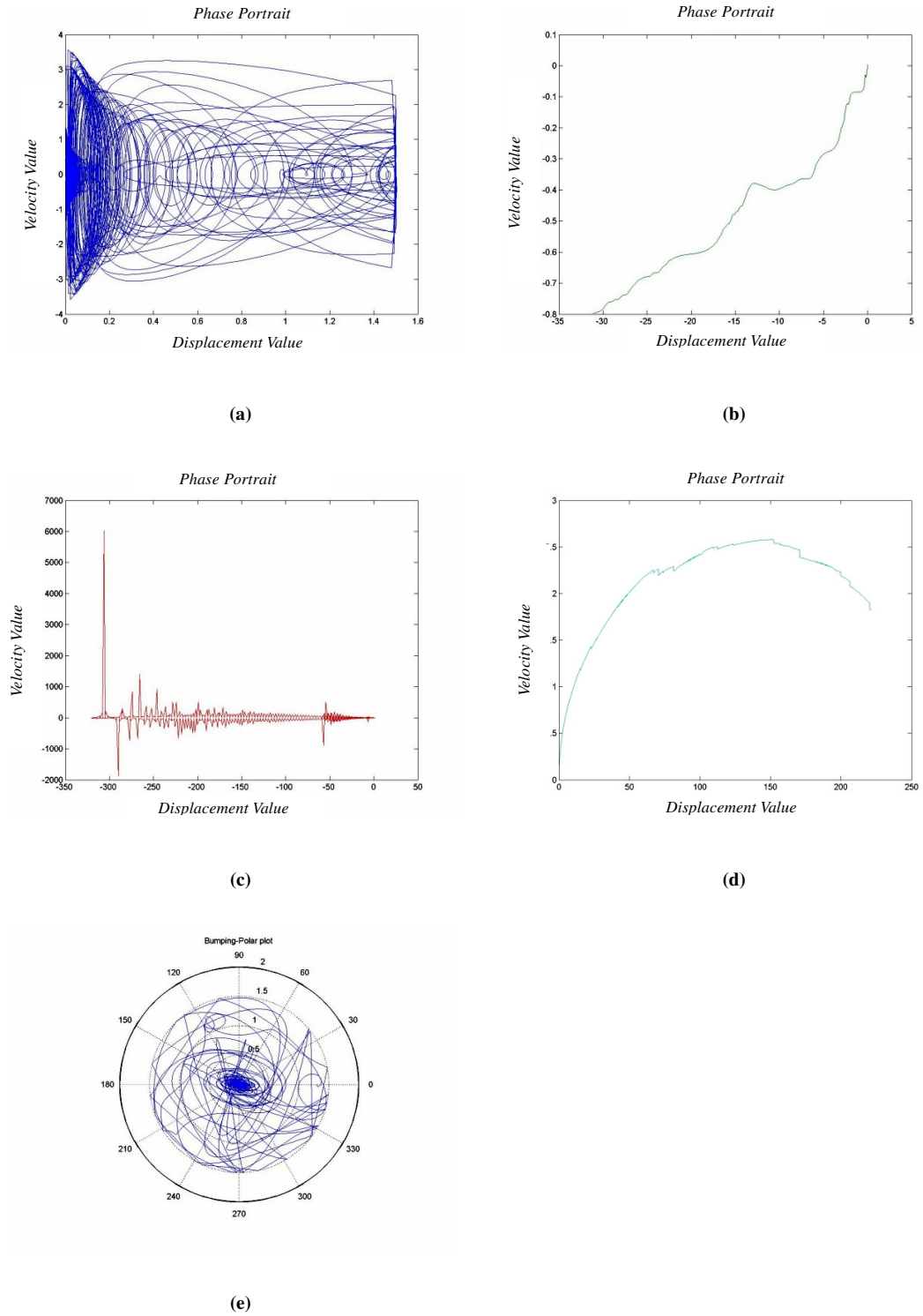
In order to better understand the system dynamics, numerical solutions of the governing equations obtained through numerical integrations turns out to be quite useful. In this section, a fourth order Runge-Kutta scheme is used for generating the numerical results with Matlab. Most of parameter values used are based on the work of Melakhessou *et al.* (2003), and other values that are not provided in this reference work are assumed; for example, the level of unbalanced mass  $m_b$ . Here, the ratio of unbalanced mass  $m_b$  to rotor mass  $m$  is taken as 0.1.

Parameter values provided in Table 3.2 were used to conduct simulations with equations (3.12)-(3.15) to provide a flavor for the qualitative aspects of the drill-string dynamics. Representative results obtained for two different values of the coefficient of friction  $\mu$  are shown in Figures 3.7 and 3.8. The contact friction coefficient  $\mu$  is set to 0.1 for “smooth” contact and 0.9 for “rough” contact. The initial position  $\rho_0$  of the string is close to the outer shell in both cases. It is noted that the stiffness of the outer shell is assumed to be orders of magnitude larger than that of the drill string itself. The contact between the rotor and outer shell is not considered as free-body contact.

The parameter values used to conduct the simulations with the five degree-of-freedom model given by equations (3.44)-(3.48) are as the same as that used for the four degree-of-freedom model provided in Table 3.2. Representative results obtained for two different values of the coefficient of friction  $\mu$  are shown in Figures 3.9 and Figures 3.10. As with the four degree-of-freedom model, the initial position of the string is close to the outer shell in both cases and the stiffness of the outer shell is assumed to be orders of magnitude larger than that of the drill string itself.

### **3.3.1 Numerical results for system with four degree-of-freedom**

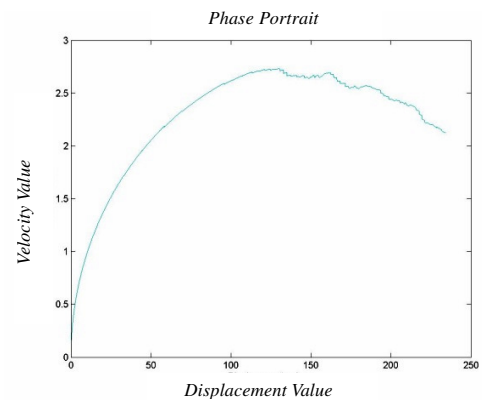
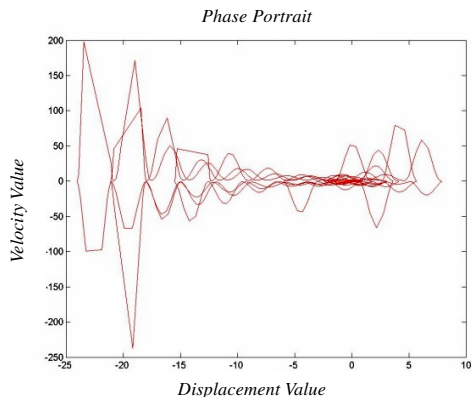
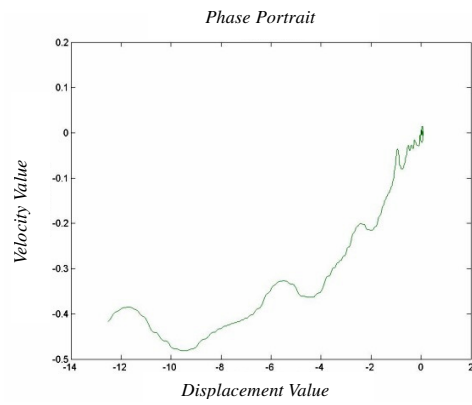
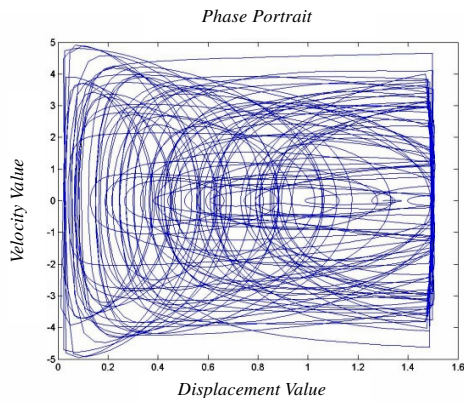
#### **Case I: High friction coefficient case, $\mu = 0.9$**

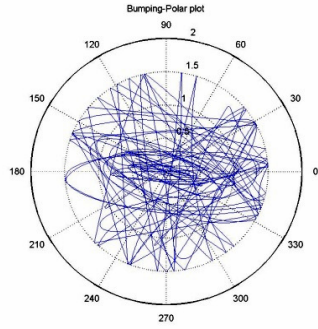


**Figure 3.7:** Four degree-of-freedom system responses for  $\mu=0.9$ : (a) radial displacement of rotor versus radial speed, (b) rotation angle of stator versus rate of change of rotation

angle, (c) bending angle of rotor versus rate of change of bending angle, (d) rotation angle of rotor versus rate of change of rotation angle, and (e) trajectory of the center of rotor in horizontal plane, in polar coordinates ( $\rho$ ,  $\theta$ ).

**Case II: Low friction coefficient case,  $\mu = 0.1$**



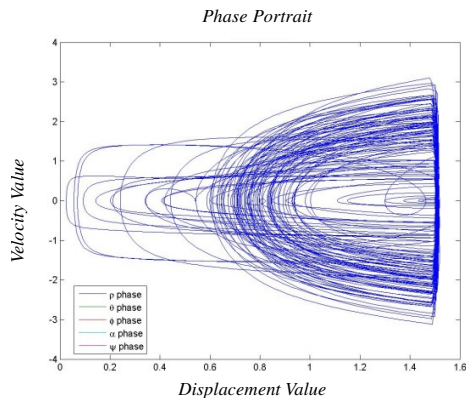


(e)

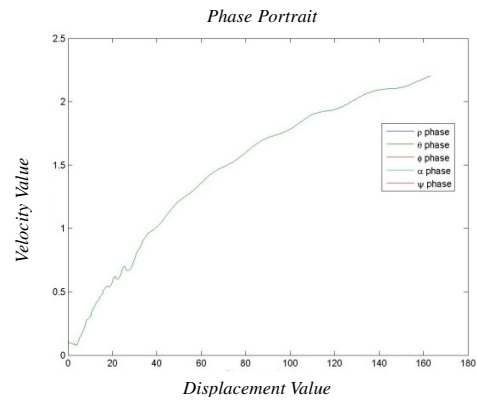
**Figure 3.8:** Four degree-of-freedom system responses for  $\mu=0.1$ : (a) radial displacement of rotor versus radial speed, (b) rotation angle of stator versus rate of change of rotation angle, (c) bending angle of rotor versus rate of change of bending angle, (d) rotation angle of rotor versus rate of change of rotation angle, and (e) trajectory of the center of rotor in horizontal plane, in polar coordinates  $(\rho, \theta)$ .

### 3.3.2 Numerical results for system with five degree-of-freedom

#### Case III: High friction coefficient case, $\mu = 0.9$



(a)



(b)

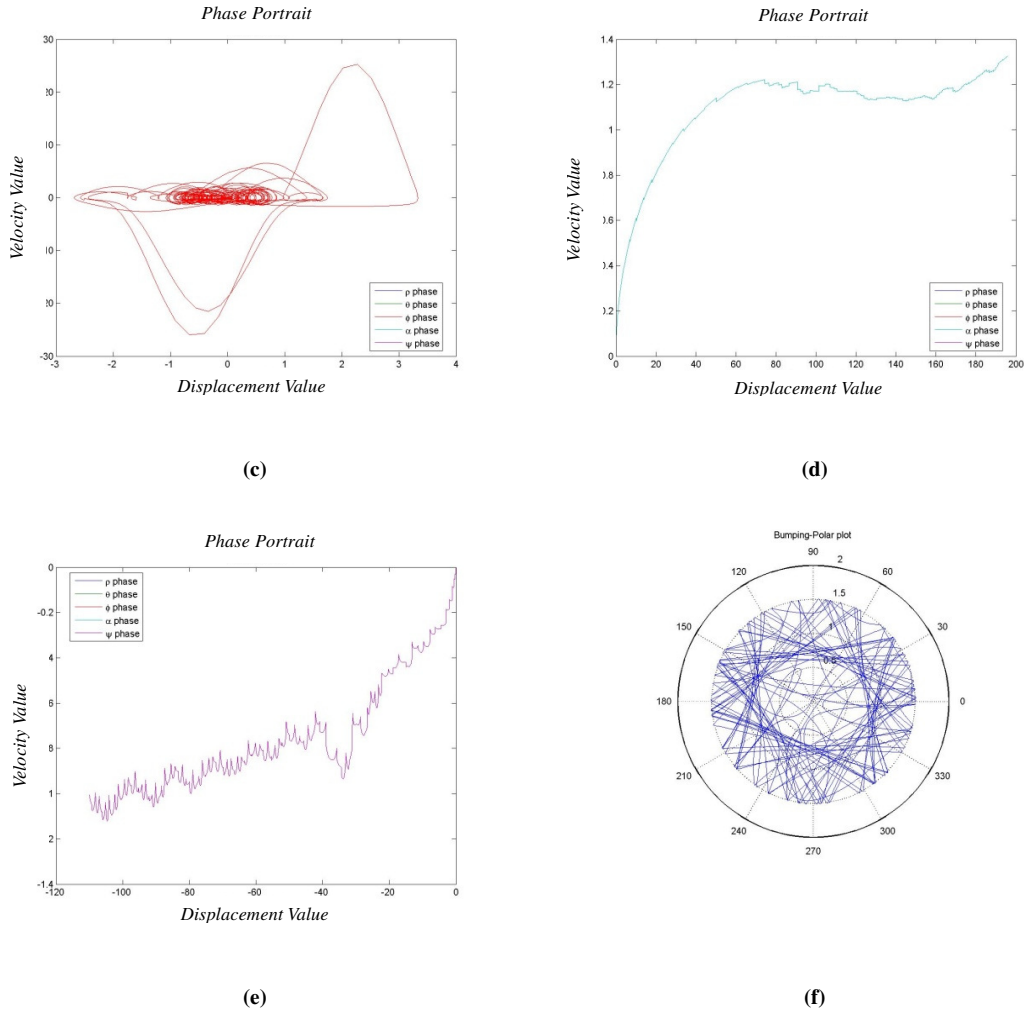


**Figure 3.9:** Five degree-of-freedom system responses for  $\mu=0.9$ : (a) radial displacement of rotor versus radial speed, (b) rotation angle of stator versus rate of change of rotation angle, (c) bending angle of rotor versus rate of change of bending angle, (d) rotation angle of rotor versus rate of change of rotation angle, (e) tilt angle of the rotor versus rate of change of tilt angle, and (f) trajectory of the center of rotor in horizontal plane, in polar coordinates  $(\rho, \theta)$ .

**Case IV: Low high friction coefficient case,  $\mu = 0.1$**

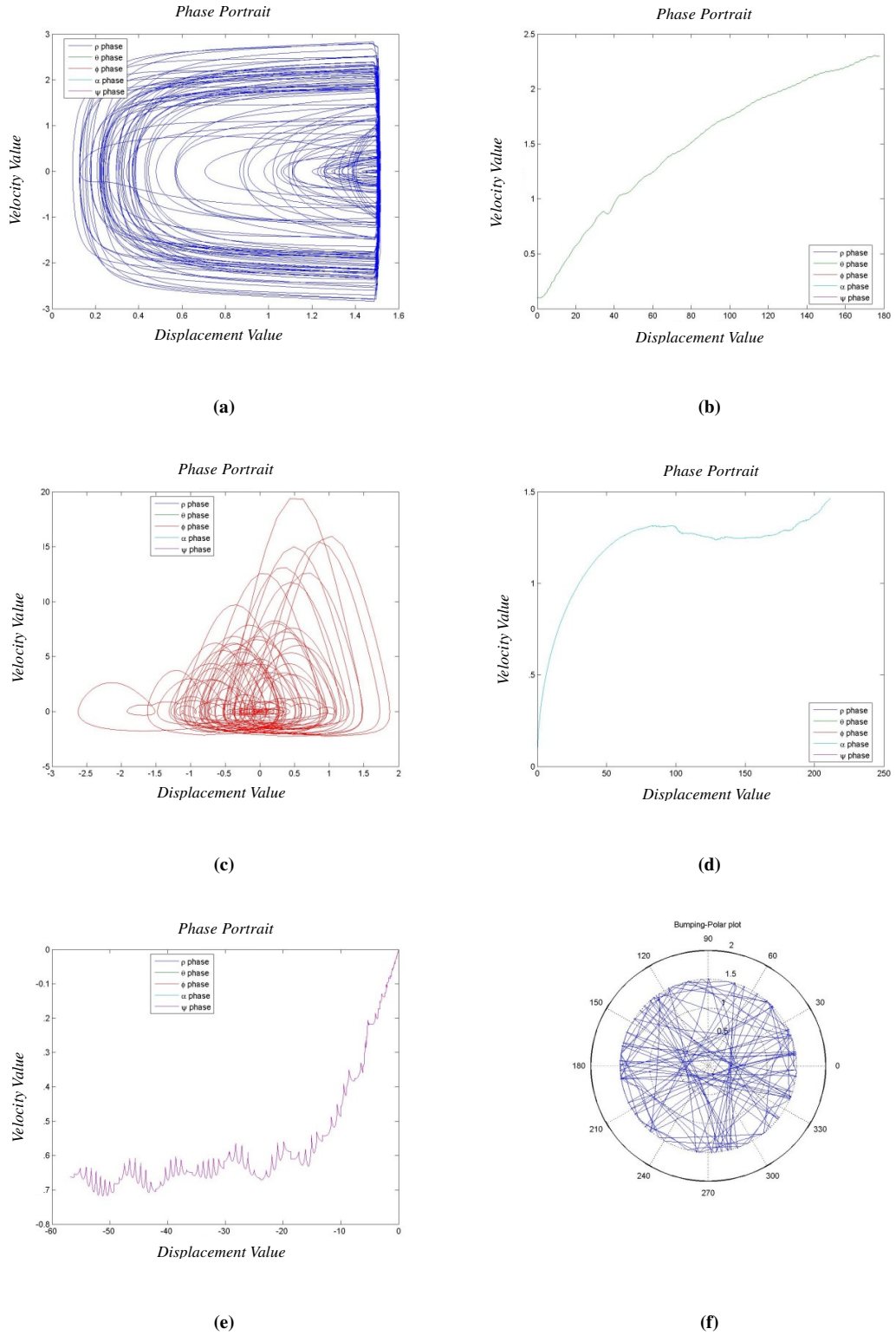


**Figure 3.10:** Five degree-of-freedom system response for  $\mu=0.1$ : (a) radial displacement

of rotor versus radial speed, (b) rotation angle of stator versus rate of change of rotation angle, (c) bending angle of rotor versus rate of change of bending angle, (d) rotation angle of rotor versus rate of change of rotation angle, (e) tilt angle of the rotor versus rate of change of tilt angle, and (f) trajectory of the center of rotor in horizontal plane, in polar coordinates  $(\rho, \theta)$ .

### **3.3.3 Discussion**

Comparing the results obtained in Cases I and II of Section 3.3.1 for the four degree-of-freedom model, it is clear that when the coefficient of friction is high, the trajectory of the drill string stays closer to the center for longer periods in contrast to the case with a lower coefficient of friction, when the drill string bounces from one end to the other. Considering the five degree-of-freedom system in Section 3.3.2, the system exhibits what appear to be aperiodic motions for both values of the friction coefficient. The drill-string dynamics is dominated by bumping motions, without the stick and slip aspects seen with the four degree-of-freedom system.

It should be noted that the results are highly dependent on the value of the initial radial displacement  $\rho_0$ . The movement of drill string depends on the contact friction, which determines sticking or slipping behavior. As the contact friction coefficient is changed, the magnitude of the friction force varies, as it is dependent upon the friction

coefficient  $\mu$ . Further, the friction force only acts once the rotor makes contact with the outer shell (i.e., the  $\lambda=1$  case). The initial radial displacement is a key determining factor for whether there is contact or not. In short, the friction coefficient determines the level of friction force while the initial radial displacement determines the chance of contact between the drill string and the outer shell.

### **3.4 Comparison of Model Predictions with Experimental Results**

In the previous sections, models for describing the drill-string system and analyses around equilibrium position have been carried out. In this section, comparisons are made between numerical results and experimental results from this dissertation work as well as previous work (Melakhessou *et al.*, 2003).

#### **3.4.1 Qualitative comparisons**

In Figure 3.11, the model predictions obtained from the four degree-of-freedom model are illustrated and are compared to experimental results for the parameter values given in Table 3.3.

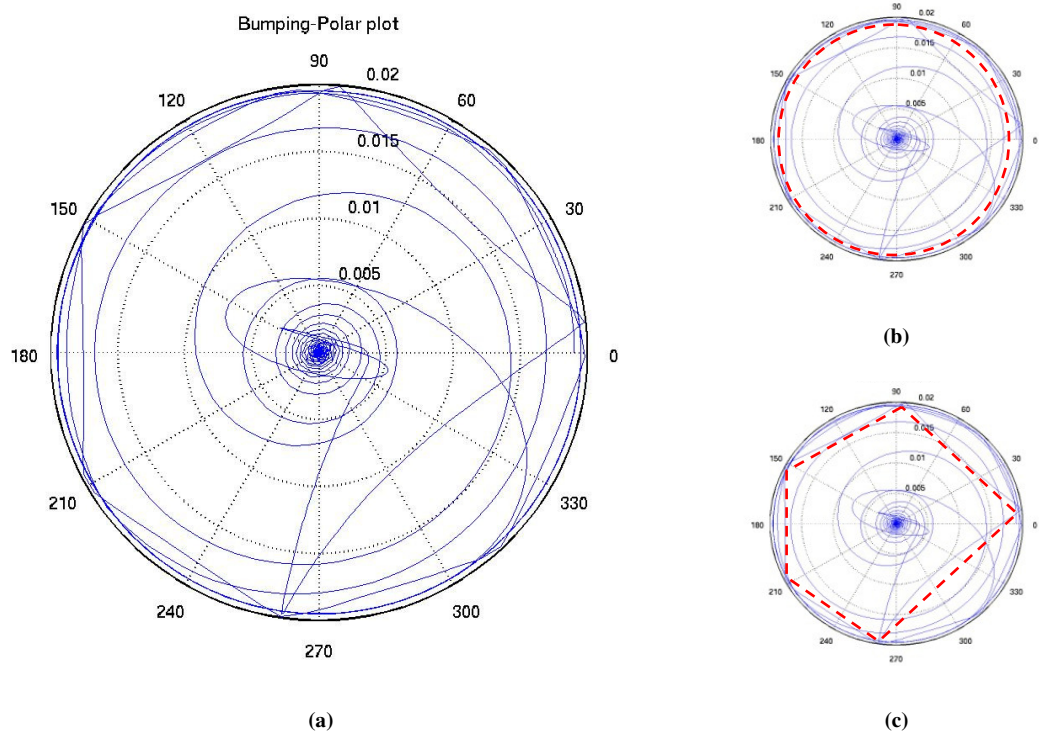


**Figure 3.11:** Numerical simulation of rotor motions corresponding to experiments: showing segments of rolling contact in (b) and bouncing contact in (c).

A friction coefficient value of 0.3 is used to make the predictions in the numerical simulations. The qualitative nature of the model predictions, in terms of rolling and bouncing phases of motions compare well with the experimental observations presented in Figures 2.4 and 2.5 in Section 2.2.

**Table 3.3: System parameter values used to generate numerical results for comparison with experimental results**

Parameters	Variable	Value	units
Mass of Rotor	$m$	$7.08 * 10^{-1}$	Kg
Unbalanced Mass on Rotor	$m_b$	$7 * 10^{-3}$	Kg
Stator Moment of Inertia	$I_1$	$5.9 * 10^{-3}$	$Kgm^2$
Rotor Moment of Inertia	$I_2$	$1.9 * 10^{-3}$	$Kgm^2$
Bending Stiffnesses I	$K_r$	27.2	$Nm^{-1}$
Bending Stiffnesses II	$K_t$	27.2	$Nm^{-1}$
Torsional Stiffnesses	$K_{TOR}$	4.69	$Nm^*rad^{-1}$
Stiffnesses of Outer Shell	$K_p$	$2.7 * 10^5$	$Nm^{-1}$
Outer Shell Inner Diameter	$D$	$1.91 * 10^{-1}$	m
Rotor Diameter	$d$	$1.52 * 10^{-1}$	m
Initial Position of Rotor	$\rho_0$	$1.9 * 10^{-2}$	m
Motor Torque	$\tau$	$2.05 * 10^{-2}$	Nm

### 3.4.2 Comparisons with results from literature

The differences seen between the results obtained with the dissertation’s four degree-of-freedom model and those obtained with the model of Melakhessou *et al.* (2003) is attributed to the manner in which the contact between the drill string and the outer shell is modeled here. The rotor trajectory predicted by equations (3.12)-(3.15) is compared with that presented in reference work in Figure3.10. The key difference between the results of the two studies is the consideration of stick-slip interactions in the current work.

The results of the current work are shown in Figures 3.12(a) to (c) for three different friction coefficient values and the corresponding results from reference work are shown

in Figures 3.12(d) to (f). It is seen that each time, the rotor makes contact with the outer shell there is a bouncing motion in the results of the reference work, whereas in the present case, the rotor can slide, roll, as well as bounce after a contact. While the results for a friction coefficient of 0.1 are similar in both cases, as the motions are dominated by bouncing contact, clear differences emerge as the friction coefficient value is increased. When the friction coefficient is 0.3, the rotor spends a considerable amount of time close to the radial center as shown in Figure 3.12 (b) without any contact with the outer shell. As the friction coefficient is increased to 0.9, as expected there are sliding motions as well in the results predicted by the current work. However, the results of reference work for this value of friction coefficient are not consistent with those obtained previously, since the rotor does not stay close to the radial center. From a practical standpoint, the case with intermediate value of friction coefficient is appealing, as the rotor spends more time close to the radial center, which is preferable for a drilling operation.

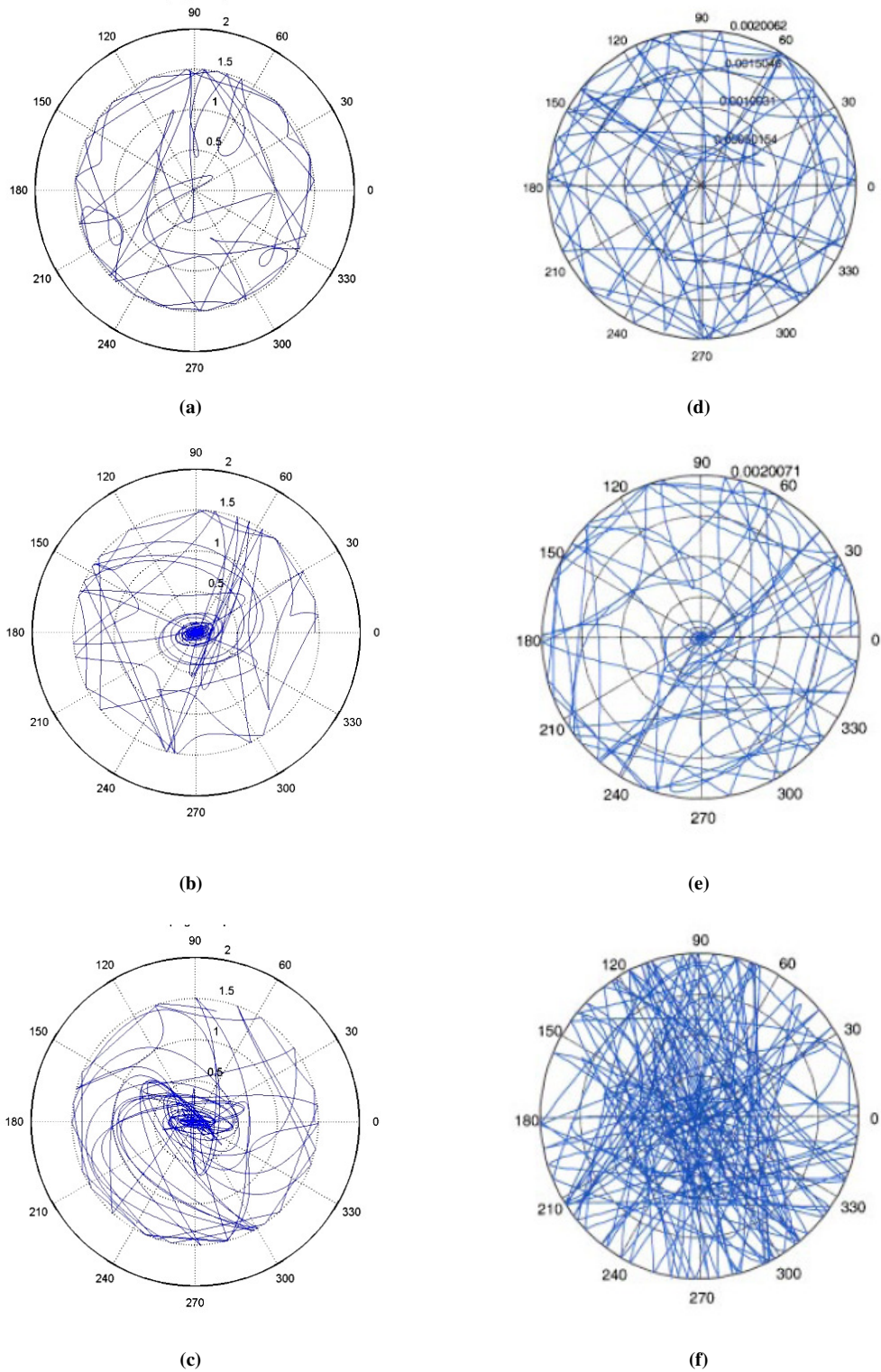


**Figure 3.12:** Comparison of simulation results of rotor trajectories in plane with polar coordinates  $(\rho, \theta)$ ; trajectory of the center of rotor: (a) initial position close to the outer

shell, friction coefficient  $\mu = 0.1$ ; (b) initial position close to the outer shell, friction coefficient  $\mu = 0.3$ ; and (c) initial position close to the outer shell, friction coefficient  $\mu = 0.9$ . The results obtained by using the modified four degree-of-freedom system are shown on the left column, and those obtained by using the model of Melakhessou *et al.* (2003) are shown on the right.

In Figure 3.13, the phase portrait projections of the radial motions as determined by the four degree-of-freedom model are shown along with the corresponding velocity time histories of the tangential component. Figures 3.13(a) to (c) correspond to the radial motion phase portrait projections, and Figures 3.13(d) to (f) correspond to the velocity time histories of the tangential component. Referring to the results of Figures 3.12 and Figure 3.13 (a) to (c), it is clear that the results in Figures 3.13(a) to (c) also show that the rotor stays closer to the radial center for a longer period of time as the friction coefficient is increased, but there is an intermediate value of the friction coefficient for which the rotor spends considerable amount of time close to the rotor center. The results shown in Figures 3.13(d) to (f) indicate that the number of tangential velocity jumps increases as the friction coefficient is increased, which is attributed to the impact between the rotor and the outer shell.

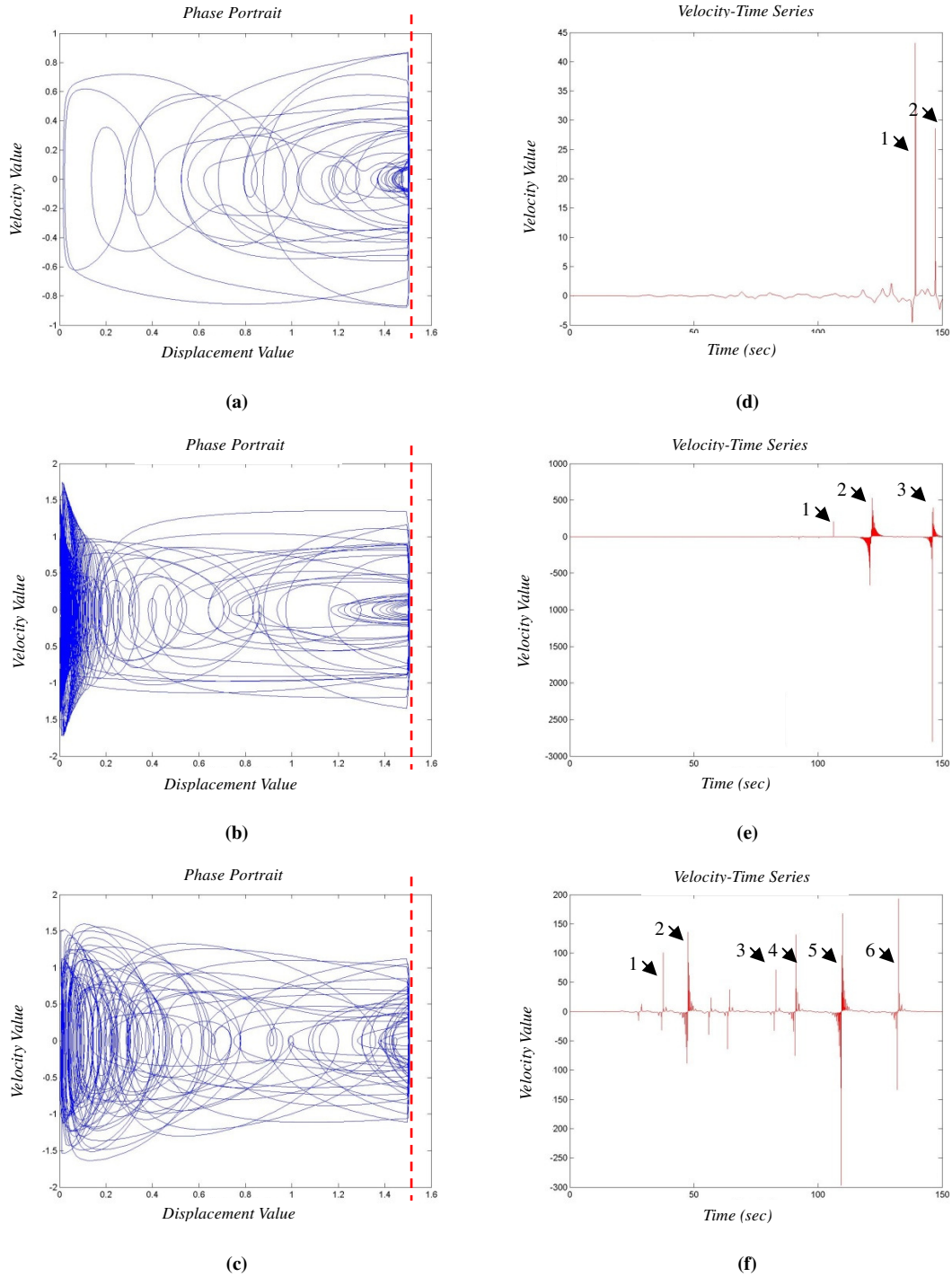
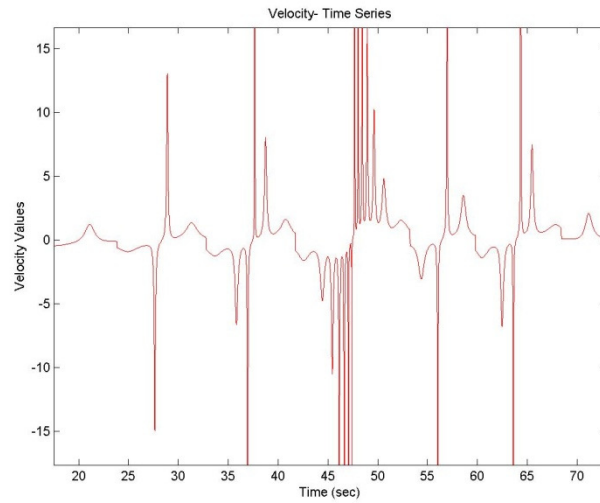
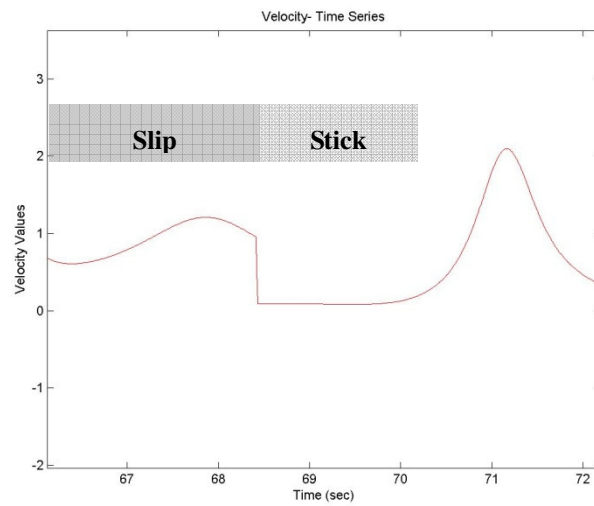


**Figure 3.13:** Phase portraits and time histories: (a) and (d) results for friction coefficient  $\mu = 0.1$ , (b) and (e): results for friction coefficient  $\mu = 0.3$ , and (c) and (f) results for friction coefficient  $\mu = 0.9$ . The dashed vertical line in the phase plots corresponds to the

outer shell.



(a)



(b)

**Figure 3.14:** Time history of tangential motion component: (a) complete record and (b) a portion showing slipping and sticking (Liao *et al.*, 2011).

In addition, the number of velocity changes also goes up with increase in friction coefficient value, suggesting that there is significant stick-slip interaction in these cases, as has been observed in other studies (e.g., Batako and Piiroinen, 2008). The results shown in Figure 3.13 (f) are revisited in Figure 3.14, to highlight the impacts that occur in the time window of 45 to 50 seconds and the stick-slip interactions that occur between the rotor and outer shell.

## **Chapter 4**

### **Parametric Studies**

In practice, erratic motions of rotor should be avoided for smooth operations and reducing system failures. Backward whirling is one of the major causes of drill string failures. Understanding the factors that cause backward whirling is a key to enhancing system stability. Here, parametric studies have been undertaken to examine the causes of backward whirling.

A parametric study is a way to monitor the system performance under various situations by selecting different system parameter values. As shown in Chapter 2, the drive speed has a key role in determining different types of rotor behavior. Continuing this work, changes in the rotor response with respect to different levels of unbalanced

mass, changes in the friction force (by changing contact surface material), and changes in the initial position of the rotor are explored in this section.

The effect of drive speed, levels of mass imbalance, and contact friction are experimentally studied and the findings are discussed in Section 4.1. The influence of initial position of rotor for different driving speeds is covered in Section 4.2.

## **4.1 Experimental Parametric Studies**

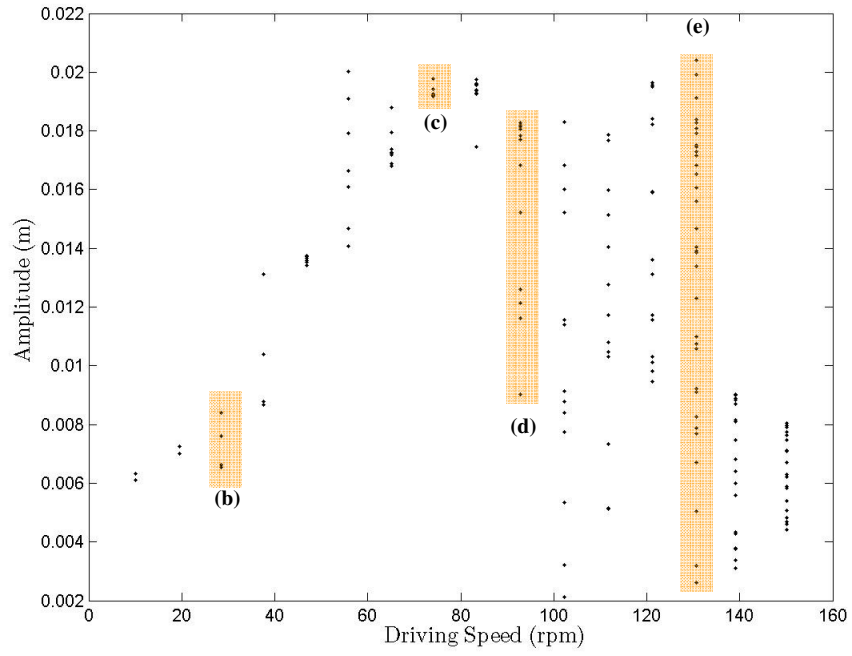
Here, qualitative changes in the system are studied with respect to changes in the following: i) driving speed of motor, ii) magnitude of unbalanced mass attached to the disc, and iii) friction coefficient between the outer shell and the disc at the bottom of the drill string.

### **4.1.1 Qualitative changes**

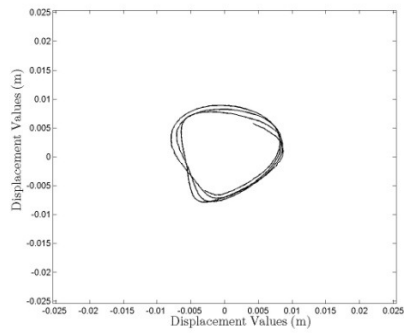
Rotor trajectories were traced and constructed by analyzing the position of the rotor within each frame of the video clip through image processing procedure, and representative examples of obtained results are presented in Figure 4.1. These examples are from experiments conducted with a rotor attached with 61.7 grams unbalanced mass in rubber-aluminum contact at different rotating speeds. Similar to results of Section 2.3, the rotor rotates around the center of shell region (Figure 4.1 (b)), and transitions

through a forward whirling phase (Figure 4.1 (c)), followed by a bumping phase (Figure 4.1 (d)), before reaching a backward whirling stage (Figure 4.1 (e)).

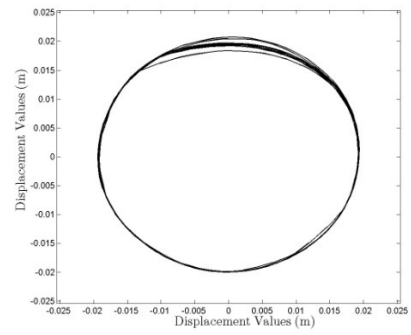
After collecting all the results obtained for the different driving speeds, the radial position of the rotor in time is re-sampled by using the motor driving speed as the clock frequency. Essentially, the radial displacement of rotor has been re-sampled at a rate equal to the driving frequency. In Figure 4.1 (a), these discrete time samplings are plotted in black dots with respect to the driving speed to create a diagram of qualitative changes, as common in experimental nonlinear dynamics (e.g., Nayfeh and Balachandran, 1995, 2006). Such diagrams can be used to understand the system response for a variety of driving speeds. When the rotor rotates periodically, such as shown in Figure 4.1 (c), a small group on black dots is seen on case (c) of Figure 4.1. On the other hand, a large spread of data points is indicative of an aperiodic motion of the rotor that can in some cases include bouncing motions and sticking motions shown as Figure 4.1 (e) and case (e) of Figure 4.1(a).



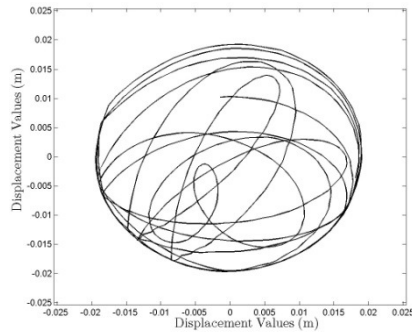
(a)



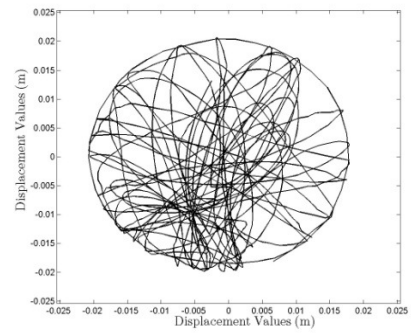
(b)



(c)



(d)



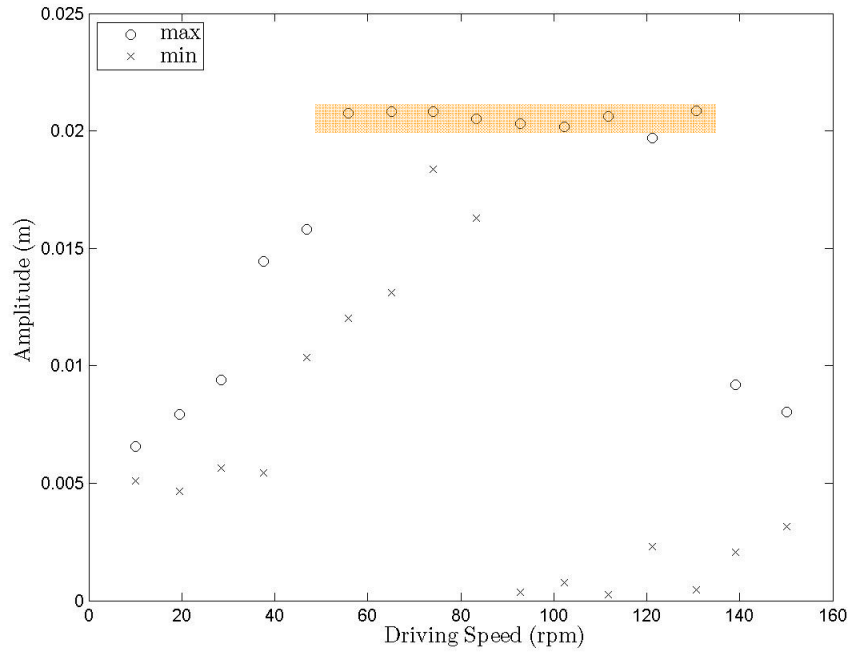
(e)

**Figure 4.1:** Rotor response with 61.7 grams unbalanced mass and aluminum-aluminum

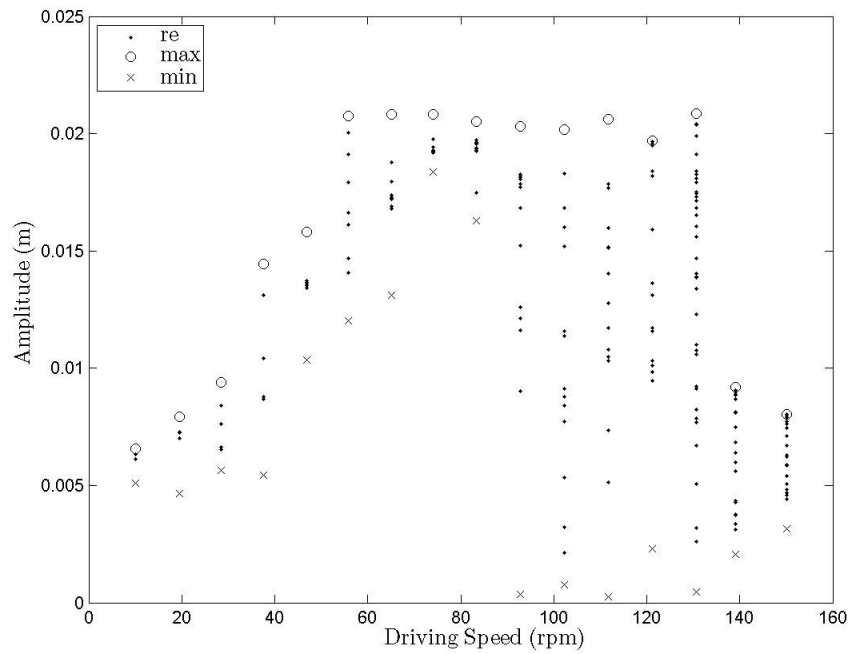
contact: (a) diagram of qualitative changes, (b) 28.3 rpm, (c) 74 rpm, (d) 92.5 rpm, and (e) 130 rpm.

The maximum and minimum values of rotor radial displacement over the whole time history can be used to pick up characteristics of rotor motions. In addition, the rotor motions may change after there is a contact with the outer shell. Therefore, it is important to determine whether or not contact has been made during the experiment. The extreme values of rotor radial displacement are plotted as a function of the driving speed in order to determine if there has been contact between the rotor and stator, as shown in Figure 4.2 (a). The light shaded region of Figure 4.2 (a) indicates that the rotor has made contact with the outer shell.

Combing the diagram of qualitative changes and extreme response values of rotor, a response characteristics diagram has been constructed to record rotor movements and determine certain system characteristics such as contact or noncontact dynamics and also the nature of the response, such periodic or aperiodic response. An example of the this diagram is shown as Figure 4.2 (b); this diagram contains the same information as Figure 4.1 (a) and Figure 4.2 (a).



(a)



(b)

**Figure 4.2:** Rotor response by 61.7 grams unbalanced mass and aluminum-aluminum

contact: (a) extreme values of radial displacement and (b) response characteristics diagram.

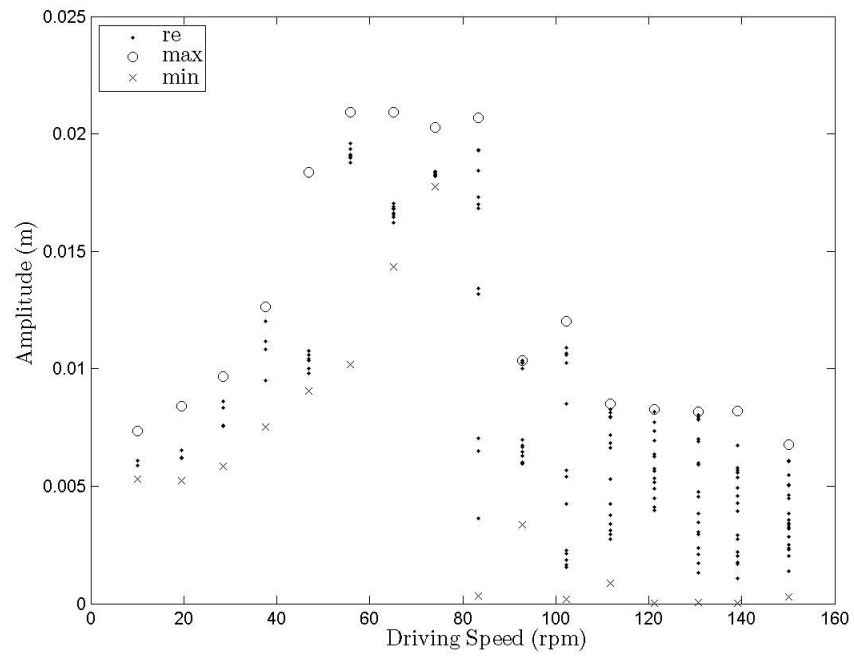
#### **4.1.2 Effect of mass imbalance**

The characteristic diagram presented in the earlier section can be used as a tool in parametric studies to examine the system performance for various conditions. In Figure 4.3, two sets of experimental results obtained with different level of unbalanced mass attached to the rotor and for rubber-aluminum contact are presented. In Figure 4.3 (a), the results are presented for an unbalanced mass of 28 grams, and in Figure 4.3 (b), the results are presented for the larger unbalanced mass of 61.7 grams. Comparing the results obtained for these two cases, it is evident that the rotor with the larger unbalanced mass shows bouncing motions in the drive speed range of 55 rpm to 130 rpm. By contrast, the rotor with the smaller unbalanced mass bumps onto the shell only in the drive speed range of 55 rpm to 82 rpm.

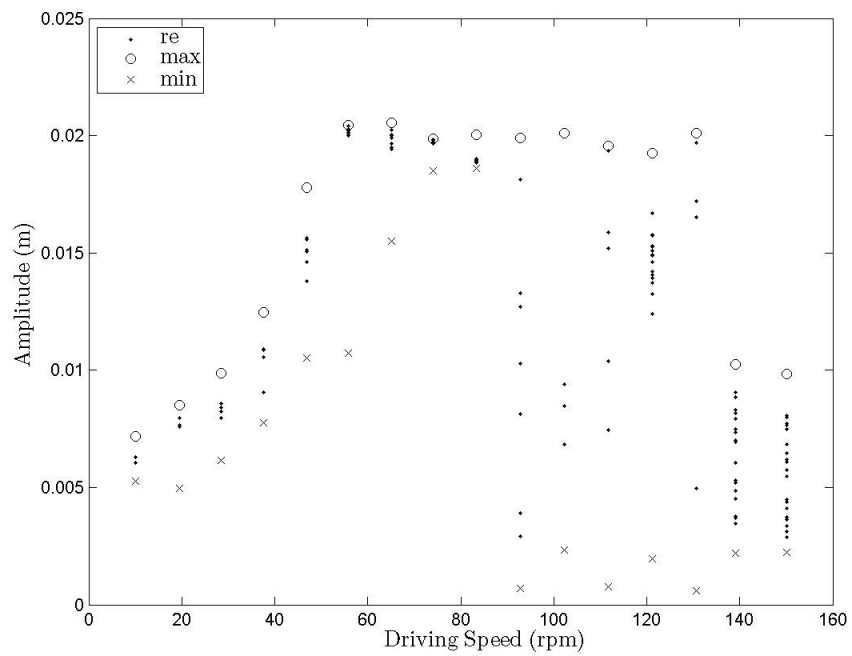
In more detail, in the range lower than 50 rpm, both of the sets share the same characteristics and the rotor moves about the center without contact. When the drive speed is around 55 rpm, the response of the rotor with smaller unbalanced mass shows bumping characteristics followed by forward whirling characteristics, but for the case with larger unbalanced mass, there is only pure forward whirling. When rotating at 82

rpm, the rotor with the smaller unbalanced mass exhibits bumping characteristics along with backward whirling. However, at this drive speed, the rotor with the larger unbalanced mass is still in the forward whirling phase. The rotor with the smaller unbalanced mass rotor rotates near the center of the shell with no contact when the drive speed is larger than 91 rpm. On the other hand, the rotor with the large unbalanced mass continues to show backward whirling up until 130 rpm.

For a given drive speed, the level of mass imbalance is influential in altering the nature of the observed response. From the experimental data, a few observations can be made: First, a rotor with large unbalanced mass has better likelihood of contacting the outer shell. Second, a system operated at a low rotating speed and with a large unbalanced mass can stay in the forward whirling phase for high driving speeds (e.g., 73 rpm to 82 rpm). Third, at higher driving speed cases, a rotor with large unbalanced mass is more likely to exhibit erratic movements such as bumping and also backward whirling.



(a)



(b)

**Figure 4.3:** Characteristic diagram of rotor response with rubber-aluminum contact: (a)

unbalanced mass of 28 grams and (b) unbalanced mass of 61.7 grams.

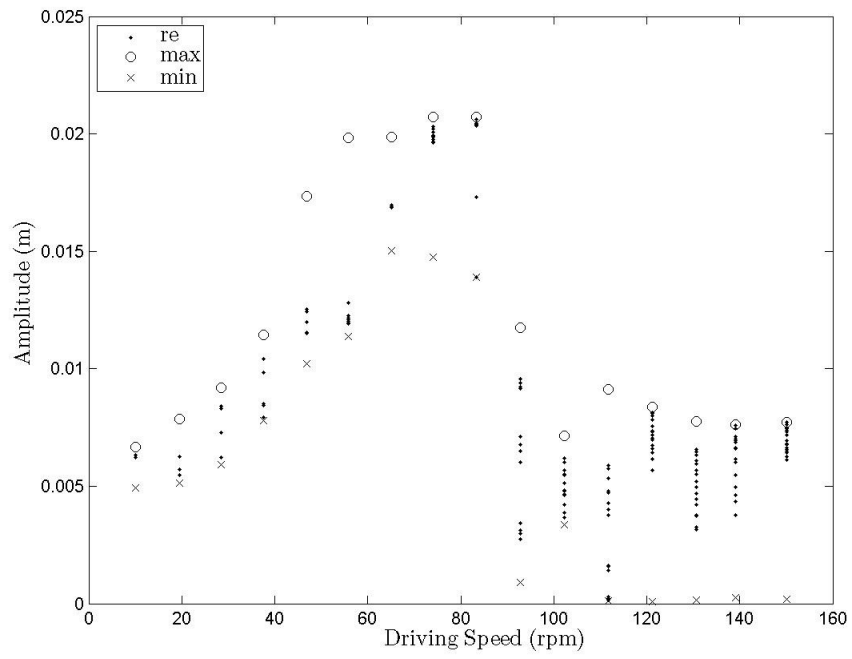
### **4.1.3 Influence of friction**

Contact friction is another factor which can cause rotor erratic movements. In order to study the effects of friction and its influence on the system, different combinations of rotor and outer shell contact surface have been used. Aluminum-aluminum, rubber-aluminum and rubber-rubber are the combinations used in this study, and as previously mentioned; they respectively correspond to low friction, moderate friction, and high friction cases.

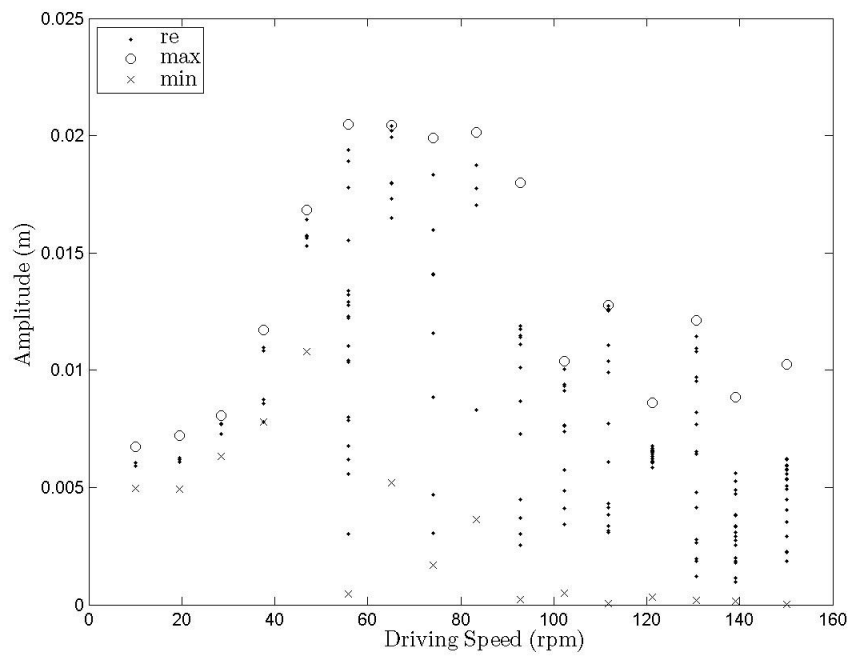
Results of rotor motions are shown in a characteristic diagram for a rotor with 28 grams unbalanced mass in Figure 4.4. In Figure 4.4 (a), results obtained with aluminum-aluminum contact combination are shown, and in Figure 4.4 (b), the results obtained for rubber-rubber contact combination are shown. There are only four cases that show bumping motions, and these cases lie within the drive speed range of 55 rpm to 82 rpm. These results also agree with the rubber-aluminum contact combination results presented in Figure 4.3 (a). More specifically, in the first and second case of 55 rpm and 64.5 rpm, the low friction setup shows bumping and forward whirling. This is also found to be the case with moderate friction. However, in the high friction setup, the rotor undergoes bumping and backward whirling. For the 74 rpm case, with the low friction

setup, the rotor motions exhibit forward whirling, while with moderate friction, the rotor motions exhibit bumping and forward whirling. With the high friction setup, the rotor exhibits bumping and backward whirling. For a drive speed of 82 rpm, forward whirling is also observed in the low friction setup. By contrast, for the same drive speed and moderate as well as high friction setups, the rotor exhibits bumping and backward whirling.

Generally speaking, within the four cases considered, the low friction configurations show bumping motions and transitions to forward whirling. By contrast, with the high friction setup, bumping motions followed by backward whirling are observed. With the moderate friction setup, the rotor response exhibits a combination of both bumping to forward whirling and bumping to backward whirling phases. In summary, the friction force is quite influential in altering the rotor motions when there is contact. Also, with high values of friction, the rotor is likely to undergo backward whirling, which is undesirable in real drilling operations.



(a)



(b)

**Figure 4.4:** Characteristic diagram of rotor response for 28 grams unbalanced mass: (a)

aluminum-aluminum contact and (b) rubber-rubber contact.

## **4.2 Numerical Parametric Studies**

Rotor impacts with the outer shell raise the possibility of system instability. Rotor operations close to the center and away from the shell is desirable in real drilling operations. However, in a real mining procedure, the drill string contacts the bore hole it creates several times throughout the drilling process. Thus, it is also important to know how the system responds after contact with the shell over a range of drive speeds.

In this section, numerical predictions made by using the models discussed in previous section are examined. The effect of having an initial position close to the shell, which generally leads to contact, are studied over a range of driving speeds.

### **4.2.1 Model description**

A constant rotation speed driving the system is assumed in order to replicate an actual drill rig. The four degree-of-freedom model reported in Section 3.1 can be cast in three-degree-of-freedom form when the drive speed is constant ( $\dot{\theta} = \omega$ ), which is equivalent to adding a constraint to the four-degree-of-freedom system. The equations of motion for this three-degree-of-freedom model are given in the form of equations (4.1) to (4.3):

$$(m + m_b) \ddot{\rho} - (m + m_b) \rho (\omega + \dot{\phi})^2 + K_r (\rho - \rho_0) + \lambda K_p (\rho - \delta) + K_t \rho \phi^2 - em_b (\ddot{\alpha} \sin(\beta) + \dot{\alpha}^2 \cos(\beta)) = 0 \quad (4.1)$$

$$(m + m_b) \rho^2 \ddot{\phi} + 2(m + m_b) \rho \dot{\rho} (\omega + \dot{\phi}) + K_t \rho^2 \dot{\phi} - em_b \rho (\dot{\alpha}^2 \sin(\beta) - \ddot{\alpha} \cos(\beta)) = -\lambda F_t \rho \quad (4.2)$$

$$(I_2 + m_b e^2) \ddot{\alpha} + K_{tor} (\alpha - \omega t) + em_b [-\ddot{\rho} \sin(\beta) + \rho \ddot{\theta} \cos(\beta) + \rho (\omega + \dot{\phi})^2 \sin(\beta) + 2 \dot{\rho} (\omega + \dot{\phi}) \cos(\beta)] = M_{ext} - \lambda F_t R \quad (4.3)$$

where  $\beta = \alpha - (\omega t + \phi)$

Equations (4.1) to (4.3) are descriptive of the time evolutions of the lateral or radial displacement, torsion displacement, and angular position of the rotor, respectively. The time derivatives of the different quantities are indicated by using dots on top of the corresponding quantities. For example, in equation (4.3),  $\dot{\rho}$  and  $\ddot{\rho}$  represent the first and second derivatives of radial displacement, respectively.

Reconsidering stick-slip interactions as in the Section 3.1, equation (3.27) has been rewritten (Liao, Vlajic, Karki, and Balachandran, 2011) as

$$F t_{equ} = \frac{\gamma K_t \rho \phi - K_{tor} (\omega t - \alpha)}{\frac{d}{2} - \gamma} \quad (4.4)$$

$$\text{where } \gamma = \frac{2 \cdot I_2}{m \cdot d} \quad (4.5)$$

Other than the mentioned equations above, the remaining equations of the force-interactions model have not changed. Numerical results are obtained by integrating the above equations for the system parameter values corresponding to the experimental

arrangement shown in Table 3.3.

#### **4.2.2 Influence of initial position and driving speed**

In Figure 4.5, the influence of initial rotor position on the system behavior is illustrated for different drive speeds with the same value of unbalanced mass (i.e., 70 grams). When the initial position of rotor is midway between the center of the outer shell and the edge of the outer shell, the rotor has less chance of coming into contact with the outer shell, as indicated by the results of Figure 4.5 (a) and Figure 4.5 (b). This finding illustrates again what has been noticed in the experiments. The transition from a circular orbit in Figure 4.5 (a) to a wrinkled orbit in Figure 4.5 (b) is solely due to the increase in the drive speed. In the cases of the results shown in Figures 4.5 (c) and 4.5 (d), the initial rotor position is close to the edge of the outer shell. The subsequent motions stay close to the center of the outer shell, with the bumping motions being more pronounced with an increase in the drive speed.

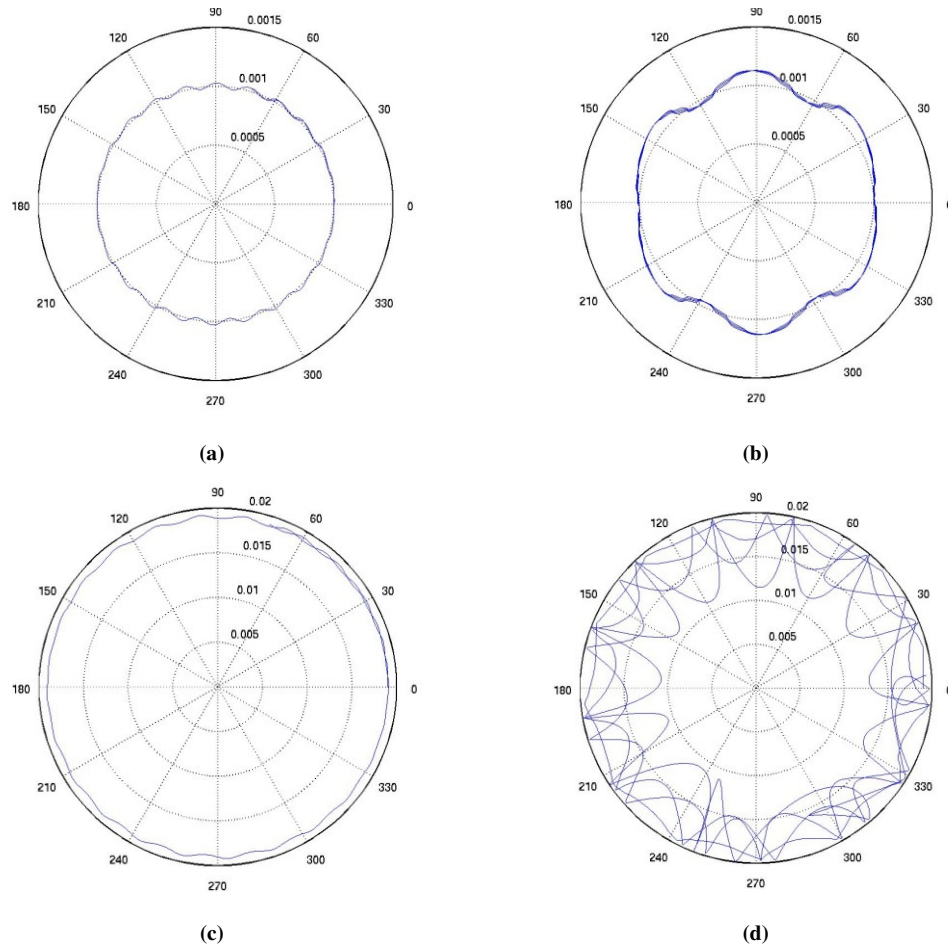


**Figure 4.5:** Rotor trajectory variation with respect to drive speed: (a) initial position midway between radial center and outer shell edge, and drive speed of 50 rpm; (b) initial position midway between radial center and outer shell edge, and drive speed of 200 rpm; (c) initial position close to outer shell and drive speed of 50 rpm; and (d) initial position close to outer shell with drive speed of 200 rpm.

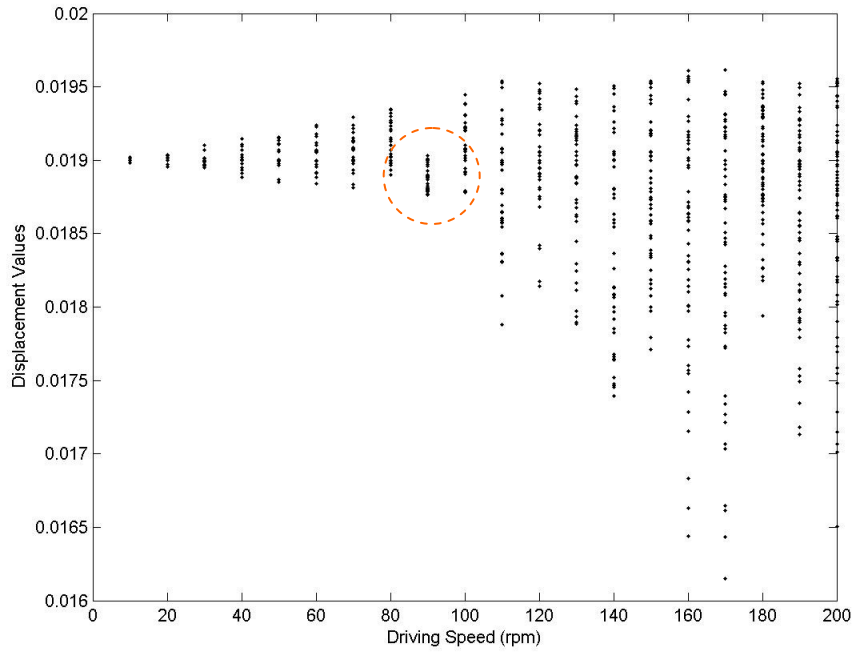
### 4.2.3 Results

As discussed earlier, in experimental nonlinear dynamics, it is common to construct plots of the system response versus a control parameter, which in this case is chosen as the

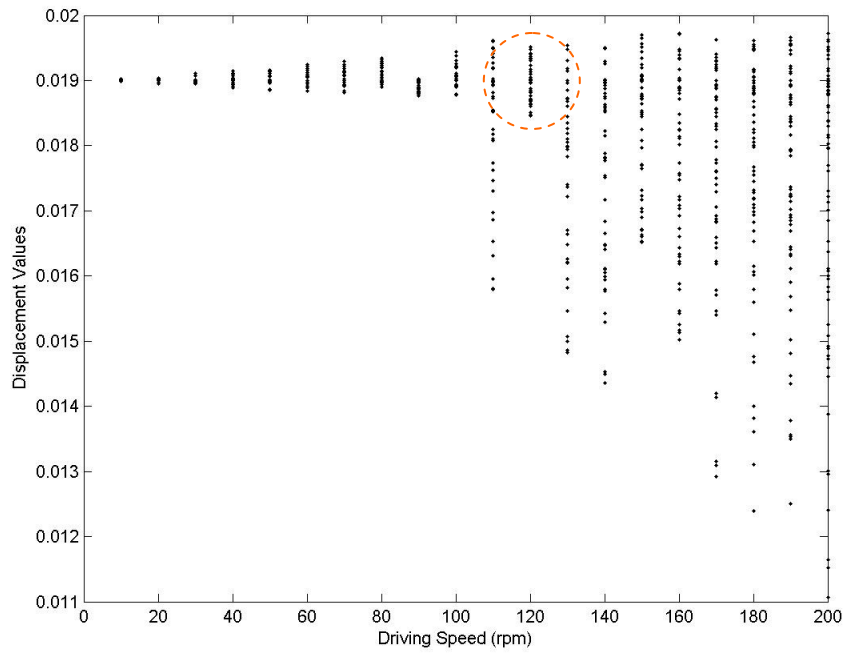
drive speed. Such plots are helpful to understand qualitative changes in the system behavior, as also illustrated in Section 4.1.

In the current studies, three different friction coefficient values and three different levels of unbalanced mass are used to generate the results shown in Figures 4.6 to Figures 4.8. The results of Figure 4.6 correspond to the lowest level of unbalanced mass at 10 grams. Likewise, the results of Figure 4.7 correspond to an intermediate level of mass imbalance at 30 grams, and the results of Figure 4.8 correspond to the highest level of mass imbalance at 80 grams.

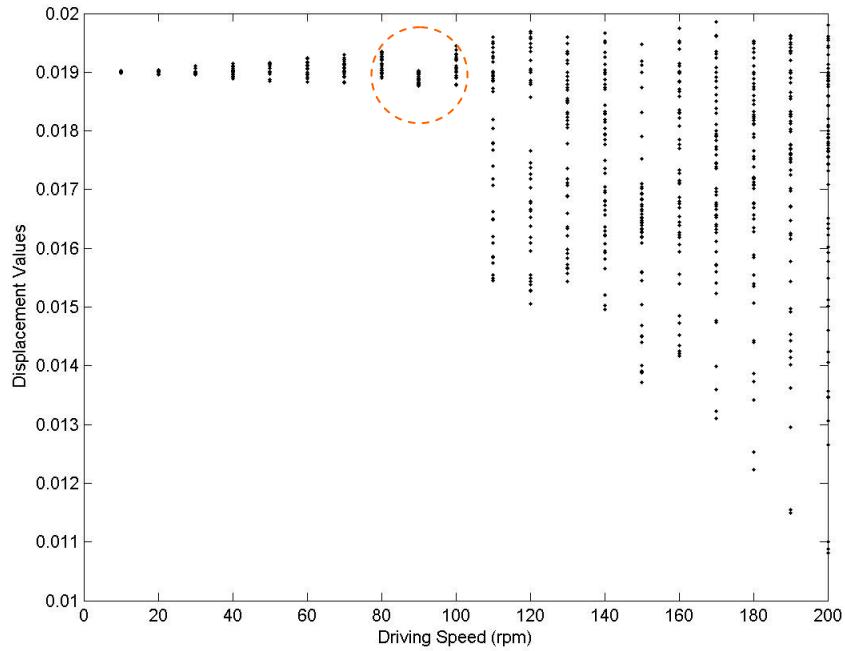
Focusing on the results of Figure 4.6, it is clear that for a low level of friction between the rotor and the outer shell, it takes a slightly higher drive speed for the system motions to become erratic as indicated by the spread of points on the corresponding slice, compared to the higher levels of friction. However, in all cases, there exists a certain driving speed where the rotor returns to the center of the shell, as indicated by a small radial spread of dots highlighted by the circles in the plots. This qualitative change in system dynamics has an important practical implication; that is, one can use the drive speed as a control parameter to avoid undesirable radial motions as well as to steer the system response to stay close to the radial center of a borehole. Similar qualitative trends are also observed in the results of Figures 4.7 and 4.8.



(a)



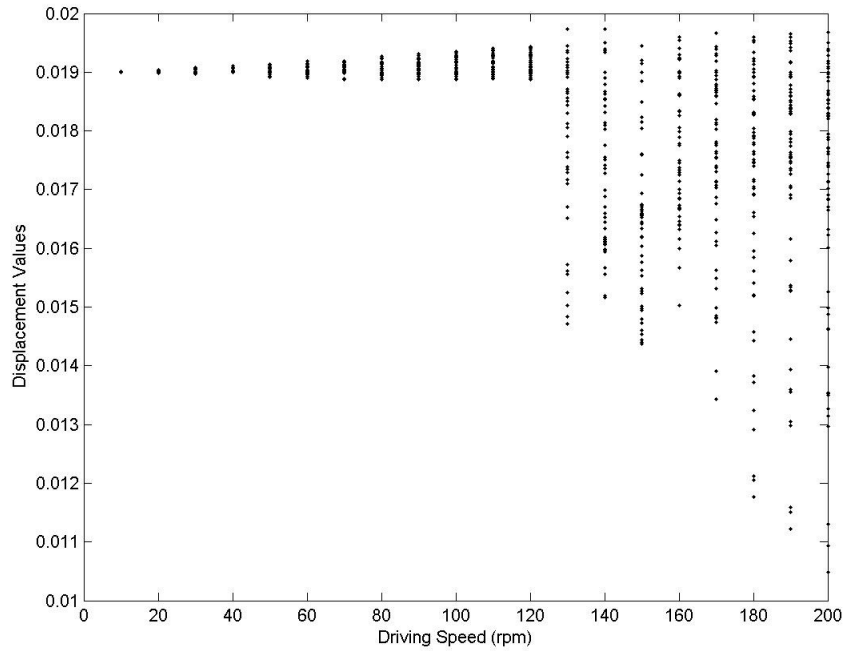
(b)



(c)

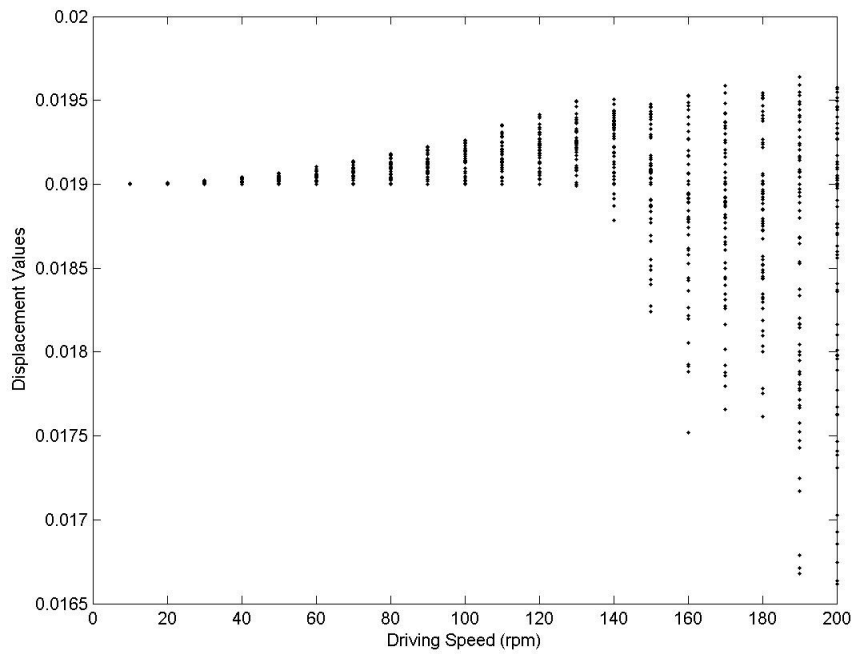
**Figure 4.6:** Characteristic diagram for lateral displacement response; the circles have been included to relate to the discussion made in the text: (a)  $m_b = 0.01$  and  $\mu = 0.1$ , (b)  $m_b = 0.01$  kg and  $\mu = 0.3$ , and (c)  $m_b = 0.01$  kg and  $\mu = 0.7$ .



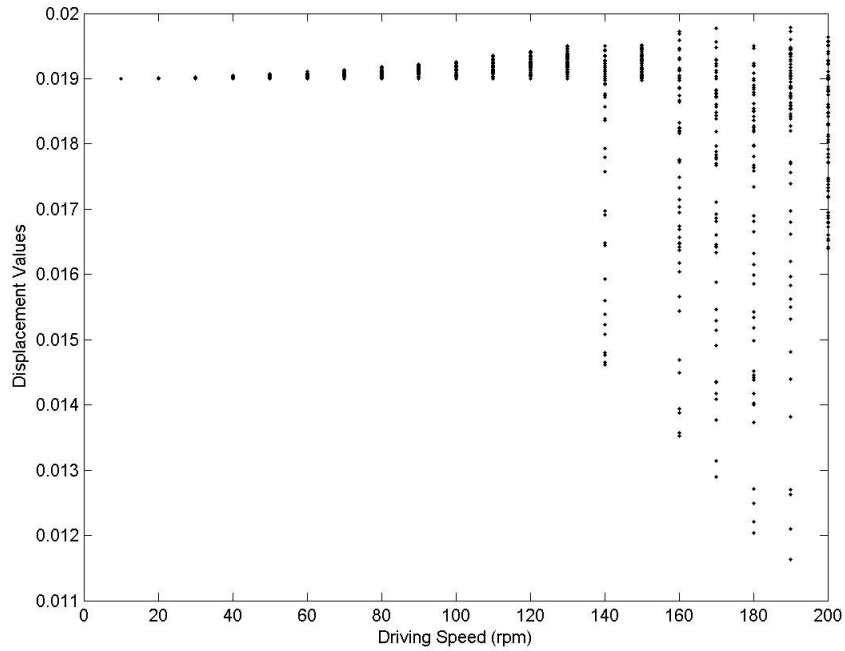


(c)

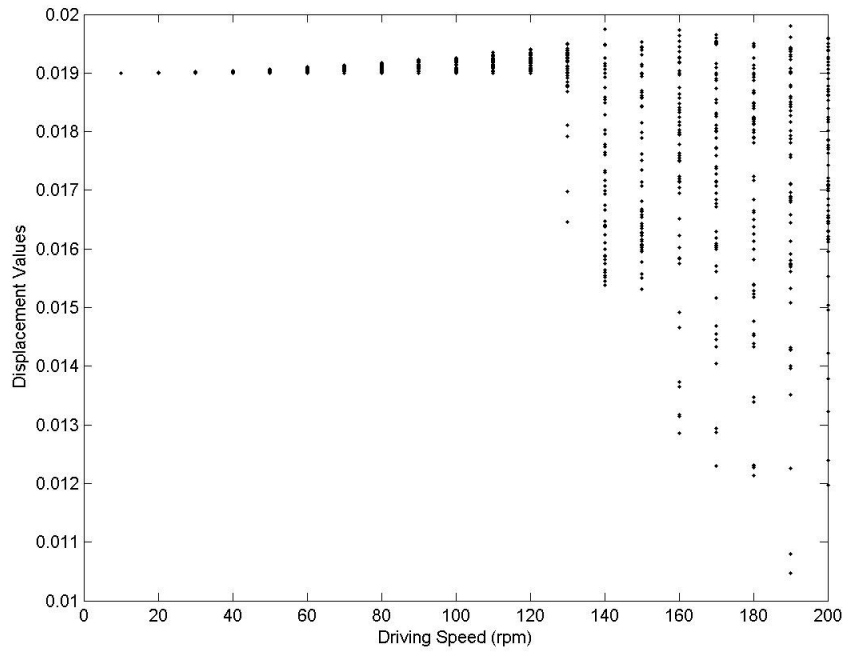
**Figure 4.7:** Characteristic diagram for lateral displacement response: (a)  $m_b = 0.03\text{kg}$  and  $\mu = 0.1$ , (b)  $m_b = 0.03$  and  $\text{kg}$   $\mu = 0.3$ , and (c)  $m_b = 0.03\text{kg}$  and  $\mu = 0.7$ .



(a)



(b)



(c)

Figure 4.8: Characteristic diagram for lateral displacement response: (a)  $m_b = 0.08\text{kg}$  and  $\mu = 0.1$ , (b)  $m_b = 0.08\text{kg}$  and  $\mu = 0.3$ , and (c)  $m_b = 0.08\text{ kg}$  and  $\mu = 0.7$ .

## **Chapter 5**

### **Summary and Recommendations for Future Work**

#### **5.1 Summary**

Within the dissertation, drill-string dynamics has been studied through a combined experimental, modeling, and numerical effort. Rotor dynamics along with contact dynamics have been studied within the unique long string with contact system. The experimental arrangement consists of a clamped-free rotor with unbalanced mass enclosed within a shell, and this unique arrangement has not been previously studied. This arrangement is used for studying both rotor dynamics and contact dynamics. The rotor motions have been decomposed into distinct phases, with each phase being associated with specific distinguishing characteristics. The dissertation findings can provide drilling operator insights into the movements of the drill string below the ground.

Two reduced order models, one with four degrees of freedom and another with five

degrees of freedom, have been derived to simulate the dynamics of a drill string. In particular, attention has been paid to the contact between the drill string and the outer shell, and the modeling allows the author to simulate bumping, sliding, and sticking motions. For low values of the friction coefficient, there are bumping motions between the drill string and the outer shell. The characteristics of these interactions change as the friction coefficient is increased. Additionally, the system exhibits sliding and sticking motions for higher values of friction.

Results obtained from the four degree-of-freedom model have been compared with those obtained through experiments as well as previous work. The model is found to be capable of predicting qualitative behavior observed in the experiments. The novelty of the developed reduced-order model is that it can account for stick-slip interactions, something which has not been covered in prior work.

Parametric studies reported here can serve as guideline for operating the drilling system. For the low friction contact condition and low level of unbalanced mass, the system is found to be regular in behavior for certain operating speeds. In the presence of high friction, a premature drill string failure may occur due to the erratic system response. With increasing level of unbalanced mass, which can be thought of as being representative of the curvature of the drill string, the rotor will stay close to the center of

the shell for low driving speeds, but exhibit erratic motions at high driving speeds. When contact occurs between the drill string and the borehole, an increase in the driving speed may bring the rotor back to the center of the shell, a location which is preferable for safe operations.

## **5.2 Future Work**

Some suggestions have been provided in the section for further studies in the following areas: i) model selection, ii) nonlinear phenomena, and iii) control schemes.

### **5.2.1 Distributed-parameter models with experiments**

Reduced-order models focusing on vertical drill-string dynamics have been studied in this work. For expanding the applications to capture more features such as initial curvature, a distributed-parameter model is needed. Finite-element discretization of a continuous model (e.g., Ritto *et al.*, 2009) may be a potential way to develop a model to mimic the whole drill-string system, especially, in horizontal drilling configurations. Non-dimensional analysis could also be considered to make the predictions have a broad applicability. Experiments focused on horizontal drilling, along with a corresponding distributed-parameter model, can be a bridge between the current work and studies with a full size drill-string system.

### **5.2.2 Five degree-of-freedom model with experiments**

The continuation of work with the five degree-of-freedom model through numerical simulations and experiments can form another path to study the system. The additional degree-of-freedom, tile angle, can allow the linking of the model to a continuous model for a better description of the whole drill-string system.

### **5.2.3 Nonlinear phenomena**

Although in this work, some drill-string nonlinear phenomena have been examined, other nonlinear oscillatory behavior and instabilities remain to be explored. If feasible, nonlinear analyses can be conducted along the lines of Leine and Nijmeijer (2004), Long, Lin, and Balachandran (2007), and Nguyen, Schultz, and Balachandran (2009) to study bifurcations in systems with discontinuities. Attention also needs to be paid to possible nonlinear coupling between bending vibrations and torsion vibrations and other modes of vibrations.

### **5.2.4 Control schemes**

Different control schemes can be studied with the experimental apparatus to determine their effectiveness. These schemes can include those that have been previously studied in the active control area (e.g., Baz and Poh, 1988; Pelinescu, 2002) and previous efforts related to drill stings (Canudas-de-Wit *et al.*, 2005; Corchero *et al.*, 2006).

## Appendix A

### Initial Experimental Design and Arrangement

Details of the initial experimental design as well as the experimental arrangement and different components of it are discussed below. These are the design to fulfill the motion detecting corresponding to reduce order models. The arrangement is slightly different than the setting in the presented work but the original experimental plan records all the possibilities including feedback controller and control scheme studies. Most of the possibilities and equipment had been studied or used to sensing best quality result. However, only the relevant setting to the presented work has been printed within the chapters.

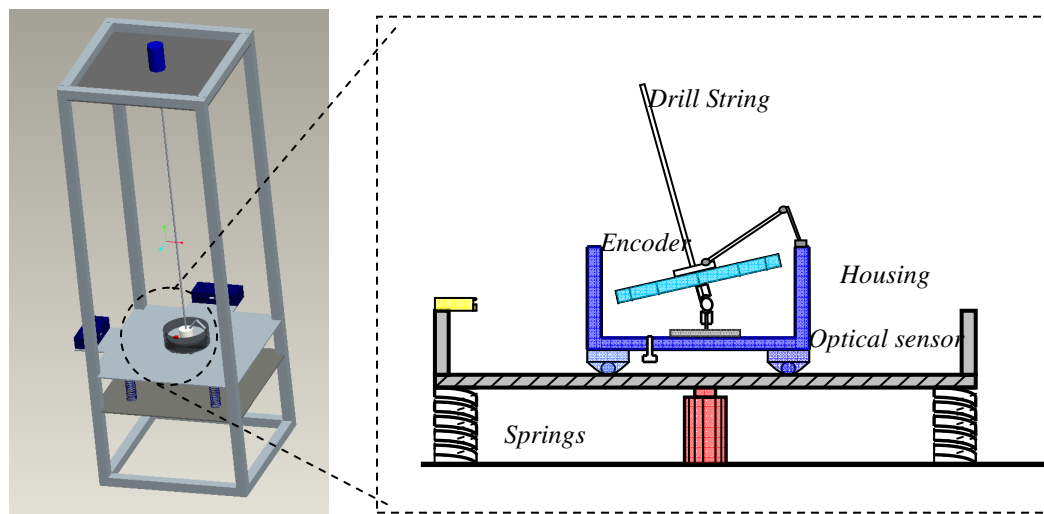


**Figure A.1:** Experimental arrangement to study bending-torsion vibrations (on the left)

with details at the bottom (on the right).

**Table A.1: Experimental components in design phase.**

<b>Item</b>	<b>Description</b>	<b>Figure</b>
<b>DC Motor</b>	A DC motor will be adapted as the main driving device to excite the system. This motor has the following features; i) maximum speed of 4000 rpm, ii) peak torque of 22.5 oz-in, and iii) a built-in rotary encoder.	A.12
<b>Rotating Discs</b>	There will be upper and lower discs in the system. The upper disc represents the rotary table of the drill string, and the lower disc represents the combination of the drill collar and drill bit. The diameters of the upper disc and lower disc are 12 inches and 6 inches, respectively.	A.13
<b>Encoder</b>	Absolute rotary encoders are to be used to measure the rotation angles of the discs. These encoders have a resolution of 2047 bits per revolution.	A.14
<b>Actuator</b>	An electro-magnetic actuator will be used to realize an axial loading in the 0-2.5kHz frequency range. This actuator is to be	A.15

	used to simulate the bearing capacity of the soil as well as to provide control input to the system.	
<b>Laser Displacement Sensor</b>	A laser sensor is to be used to measure the lateral movement of the bottom end of the drill string. This end is connected to the lower rotating disc and brake housing.	A.16
<b>Optical Sensor</b>	An optical sensor is to be placed on the brake housing to measure the tilt angle of the lower rotating disc.	A.17

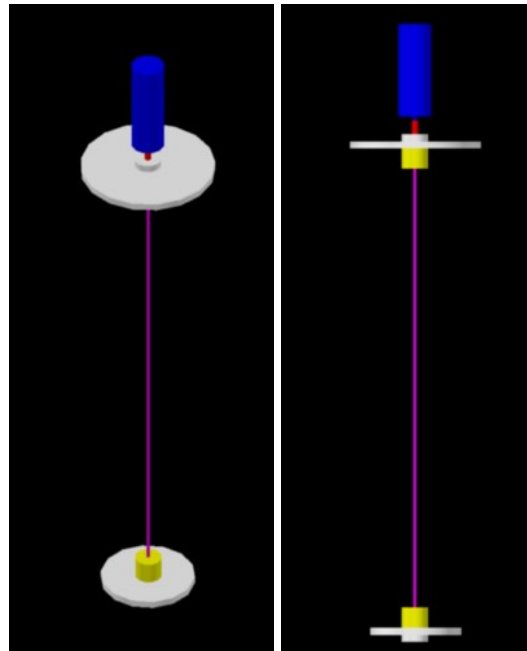


**Figure A.2:** Driving and transmission parts of the experiment.

**Design Details:**

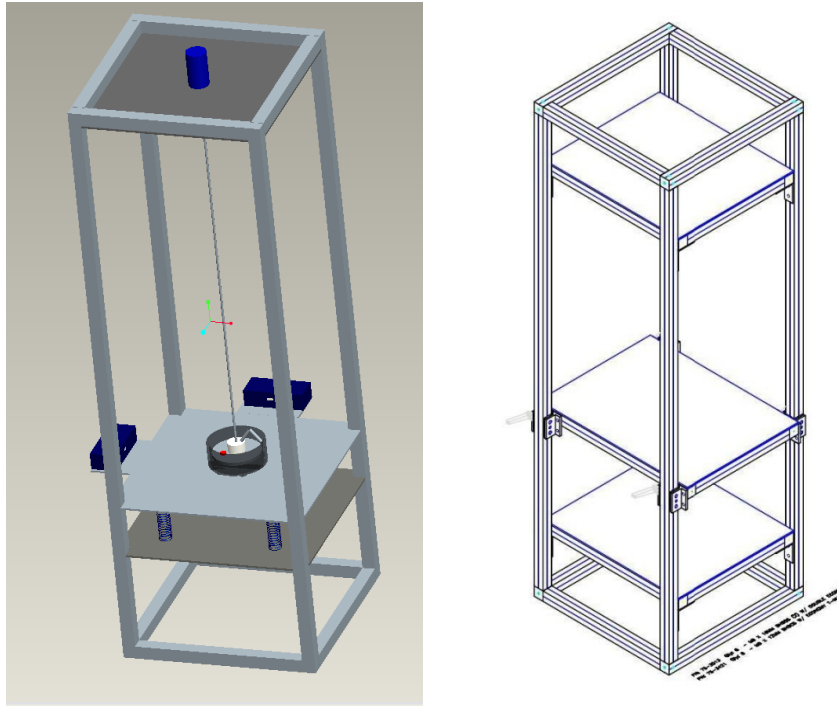


**Figure A.3:** Experimental setup on the left and main frame model on the right.

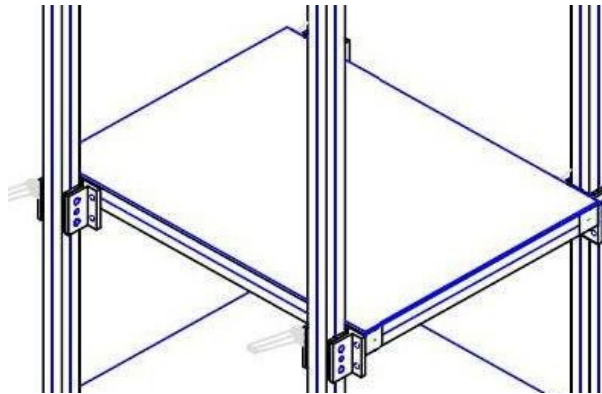


**Figure A.4:** Middle shelf held by linear bearings (to allow free sliding along the vertical direction).

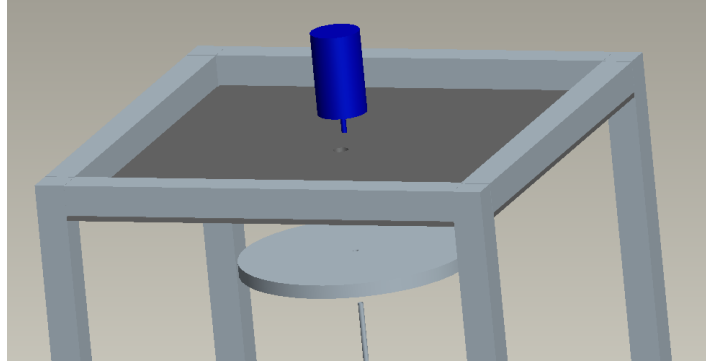


**Figure A.5:** Drive motor: motor mounted on top where the drive shaft is inserted through the hole made on the top panel to be screwed onto the upper disc by using a customized hexagonal connector.

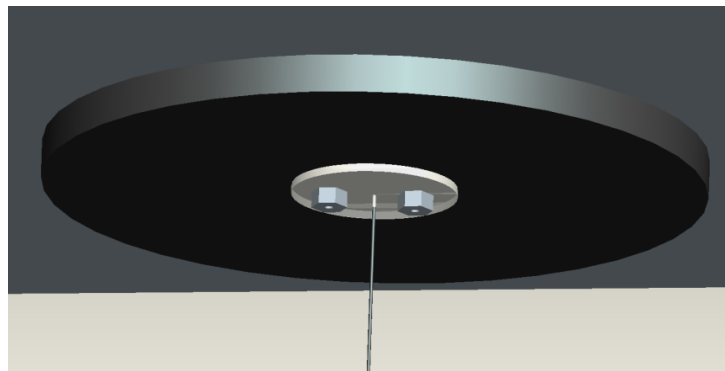


**Figure A.6:** Metal shaft with a disc on top to be bolted onto the upper disc. A metal string (drill string) is to be screwed onto the metal shaft.

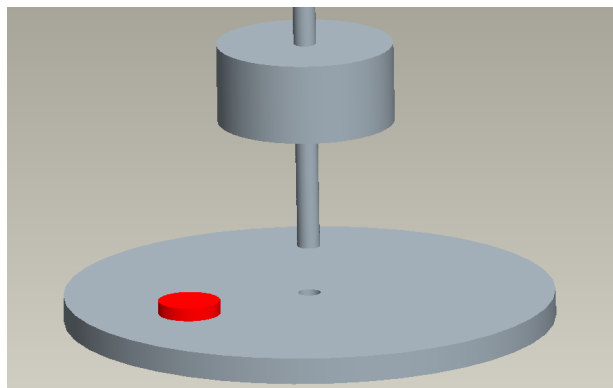


**Figure A.7:** Encoder to be placed at the lower end of the metal string. The metal string is

to be screwed onto the lower disc.

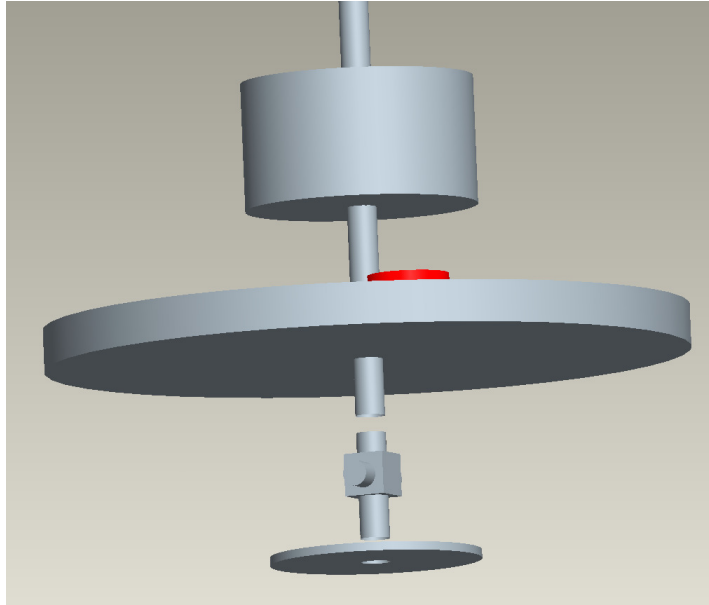


**Figure A.8:** Rotor with brake disc. The metal string coming out of the lower disc is to be connected to a universal joint which in turn is screwed onto the brake disc.

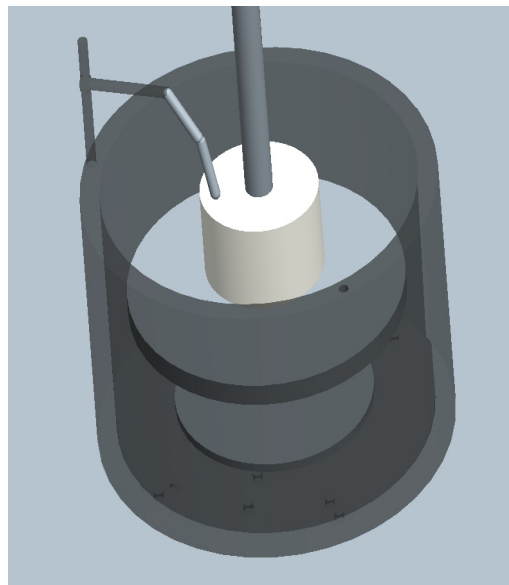


**Figure A.9:** Cylindrical housing that encloses the lower disc and the brake disc. The encoder (white) is to be attached to the housing by using a joint.

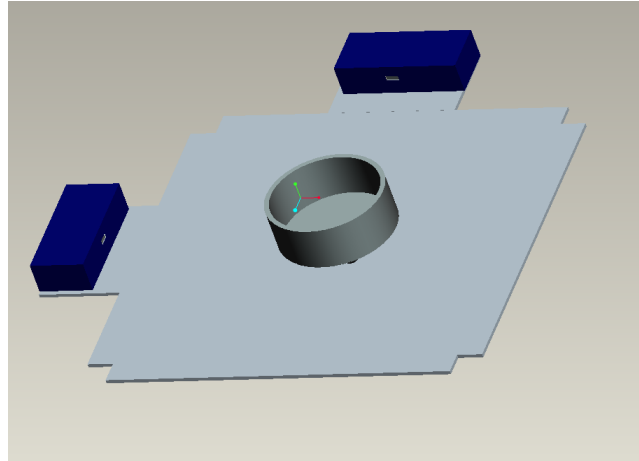


**Figure A.10:** Floating (middle) panel that supports the housing. Two laser triangulation sensors are to be placed on this panel. The panel is attached to the frame through linear bearings.

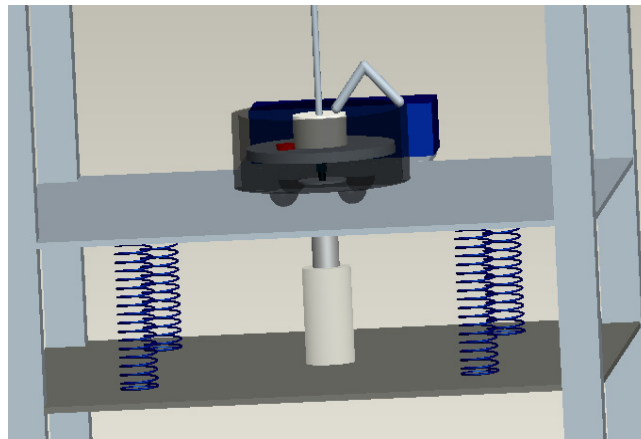


**Figure A.11:** Middle and lower panels. The housing rests on the middle panel. Four springs and one actuator are attached to both the middle and lower panels. The actuator is to be bolted whereas the springs are to be attached by using a horseshoe clamp.

**Experimental Components:**

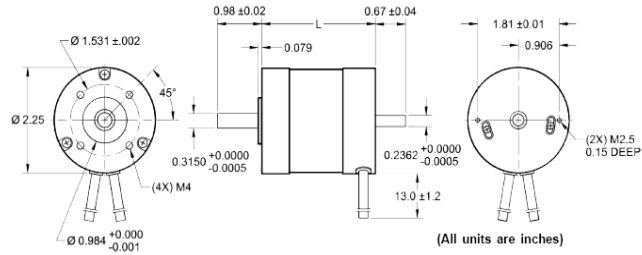


**Figure A.12:** DC motor scale diagram (Ref. Anaheim Automation).

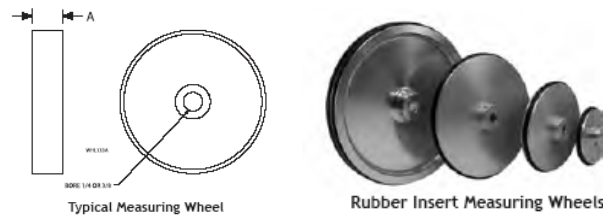


**Figure A.13:** Brake disc (Ref. Encoder Product Inc.).

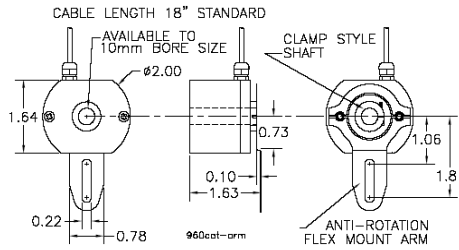


**Figure A.14:** Absolute encoder: model 960 (Ref. Encoder Product Inc.).

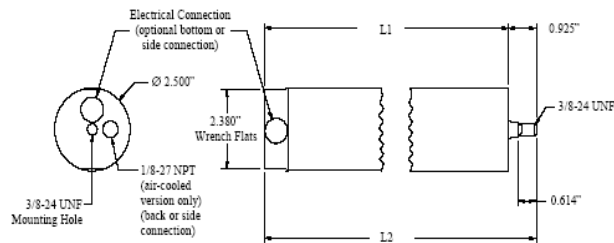


**Figure A.15:** Electro-magnetic actuator (Ref. ETREMA Inc.).

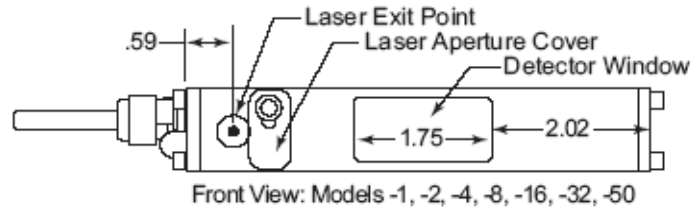


**Figure A.16:** Laser displacement sensor

(Ref. Acuity Laser Measurement).

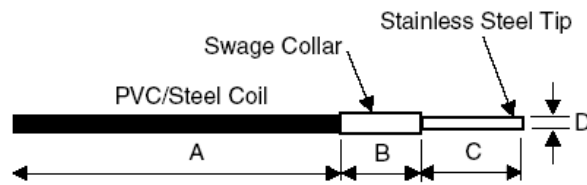


**Figure A.17:** Optical Sensor (Ref. Philtec Inc.).

**Experiment Arrangement:**



**Figure A.18:** Side view of arrangement.



**Figure A.19:** An isometric view of arrangement.



**Figure A.20:** Driving motor with circuit.



**Figure A.21:** Housing and bottom disc.

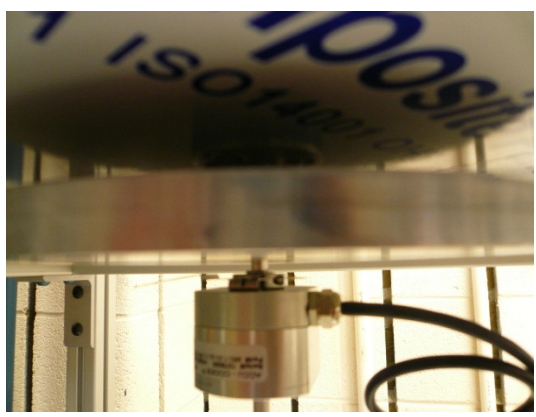


**Figure A.22:** Top disc with encoder

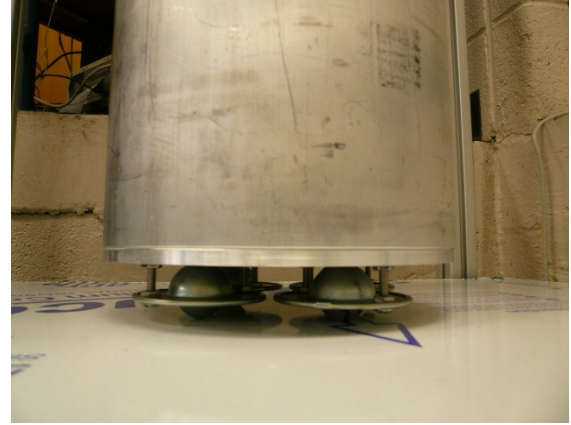


**Figure A.23:** Wheels under the housing



**Figure A.24:** Encoder supporting frame.

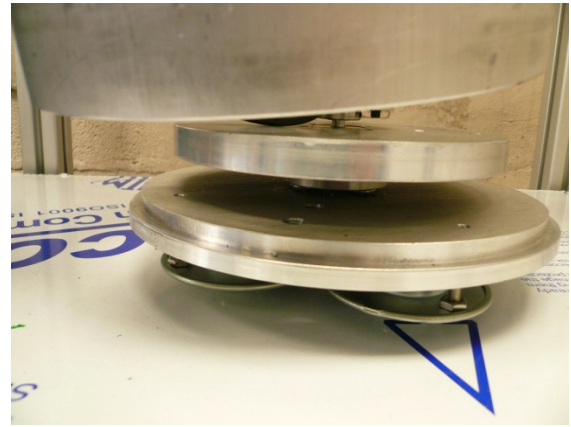


**Figure A.25:** Bottom disc with housing.

## Appendix B

### Derivation of Four Degree-of-Freedom Model

In this appendix, the four degree-of-freedom model presented by Melakhessou *et al.* (2003) is re-derived by using Lagrange's equations. This model is an extended version of an unbalanced rotor model, as illustrated by the two-section model shown in Figures 3.1 and 3.2. First, the kinetic energy, potential energy, and virtual work expressions are constructed.

#### Kinetic Energy

The system kinetic energy is composed of the kinetic energy of each section and of the kinetic energy of the unbalanced mass. The different components are as follows.

##### 1. Kinetic energy of Section I

The motion of Section I is a rotation around axis OZ with an angular speed  $\dot{\theta}$ ; thus, the energy is

$$T_1 = \frac{1}{2} I_1 \dot{\theta}^2 \quad (\text{B.1})$$

where  $I_1$  is the mass moment of inertia of Section I. The whole system rotates with an angular speed  $\dot{\theta}$ . It is assumed that there is no any lateral movement from the original axis OZ.

## 2. Kinetic energy of Section II

Section II has a mass  $m$  and a moment of inertia  $I_2$ . This section's center of mass has a radial motion  $\rho$  with respect to axis OZ and an angular speed  $\dot{\alpha}$ . Hence, the kinetic energy can be written as

$$T_2 = \frac{1}{2}m(\mathbf{V}_G \cdot \mathbf{V}_G) + \frac{1}{2}I_2\dot{\alpha}^2 \quad (\text{B.2})$$

where the velocity of the center of mass  $\mathbf{V}_G$  is

$$\mathbf{V}_G = \dot{\rho} \hat{\mathbf{n}} + \rho(\dot{\theta} + \dot{\varphi}) \hat{\mathbf{t}} \quad (\text{B.3})$$

## 3. Kinetic energy of Unbalanced mass

The position of the unbalanced mass  $m_b$  with respect to the origin  $O$  is written as

$$\mathbf{OM}_b = X \hat{\mathbf{i}} + Y \hat{\mathbf{j}} = (\rho \cos(\theta + \varphi) + e \cos(\alpha)) \hat{\mathbf{i}} + (\rho \sin(\theta + \varphi) + e \sin(\alpha)) \hat{\mathbf{j}} \quad (\text{B.4})$$

where the parameter  $e$  is distance between the axis of rotation of rotor and the unbalance mass

as shown in Figure 3.2. Thus, the kinetic energy is

$$T_b = \frac{1}{2}m_b \left( \frac{d(\mathbf{OM}_b)}{dt} \cdot \frac{d(\mathbf{OM}_b)}{dt} \right) = \frac{1}{2}m_b (e^2 \dot{\alpha}^2 + \dot{\rho}^2 + \rho^2 (\dot{\theta} + \dot{\varphi})^2) + 2e \dot{\alpha} [\rho(\dot{\theta} + \dot{\varphi}) \cos(\beta) - \dot{\rho} \sin(\beta)] \quad (\text{B.5})$$

where

$$\beta = \alpha - (\theta + \varphi) \quad (\text{B.6})$$

## 4. Ratio of Unbalanced Mass to Mass of Section II (rotor)

The unbalanced mass  $m_b$  is assumed to be relatively small compared to that the mass of Section II, when the total system kinetic energy is constructed; that is

$$m + m_b \approx m \quad (\text{B.7})$$

### 5. System Kinetic Energy

$$\begin{aligned} T &= T_1 + T_2 + T_b = \frac{1}{2} I_1 \dot{\theta}^2 + \frac{1}{2} m (\dot{\rho}^2 + \rho^2 (\dot{\theta} + \dot{\varphi})^2) + \frac{1}{2} I_2 \dot{\alpha}^2 + \\ &\frac{1}{2} m_b (e^2 \dot{\alpha}^2 + \dot{\rho}^2 + \rho^2 (\dot{\theta} + \dot{\varphi})^2) + 2e \dot{\alpha} [\rho (\dot{\theta} + \dot{\varphi}) \cos(\beta) - \dot{\rho} \sin(\beta)] \\ &\approx \frac{1}{2} I_1 \dot{\theta}^2 + \frac{1}{2} m (\dot{\rho}^2 + \rho^2 (\dot{\theta} + \dot{\varphi})^2) + \frac{1}{2} (I_2 + m_b e^2) \dot{\alpha}^2 \\ &\quad + m_b e \dot{\alpha} [\rho (\dot{\theta} + \dot{\varphi}) \cos(\beta) - \dot{\rho} \sin(\beta)] \end{aligned} \quad (\text{B.8})$$

## Potential Energy

### 1. Energy associated with Bending along Radial Direction

The potential energy associated with the radial bending of the drill string between

Sections I and II is expressed as

$$U_r = \frac{1}{2} K_r (\rho - \rho_0)^2 \quad (\text{B.9})$$

where  $K_r$  is the equivalent bending stiffness of the drill string along the radial direction and  $\rho_0$  is the distance between point O and  $O_1$  the origin of the  $O_1XYZ$  frame. The frame  $O_2XYZ$  shown in Figure 2.2 can be obtained from frame  $O_1XYZ$ , after going through an additional rotation  $\varphi$ .

### 2. Energy associated with Bending along Tangential direction

The potential energy associated with the tangential bending of the drill string between

Sections I and II is expressed as

$$U_t = \frac{1}{2} K_t (\rho\varphi)^2 \quad (\text{B.10})$$

where  $K_t$  is the equivalent bending stiffness of the drill string along the tangential direction. The deformation energy constructed along the tangential direction is based

on the assumption that the rotation angle  $\varphi$  is small, so that, one can state

$$\sin \varphi \approx \varphi.$$

### 3. Energy associated with Torsion of the rod

The potential energy associated with the torsion of Section II is constructed as

$$U_{tor} = \frac{1}{2} K_{tor} (\alpha - \theta)^2 \quad (\text{B.11})$$

where  $K_{tor}$  is the equivalent torsion stiffness of Section II.

### 4. Energy associated with Contact Deformation

The energy associated with radial deformation of the drill string when it contact with the outer shell (well bore) is constructed as

$$\begin{aligned} U_c &= \frac{1}{2} K_p (\rho - \delta)^2 \\ &= \frac{1}{2} K_p \left( \rho - \left( \frac{D}{2} - \frac{d}{2} \right) \right)^2 \end{aligned} \quad (\text{B.12})$$

where  $K_p$  is the contact stiffness,  $\rho$  is the radial position of the center  $O_2$  at time

$t$ ,  $\delta = \rho_0 + gap$ ,  $gap = \frac{D}{2} - \frac{d}{2} - \rho_0$ , and  $D$  and  $d$  represent the diameter of shell and

drill string, respectively. So,  $\delta = \frac{D}{2} - \frac{d}{2}$  is a constant; when  $\rho \geq \delta$ , the drill string is

making contact with the well bore or outer shell. To make it explicit that this energy

is zero when there is no contact, the contact parameter  $\lambda$  is introduced. When there is contact  $\lambda$  is 1 and it is zero otherwise. After introducing this contact parameter into equation (B.12), it can be rewritten as

$$U_c = \frac{1}{2} \lambda K_p (\rho - \delta)^2 \quad (\text{B.13})$$

### 5. System Potential Energy

$$U_{total} = \frac{1}{2} K_r (\rho - \rho_0)^2 + \frac{1}{2} K_t (\rho \varphi)^2 + \frac{1}{2} K_{tor} (\alpha - \theta)^2 + \frac{1}{2} \lambda K_p (\rho - \delta)^2 \quad (\text{B.14})$$

### Virtual Work

The external work done by the friction force  $F_t$  that acts along the tangential direction

and the torque  $M_{ext}$  applied to Section II is determined as

$$\delta W_{ext} = \lambda F_t [R(\delta\alpha) + \rho(\delta\theta + \delta\varphi)] + M_{ext} \delta\theta \quad (\text{B.15})$$

where  $\delta\alpha$ ,  $\delta\theta$ , and  $\delta\varphi$  are the corresponding virtual displacements.

After using equations (B.8), (B.14), and (B.15) and the extended Hamilton's principle

(e.g., Meirovitch, 2001), the equations of motion are obtained as shown below.

$$m \ddot{\rho} - m \rho (\dot{\theta} + \dot{\varphi})^2 + K_r (\rho - \rho_0) + \lambda K_p (\rho - \delta) + K_t \rho \varphi^2 = em_b (\dot{\alpha}^2 \cos(\beta) + \ddot{\alpha} \sin(\beta)) \quad (\text{B.16})$$

$$I_1 \ddot{\theta} + m \rho^2 (\ddot{\theta} + \ddot{\varphi}) + 2m \rho \dot{\rho} (\dot{\theta} + \dot{\varphi}) = -em_b \ddot{\alpha} \rho \cos(\beta) + em_b \rho \dot{\alpha}^2 \sin(\beta) + \lambda F_t \rho + M_{ext} \quad (\text{B.17})$$

$$m \rho (\ddot{\theta} + \ddot{\varphi}) + 2m \dot{\rho} (\dot{\theta} + \dot{\varphi}) + K_t \rho \varphi = -em_b \ddot{\alpha} \cos(\beta) + em_b \dot{\alpha}^2 \sin(\beta) + \lambda F_t \quad (\text{B.18})$$

$$I_2 \ddot{\alpha} + K_{tor} (\alpha - \theta) = -em_b ([2\dot{\rho}(\dot{\theta} + \dot{\varphi}) + \rho(\ddot{\theta} + \ddot{\varphi})] \cos(\beta) + [\rho(\dot{\theta} + \dot{\varphi})^2 - \ddot{\rho}] \sin(\beta)) + \lambda F_t R \quad (\text{B.19})$$

Equations (B.16)-(B.19) are given in Section 3.1 as equations (3.7) to (3.10). These

nonlinear equations can be put in the matrix form

$$[M]\{\ddot{X}\}+[C]\{\dot{X}\}+[K]\{X\}=\{F\} \quad (\text{B.20})$$

where the matrices and the states are given by

$$[X]=\begin{bmatrix} \rho \\ \theta \\ \varphi \\ \alpha \end{bmatrix} \quad (\text{B.21})$$

$$[M]=\begin{bmatrix} m & 0 & 0 & -em_b \sin(\beta) \\ 0 & I_1 + m\rho^2 & m\rho^2 & em_b \rho \cos(\beta) \\ 0 & m\rho & m\rho & em_b \cos(\beta) \\ -em_b \sin(\beta) & em_b \rho \cos(\beta) & em_b \rho \cos(\beta) & I_2 + m_b e^2 \end{bmatrix} \quad (\text{B.22})$$

$$[C]=\begin{bmatrix} 0 & -m\rho(\dot{\theta} + \dot{\varphi}) & -m\rho(\dot{\theta} + \dot{\varphi}) & -em_b \dot{\alpha} \cos(\beta) \\ 0 & 2m\rho \dot{\rho} & 2m\rho \dot{\rho} & -em_b \rho \dot{\alpha} \sin(\beta) \\ 0 & 2m \dot{\rho} & 2m \dot{\rho} & -em_b \dot{\alpha} \sin(\beta) \\ 0 & 2em_b \dot{\rho} \cos(\beta) & 2em_b \dot{\rho} \cos(\beta) & 0 \\ +em_b \rho \sin(\beta)(\dot{\theta} + 2\dot{\varphi}) & +em_b \rho \sin(\beta)(2\dot{\theta} + \dot{\varphi}) & & \end{bmatrix} \quad (\text{B.23})$$

$$[K]=\begin{bmatrix} \lambda K_p + K_r & 0 & K_t \rho \varphi & 0 \\ -\lambda F_t & 0 & 0 & 0 \\ K_t \varphi & 0 & 0 & 0 \\ 0 & -K_{tor} & 0 & K_{tor} \end{bmatrix} \quad (\text{B.24})$$

and

$$[F] = \begin{bmatrix} \lambda K_p \delta + K_r \rho_0 \\ M_{ext} \\ \lambda F_t \\ \lambda F_t \frac{d}{2} \end{bmatrix} \quad (\text{B.25})$$

## Appendix C

### Matlab Program

In this section, portions of a Matlab code used in the numerical integrations are provided.

```
%% Example of DS 4DOF model -Main

% Head
clear all;clear global;clc;%close all;

%% System Parameters
global m11 m12 m13 m14 m21 m22 m23 m24 m31 m32 m33 m34 m41 m42 m43 m44;           %[M]
global c11 c12 c13 c14 c21 c22 c23 c24 c31 c32 c33 c34 c41 c42 c43 c44;         %[C]
global k11 k12 k13 k14 k21 k22 k23 k24 k31 k32 k33 k34 k41 k42 k43 k44;         %[K]
global f11 f21 f31 f41;
                                %{f}
global tao; % tao=Mext
global m mb e I1 I2 gap thou0 DD d delta;% system constants  delta=thou0+gap;
gap=0.5*DD-0.5*d-thou0 ;delta=0.5*DD-0.5*d
global lambda kr kt ka kc % ka=ktor kc=kp
global Kr Kt KTOR Kp Delta Rho0;
global Ft Fte ft ftn fmax a b u temp % lambda=1 means contact with shell that time contact force=Ft

%% Experiment Value
m=0.7089; mb=0.01*7; e=0.0635; I1=3.84*10^-7; I2=1.84*10^-3; % I3=2; w=2*pi;
Kr=27.2; Kt=27.2; KTOR=4.69; Kp=2.7*10^5; DD=0.191; d=0.152; Rho0=0.019; u=1.05*0.1;   %Constant value
gap=0.5*DD-0.5*d-Rho0;                                % lambda =1; %ft=20; Ft=20;
Delta=0.5*DD-0.5*d;                                  % In Lagrangian code, is delta instead of Delta.
tao=0.0205*0.5;                                       %applied torque to the system on section II(rotor)
```

```
kr=Kr; kt=Kt; ka=KTOR; kc=Kp; delta=Delta; thou0=Rho0;
%% Time Parameters
t0 = 0;
dt = 0.001;
t1 = 7.4;
T0 = [t0:dt:t1];
a = 10;

%% Initial Conditions
x10 =thou0; x20 =0; x30=0; x40=0; %thou0=x10;
v10 =0; v20 =0; v30=0; v40=0;
Y0 = [x10,x20,x30,x40,v10,v20,v30,v40]';

%% Simulation
[t,q] = ode45('funhm3dofe',T0,Y0);
L = length(t);

%% Plot Results
figure(1);set(gcf,'Color',[1,1,1]);
plot(t,q(:,1),t, q(:,2)-q(:,4),t, q(:,3));xlim ([0,t1]);
legend('\rho','\theta -\alpha','\phi',0);
title('State Variable Time Series');
xlabel('Time (sec)');
ylabel('State Variable Values');

figure(2);set(gcf,'Color',[1,1,1]);
plot(t,q(:,5),t,q(:,6)-q(:,8),t,q(:,7));xlim ([0,t1]);
legend('\rho dot','\theta dot -\alpha dot','\phi dot',0);
title('Velocity- Time Series');
xlabel('Time (sec)');
ylabel('Velocity Values');

figure(3);set(gcf,'Color',[1,1,1]);
plot(q(:,1),q(:,5),q(:,2)-q(:,4),q(:,6)-q(:,8),q(:,3),q(:,7));
```

```

title('Phase Portrait');
xlabel('Displacement values');
ylabel('Velocity Values');

%% Example of DS 4DOF-function

%% Function
function dqdt=funhm3dofe(t,q); %q=4*2x1 form, neglect beta amd trans beta=alpha-(theta+phi); bdot=adot-thdot+pdot

% System Parameters
global m11 m12 m13 m14 m21 m22 m23 m24 m31 m32 m33 m34 m41 m42 m43 m44;           % [M]
global c11 c12 c13 c14 c21 c22 c23 c24 c31 c32 c33 c34 c41 c42 c43 c44;         % [C]
global k11 k12 k13 k14 k21 k22 k23 k24 k31 k32 k33 k34 k41 k42 k43 k44;         % [K]
global f11 f21 f31 f41;
        % {f}
global tao w; % tao=Mext
global m mb e I1 I2 gap thou0 DD d delta;% system constants   delta=thou0+gap;
gap=0.5*DD-0.5*d-thou0 ;delta=0.5*DD-0.5*d
global lambda kr kt ka kc % ka=ktor kc=kp
global Kr Kt KTOR Kp Delta Rho0;
global Ft Fte ft fn a u fmax temp % lambda=1 means contact with shell that time contact force=Ft

% relative definition
kr=Kr*a; kt=Kt*a; ka=KTOR; kc=Kp*a; delta=Delta; thou0=Rho0;

% IF loop; judgment of contact and non-contact: contact lambda=1 and Ft=ft
delta=0.5*DD-0.5*d;
if abs(q(1)) <= delta;
    lambda = 0;
    Ft = 0;
else;
    lambda = 1;
    ftn = kc*(abs(q(1))-delta);
    ftn = -u*ftn;

```

```

Fte = -sign(tao/0.5*d)*tao/((I2/0.5*d*m)+0.5*d);
if (q(1)*(q(6)+q(7))+0.5*d*q(8)) ~= 0; %relative velocity not equal to zero
    ftn = kc*(abs(q(1))-delta);
    ft = -u*(sign(q(1)*(q(6)+q(7))+0.5*d*q(8)))*ftn; %friction force after contact with outer surface
    Ft = ft;
else % (q(1)*(q(6)+q(7))+0.5*d*q(8)) = 0; %relative velocity equals to zero
    if abs(ftmax) >= abs(Fte);
        Ft = Fte;
    else
        Ft = ftmax;
    end
end;
end;
end;

```

```

%% indicate value of M matrix
m11=m+mb;
m12=0;
m13=0;
m14=-1*mb*e*sin(q(4)-(q(2)+q(3)));
m21=0;
m22=(m+mb)*(q(1)^2)+I1;
m23=(m+mb)*(q(1)^2);
m24=mb*e*q(1)*cos(q(4)-(q(2)+q(3)));
m31=0;
m32=(m+mb)*(q(1)^2);
m33=(m+mb)*(q(1)^2);
m34=mb*e*q(1)*cos(q(4)-(q(2)+q(3)));
m41=-1*mb*e*sin(q(4)-(q(2)+q(3)));
m42=mb*e*q(1)*cos(q(4)-(q(2)+q(3)));
m43=mb*e*q(1)*cos(q(4)-(q(2)+q(3)));
m44=I2+mb*e^2; %m44=I2+mb*e^2=I2;

```

```

%% indicate value of C matrix
c11=0;
c12=-1*(m+mb)*q(1)*(q(6)+q(7));

```

```

c13=-1*(m+mb)*q(1)*(q(6)+q(7));
c14=-1*e*mb*q(8)*cos(q(4)-(q(2)+q(3)));
c21=0;
c22=2*(m+mb)*q(1)*q(5);
c23=2*(m+mb)*q(1)*q(5);
c24=-1*e*mb*q(1)*q(8)*sin(q(4)-(q(2)+q(3)));
c31=0;
c32=2*(m+mb)*q(1)*q(5);
c33=2*(m+mb)*q(1)*q(5);
c34=-1*e*mb*q(8)*q(1)*sin(q(4)-(q(2)+q(3)));
c41=2*mb*e*(q(6)+q(7))*cos(q(4)-(q(2)+q(3)));
c42=e*mb*q(1)*(q(6)+q(7))*sin(q(4)-(q(2)+q(3)));
c43=e*mb*q(1)*(q(6)+q(7))*sin(q(4)-(q(2)+q(3)));
c44=0;

```

%% indicate value of K matrix;

```

k11= lambda*kc+kr+kt*(q(3)^2);
k12=0;
k13=0;
k14=0;
k21= lambda*Ft;
k22=ka;
k23=0;
k24=-1*ka;
k31= lambda*Ft;
k32=0;
k33=kt*(q(1)^2);
k34=0;
k41=0;
k42=-1*ka;
k43=0;
k44=ka;

```

%% for {f} vector

```

f11= -1*kr*thou0- lambda*kc*(delta);
f21=0;

```

f31=0;

f41=0.5\* lambda\*Ft\*d; %0.5d=R

%% fill in [M] [C] [G] [F] matrix

M=[m11 m12 m13 m14; m21 m22 m23 m24; m31 m32 m33 m34; m41 m42 m43 m44];

C=[c11 c12 c13 c14; c21 c22 c23 c24; c31 c32 c33 c34; c41 c42 c43 c44];

K=[k11 k12 k13 k14; k21 k22 k23 k24; k31 k32 k33 k34; k41 k42 k43 k44];

f=[f11 f21 f31 f41]';

F=[0 0 0 tao]';

%% State Space

A = [zeros(size(M)) eye(size(M))

    -MK    -MC];

B = [zeros(size(F)); MF];

D = [zeros(size(f)); -Mf];

dqdt=A\*q+B+D;

## **Bibliography**

Aarrestad, T. V., Tonnesen, H. A. and Kyllingstad, A., 1986, "Drillstring Vibrations: Comparison Between Theory and Experiments on a Full-Scale Research Drilling Rig," *Proceedings of SPE/ADC 14760 Drilling Conference*, Dallas, TX.

Antoulas, A. C., Sorensen, D. C. and Gugercin, S., 2001, "A survey of model reduction methods for large-scale systems," *Contemp. Math.*, **280**, pp. 193-219.

Awrejcewicz, J. and Olejnik, P., 2005, "Friction Pair Modeling by a 2-DOF System: Numerical and Experimental Investigations," *International Journal of Bifurcation and Chaos in Applied sciences and Engineering*, **15**(6), pp. 1931-1944.

Batako, A. D. L. and Piiroinen, P. T., 2008, "Friction-driven vibro-impact system for percussive-rotary drilling: a numerical study of the system dynamics," *Proceedings of the Institution of Mechanical Engineers, Part C: Journal of Mechanical Engineering Science*, **222**(10), pp. 1925-1934.

Baz, A. and Poh, S., 1988, "Performance of an Active Control System with Piezoelectric Actuators," *Journal of Sound and Vibration*, **126**, pp. 327-343.

Bergmann, M., Cordier, L. and Brancher, J. P., 2005, "Optimal rotary control of the cylinder wake using proper orthogonal decomposition reduced-order model," *Physics of Fluid*, **17**, pp. 097101-1– 097101-21

Berlioz, A., der Hagopian, J., Dufour, R. and Draoui, E., 1996, "Dynamic Behaviour of a Drill-string: Experimental Investigation of Lateral Instabilities," *ASME Journal of Vibration and Acoustics*, **118**, pp. 292–298.

Bockelmann, U., Essevaz-Roulet, B. and Heslot, F., 1997, "Molecular Stick-Slip Motion Revealed by Opening DNA with Piconewton Forces," *Physical Review Letters*, **79**(22), pp.4489-4492.

Canudas-de-Wit, C., Corchero, M.A., Rubio, F.R. and Navarro-Lopez, E., 2005, "D-OSKIL: a New Mechanism for Suppressing Stick-Slip in Oil Well Drillstrings," *Proceedings of the 44th IEEE Conference on Decision and Control, and the European*

*Control Conference 2005*, Seville, Spain.

Christoforou, A. P. and Yigit, S. A., 1997, "Dynamic Modelling of Rotating Drill-strings with Borehole Interactions," *Journal of Sound and Vibration*, **206**, pp. 243–260.

Christoforou, A.P. and Yigit, A.S., 2003, "Fully Coupled Vibrations of Actively Controlled Drillstrings," *Journal of Sound and Vibration*, **267**, pp. 1029-1045.

Cook, R. I., Nicholson, J. W., Sheppard, M. C. and Westlake, W., 1989, "First Real Time Measurements of Downhole Vibrations, Forces and Pressures Used to Monitor Directional Drilling Operations," *Proceedings of the SPE/ADC 18651 Drilling Conference*, New Orleans, LA.

Corchero, M.A., Canudas-de-Wit, C. and Rubio, F.R., 2006, "Stability of the D-OSKIL Oscillation Suppression Mechanism for Oil Well Drillstrings," in *Proceedings of the 45th IEEE Conference on Decision & Control*, San Diego, CA.

Crowther, A. R. and Zhang, N., 2005, "Torsional Finite Elements and Nonlinear Numerical Modelling in Vehicle Powertrain Dynamics," *Journal of Sound and Vibration*, **284**, pp. 825-849.

Duan, C. and Singh, R., 2006, "Dynamics of a 3DOF Torsional System with a Dry Friction Controlled Path," *Journal of Sound and Vibration*, **289**, pp. 657-688.

Hsu, C.S., 1980, "A Theory of Cell-to-Cell Mapping Dynamical Systems," *ASME Journal of Applied Mechanics*, **47**, pp. 931-939.

Jansen, J. D., 1991, "Non-linear Rotor Dynamics as Applied to Oilwell Drillstring Vibrations," *Journal of sound and Vibration*, **147**(1), pp.115-135.

Karnopp, D., 1985, "Computer Simulation of Stick–slip Friction in Mechanical Dynamic Systems," *ASME Journal of Dynamic Systems, Measurement, and Control*, **107**, pp. 100–103.

Khulief, Y.A. and Al-Naser, H., 2005, "Finite element dynamic analysis of drillstrings," *Finite Elements in Analysis and Design*, **41**(13), pp. 1270–1288.

Khulief, Y.A. and Al-Sulaiman, F.A., 2009, "Laboratory investigation of drillstring vibrations," *Proceedings of the Institution of Mechanical Engineers, Part C: Journal of Mechanical Engineering Science*, 223, pp. 2249–2262.

Leine R. I. and Nijmeijer, H., 2004, *Dynamics and Bifurcations of Non-Smooth Mechanical Systems*, Springer, New York.

Leine, R.I., van Campen, D.H., de Kraker, A. and Van den Steen, L., 1998, "Stick-slip Vibrations Induced by Alternate Friction Models," *Nonlinear Dynamics*, **16**, pp. 41-54.

Leine, R. I., van Campen, D. H. and Keultjes, W. J. G., 2002, "Stick-Slip Whirl Interaction in Drill String Dynamics," *ASME Journal of Vibration and Acoustics*, **124**(2), pp. 209-220.

Leine, R. I. and van Campen, D. H., 2002, "Discontinuous Bifurcations of Periodic Solutions," *Mathematical and Computer Modelling*, **36**(3), pp. 259-273.

Liao, C.-M., Balachandran, B. and Karkoub, M., 2009, "Drill String Dynamics: Reduced-Order Models," *ASME Conf. Proc. 2009*, Paper No. IMECE2009-10339, pp. 451-460.

Liao, C.-M., Balachandran, B., Karkoub, M. and Abdel-Magid, Y. L., 2011, "Drill-String Dynamics: Reduced-Order Models and Experimental Studies," *ASME Journal of Vibration and Acoustics*, **133**(4), pp. 041008-1–041008-8.

Liao, C.-M., Vljajic, N., Karki, H. and Balachandran, B., 2011, "Parametric Studies on Drill-String Motions", *International Journal of Mechanical Sciences*, Accepted

Long, X.-H., 2006, "*Loss of Contact and Time Delay Dynamics of Milling Process*," Ph. D. Dissertation, University of Maryland, College Park, MD.

Long, X.-H. and Balachandran, B., 2007, "Stability Analysis for Milling Process," *Nonlinear Dynamics*, **49**(3), pp. 349-359.

Long, X.-H., Lin, G. and Balachandran, B., 2007, "Grazing Bifurcations in Elastic Structure Excited by Harmonic Impactor Motions," *Physica D: Nonlinear Phenomena*, **237**(8), pp. 1129-1138.

Macdonald, K. A. and BJune, J. V., 2007, "Failure Analysis of Drillstrings," *Engineering Failure Analysis*, **14**(8), pp. 1641-1666.

Meirovitch, L., 2001, *Fundamentals of Vibrations*, McGraw Hill, New York.

Melakhessou, H., Berlioz, A. and Ferraris, G., 2003, "A Nonlinear Well-Drillstring Interaction Model," *ASME Journal of Vibration and Acoustics*, **125**, pp. 46-52.

Mihajlović, N., van Veggel, A. A., van de Wouw, N. and Nijmeijer, H., 2004, "Analysis of Friction-Induced Limit Cycling in an Experimental Drill-String System," *ASME Journal of Dynamic Systems, Measurement, and Control*, **126**(4), pp. 709-720.

Mihajlović, N., van de Wouw, N., Hendriks, M. P. M. and Nijmeijer, H., 2006, "Friction-induced limit cycling in flexible rotor systems: An experimental drill-string set-up," *Nonlinear Dynamics*, **46**, pp. 273-291.

Mihajlović, N., van de Wouw, N., Rosielle, P. C. J. N. and Nijmeijer, H., 2007, "Interaction between Torsional and Lateral Vibrations in Flexible Rotor systems with Discontinuous Friction," *Nonlinear Dynamics*, **50**, pp. 679-699.

Mottershead, J.E., 1998, "Vibration and Friction- Induced Instability in Disks," *Shock and Vibration Digest*, **30**(1), pp. 14-31.

Naguleswaran, S., 2003, "Transverse Vibration and Stability of an Euler–Bernoulli Beam with Step Change in Cross-section and in Axial Force," *Journal of sound and Vibration*, **270**, pp. 1045-1055.

Navarro-Lopez, E.M. and Cortes, D., 2007, "Avoiding Harmful Oscillations in a Drillstring through Dynamical Analysis," *Journal of Sound and Vibration*, **307**, pp.152-171.

Navarro-Lopez, E.M. and Cortes, D., 2007, "Controller Parameters Selection Though

Bifurcation Analysis in a Piecewise-Smooth System,” *Proc. HSCC, 2007*, pp. 736-740.

Nayfeh, A. H. and Balachandran, B., 1995, 2006, *Applied Nonlinear Dynamics: Analytical, Computational, and Experimental Methods*, Wiley, New York.

Nayfeh, A. H. and Balachandran, B., 1989, “Modal Interactions in Dynamical and Structural Systems,” *Applied Mechanics Reviews*, **42**(11-2), pp. 175-202.

Nguyen, V., Schultz, G., and Balachandran, B., 2009, "Lateral Load Transfer Effects on Bifurcation Behavior of Four-Wheel Vehicle System," *ASME Journal of Computational and Nonlinear Dynamics*, **4**, pp. 041007-1-041007-12.

Pelinescu, I., 2002, “*Active Control of Wave Transmission Through Cylindrical Struts*,” Ph. D. dissertation, University of Maryland, College Park, USA.

Pfeiffer, F. and Glocker, C., 1996, *Multibody Dynamics with Unilateral Contacts*, Wiley-Interscience, New York.

Popp, K. and Stelzer, P., 1990, “Stick-slip Vibration and Chaos”, *Philosophical Transactions: Physical Sciences and Engineering*, **332**(1624). pp. 89-105.

Popprath, S. and Ecker, H., 2007, “Nonlinear Dynamics of a Rotor Contacting an Elastically Suspended Stator,” *Journal of Sound and Vibration*, **308**(3-5), pp. 767 -784.

Richard, T., Germy, C. and Detournay, E., 2004, “Self-excited Stick-slip Oscillation of Drill Bits,” *C.R. Mecanique*, **332**, pp. 619-626.

Ritto, T. G., Soize, C. and Sampaio, R., 2009, “Non-linear dynamics of a drill-string with uncertain model of the bit-rock interaction” *International Journal of Non-Linear Mechanics*, **44**, pp. 865-876.

Russ, J. C., 2006, *Image Processing Handbook*, 5<sup>th</sup> edition, CRC Press.

Tucker, R. W. and Wang, C., 1999, “An Integrated Model for Drill-String Dynamics,” *Journal of Sound and Vibration*, **224**, pp. 123-165.

Spanos, P. D., Chevallier, A. M., Politis, N. P. and Payne, M. L., 2003, "Oil and Gas Well Drilling: A Vibrations Perspective," *Shock and Vibration Digest*, **35**(2), pp. 85-103.

Staal, J., Abramoff, M.D., Niemeijer, M., Viergever, M.A. and van Ginneken, B., 2004, "Ridge-based vessel segmentation in color images of the retina," *IEEE Transaction on Medical Imaging*, **25**(4), pp.501-509.

Swanson, E., Powell, C.D. and Weissman, S., 2005, "A Practical Review of Rotating Machinery Critical Speeds and Modes," *Sound and Vibration*, **39**(5), pp.10-17.

Vlajic, N., Liao, C.-M., Karki, H. and Balachandran, B., 2011, "Stick Slip and Whirl of Drill Strings: Numerical and Experimental Studies", *ASME Conf. Proc. 2011*, Paper No. DETC2011-47949.

Wang, L., Tan, T. Ning, H. and Hu, W., 2003, "Silhouette Analysis-Based Gait Recognition for Human Identification," *IEEE Transaction on Pattern Analysis and Machine Intelligence*, **25**(12), PP. 1505-1518.

Yigit, S. A. and Christoforou, A. P., 1996, "Coupled Axial and Transverse Vibrations of Oilwell Drillstrings," *Journal of Sound and Vibration*, **195**(4), pp. 617-627.

Yigit, S. A. and Christoforou, P. A., 1998, "Coupled Torsional and Bending Vibrations of Drill-strings Subject to Impacts with Friction," *Journal of Sound and Vibration*, **215**, pp. 167-181.